Role of interlayer couplings in bilayer superconductors: A variational Monte Carlo study

Amal Medhi

A thesis
submitted for the degree of
Doctor of Philosophy

Department of Physics
Indian Institute of Technology Guwahati
Guwahati 781039, India

October 2008

Role of interlayer couplings in bilayer superconductors: A variational Monte Carlo study

Amal Medhi

A thesis
submitted for the degree of
Doctor of Philosophy

Supervisors:
Charudatt Kadolkar and Saurabh Basu

Department of Physics
Indian Institute of Technology Guwahati
Guwahati 781039, India

October 2008

Certificate

It is certified that the work contained in the thesis entitled "*Role of interlayer couplings in bilayer superconductors: A variational Monte Carlo study*" by Mr. Amal Medhi, a student of the Department of Physics, IIT Guwahati was carried out under our supervision and has not been submitted elsewhere for award of any degree.

Charudatt Kadolkar

Saurabh Basu

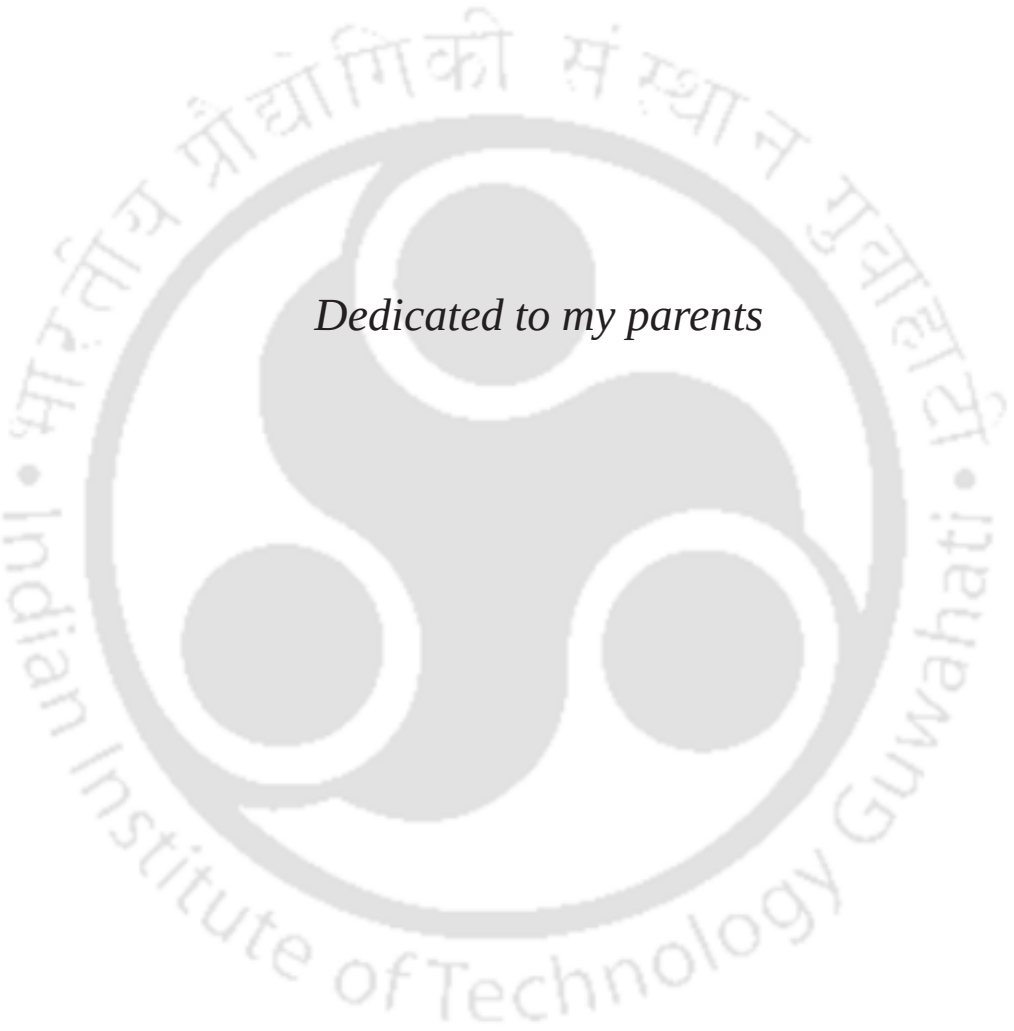

Dedicated to my parents

Acknowledgements

It has been a great pleasure and tremendous learning experience for me to work under the supervision of Dr. Charudatt Kadolkar and Dr. Saurabh Basu. Starting from ground zero, I gained immensely from the vast knowledge and versatile ability of Dr. Kadolkar, wide expertise of Dr. Basu, who with their generous helps enabled me to attain a foothold in this difficult and fascinating field of research in high-T_c superconductivity. I express my deep gratitude and heartiest thanks to them for all the supports, all the freedom that they gave me to learn and the constant encouragement throughout the course of my research. Above all, they have been my great friends with whom I could share my thoughts freely. Their witty comments on various matters have been unforgettable. I thoroughly enjoyed their companionship and felt very fortunate to have them as my guide.

I thank Prof. A. Srinivasan for his constant encouragement and valuable suggestions and Dr. S. B. Santra and Prof. R. Alam for their useful comments on my work. I would like to thank Prof. A. Khare who has been very cordial and always helpful. I extend my thanks to all other faculty members of this institute who helped me in various ways during this period. I specially thank Prof. M. K. Chaudhuri for his kindness and great helps to me in a few crucial situations. I remain grateful to the Department of Physics, IIT Guwahati for all the supports and the work environment it gave which was very comfortable. The facilities in IIT Guwahati have been wonderful. Particularly its computational facilities were instrumental in making this work possible. I enjoyed the beautiful atmosphere in the campus and feel to have spent the best years of my life here. I gratefully acknowledge the Council of Scientific and Industrial Research (CSIR), India for the financial support to me during the major part of this work. I also received a financial assistance jointly from the Department of Physics, IIT Guwahati, Department of Science and Technology (DST), India and CSIR, India to attend an international conference abroad. I remain thankful to all of them.

The last one and half years of the work were done while I was working as a Lecturer at the Department of Basic Sciences and Social Sciences, School of Technology, North-Eastern Hill University, Shillong. I thank all my colleagues there for their kind cooperation on various matters. I specially mention Mr. Regenel Kharwanlang who voluntarily took many of my duties to make me free for the work. I am indebted to Dr. A. K. Das, who extended all possible helps to me as the Head of the Department so that I could devote adequate time in my research. His constant encouragement, support, and kindness will be fondly remembered.

I have had a very pleasant times with my friends in IIT Guwahati. I specially thank Munima for her company and constant advices. She had to bear my stories and emotions all the time and had been admirably patient with that. I will remember Sidananda Sarma for his brotherly supports, guidance and his instant readiness to help me at any moment. I enjoyed the company of Poulumi, Biswanath, Manos and many other friends. Thanks to all of them.

My family members, parents, brothers, sisters and cousins have always been supporting to me. Their loves, ardent hopes on me kept me motivated all the time. I thank Chandan Patowary and Jayanta Sarmah for their helps and guidance in the days before my joining here.

Finally, my special thanks are due to Mitali for her hearty supports and undying loves which acted as a source of great inspiration to me.

Abstract

The ground state superconducting and magnetic properties of bilayer cuprate superconductors are studied using a *t*-*J* model with interlayer couplings using the variational Monte Carlo (VMC) method. As a separate exercise, but relevant to the single layers and ladder compounds, a brief study of an impurity doped Hubbard model via the quantum Monte Carlo method is reported. To settle a crucial question regarding the symmetry of the superconducting order parameter, we investigated the stability of a number of different pairing symmetries for a *t*-*J* bilayer. For model parameter values that are suggested by experimental studies on bilayer superconductors, the favourable pairing symmetry of the superconducting state is found to be *d*-wave. Superconductivity coexists with antiferromagnetic long range order in the underdoped region. Superconducting and magnetic properties in the pure superconducting and the coexisting state are examined and it is convincingly shown that in the coexisting phase, both the antiferromagnetic and superconducting correlations are enhanced. Further, to compliment the phase diagrams of planar systems available in literature, we obtained a ground state phase diagram for a *t*-*J* bilayer as a function of interlayer couplings. The phase diagram shows rich features, such as, a crossover of superconducting correlations from being predominantly planar to strongly interplanar as interlayer exchange coupling is increased, a non-monotonic variation of the critical hole concentraion, upto which the *d*-wave superconducting phase remains stable, as a function of interplanar hopping parameter etc. In addition, there is a lowering of superconducting correlations as a function of interlayer hopping in the under and optimally doped phases, while these are enhanced in the overdoped region for moderate values of the coupling parameter. However the effect of interlayer coupling parameters on magnetic correlations are much less pronounced. Finally, to complete our discussion on bilayered superconductors, we studied the consequence of interlayer pair tunneling using a grand canonical VMC method, where the superconducting state of a bilayer is described by a variational wavefunction that is a product of two Gutzwiller projected *d*-wave BCS wavefunctions, one for each layer, with variable particle number. Our calculations show that the energy due to the tunneling of Cooper pairs across the layers has interesting bahaviour. However, the magnitude of energy is found to be too small to have any significant effect on the physical properties at least for realistic values of the tunneling parameter.

Contents

List of Figures

Chapter 1

Introduction

High temperature superconductivity in cuprates continues to be an intense research topic in condensed matter physics due to the highly unusual features and its immense potential in technological applications. The cuprate superconductors are characterized by the presence of one or more copper oxide (CuO_2) layers per unit cell in the crystal structure. The key physics of the high temperature superconductors (HTSC) lies in these copper oxide layers where electronic correlations are very strong. The low energy electronic excitations in a single copper oxide layer is well represented by a two dimensional Hubbard model and its strong coupling variant, the t-J model. Theoretical studies on these two models have concentrated primarily on a single layer and have been quite successful in reproducing the main features of the phase diagram of high-T_c superconductors. However presence of more than one copper oxide layers per unit cell in the crystal structure leads to some important consequences to the physical properties of the cuprates. In this work we shall study the ground state superconducting and magnetic properties of bilayer superconductors and the role of interlayer couplings in the framework of the t-J model using variational Monte Carlo (VMC) method.

In chapter 2, we introduce the model Hamiltonian, i.e. a t-J model containing planar and interplanar couplings, that we consider for describing bilayer superconductors. The numerical code for the variational Monte Carlo method used to study the model is developed and tested. The method is described in details. This chapter also contains a report on a Quantum Monte Carlo (QMC) study of the Hubbard model doped with nonmagnetic impurities. We took this brief detour to understand the interesting effects of nonmagnetic impurity doping in

cuprate compounds observed experimentally. Chapter 3 contains a study of the superconducting pairing symmetry in a t-J bilayer for parameter values relevant to the bilayer cuprates. The magnetic and superconducting properties of the $d_{x^2-y^2}$ wave superconducting state which turns out to be a favourable state in bilayers are examined in details. Next the interplay of antiferromagnetism and superconductivity is examined using a variational wavefunction which describes both these orders simultaneously. Superconductivity coexists with antiferromagnetism in the underdoped phase as in planar systems. The properties of the coexisting state are compared with those of the pure superconducting state and the coexisting phase is found to have enhanced superconducting and magnetic correlations. In chapter 4, we obtain a ground state phase diagram of the bilayer t-J model as a function of interlayer coupling parameters and hole concentration. Effects of interlayer couplings on various physical properties are examined and discussed in details. In chapter 5, we study the consequence of interlayer pair tunneling in the superconducting state of a bilayer using a grand canonical VMC method based on a new Monte Carlo algorithm. The summary of all the results of the study alongwith its possible extensions are discussed in chapter 6.

In the remaining part of this introductory chapter we shall briefly review the basic experimental facts and a few current topics in theoretical studies of high-T_c superconductors. Details of the phenomenon in various respects have been discussed extensively in the past in literature. Here we only attempt to highlight some of its most interesting features and then bring out the underlying motivation for our present work.

1.1 A preliminary survey on high-T_c superconductors

1.1.1 A new class of material

A new class of material emerged with the discovery of superconductivity in barium doped La_2CuO_4 by Bednorz and Müller in 1986[1]. Undoped La_2CuO_4 is a ceramic compound which is a very good insulator. When doped with barium, quite remarkably, it became superconducting with a high transition temperature, T_c of around 30°K. This critical temperature was a step above the previously known highest T_c, which for several years remained around 23°K (for Nb_3Ge) in the inter-metallic compounds[2]. Superconductivity in the La-Ba-Cu-O system was immediately confirmed by several groups and the T_c was pushed even

higher[3, 4, 5, 6, 7]. Using strontium as dopant, another compound $La_{2-x}Sr_xCuO_4$ (LSCO) was discovered with a T_c of around 36°K[8, 9]. Soon, Wu *et al*[10] discovered superconductivity in $YBa_2Cu_3O_{6+x}$ (YBCO) with a T_c of about 93°K, a temperature well above the boiling point of liquid nitrogen (77°K). Besides these, a large number of other systems of superconducting materials, e.g. Bi-Sr-Ca-Cu-O[11, 12], Tl-Ba-Ca-Cu-O[13, 14] and Hg-Ba-Ca-Cu-O[15, 16], have been discovered having still higher critical temperatures.

The strikingly common feature in the crystallographic arrangement of all these materials is its layered perovskite-like structures which contain one or more copper oxide (CuO_2) planes per unit cell[17, 18, 19, 20]. The compounds are called cuprates because of the presence of these CuO_2 layers. In LSCO, for example, there is one CuO_2 layer while YBCO have two layers separated by Y atoms in a unit cell (Fig. 1.1). The number of CuO_2 layers per

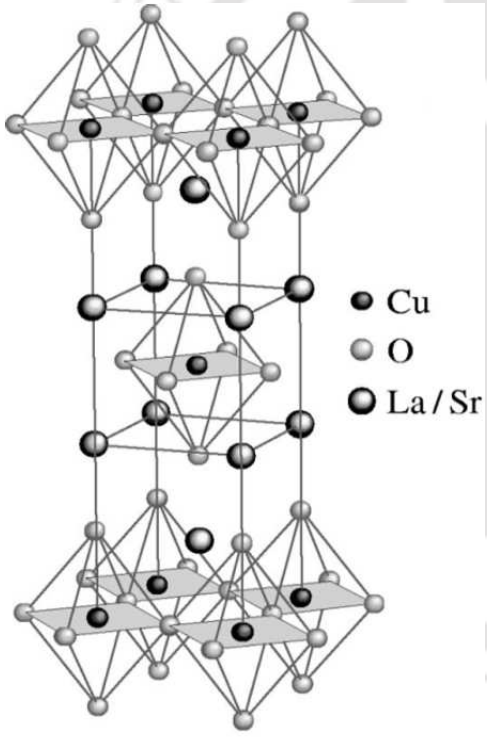

(a) Crystal structure of $La_{2-x}Sr_xCuO_4$ (Soure: Ref. [21]).

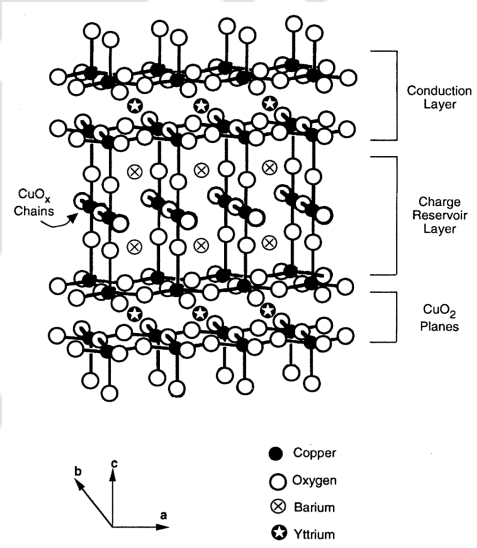

(b) Crystal structure of $YBa_2Cu_3O_{6+x}$ (Source: Ref. [22])

FIGURE 1.1: Crystal structure of two well known high-T_c superconductors.

unit cell in the Bi, Tl, and Hg compounds can vary from one to three or even higher. Charge transport takes place in the CuO_2 planes and hence these are called conduction planes. In one CuO_2 plane, each copper atom is surrounded by four oxygen atoms in a square planar

configuration (*ab* plane). The distance between copper and a neighbouring oxygen atom in a plane is approaximately 1.9 Å, which is rather small and hence there exists strong covalent bonds between copper and oxygen atoms in a CuO_2 plane. The CuO_2 planes are separated by insulating layers of other metal oxides, such as LaO, BaO, BiO etc. The insulating layers provide charge carriers to the CuO_2 planes and hence are called charge reservoirs. The distance (along *c* direction) between two CuO_2 layers in two adjacent unit cells is quite large, approaximately 6.6 Å in $La_{2-x}Sr_xCuO_4$ for instance. The resulting crystal structure is highly anisotropic tetragonal which often makes transition to orthorhombic structure as temperature or pressure is varied. In compounds which have more than one CuO_2 planes per unit cell, the separation between two such planes in a unit cell is small. For example, in bilayered YBCO the distance between two CuO_2 layers in same unit cell is ~ 3.2 Å, whereas the unit cells itself are separated from each other by a distance of ~ 8.2 Å. This makes possible an interlayer coupling between two close CuO_2 layers in a multilayered compound, which is believed to give rise to the higher T_c and other important differences in physical properties of the multilayered cuprates in comparison to its single layered counterparts.

Most of the high-T_c superconductors can be grouped into certain homologous series based on their structural formulae[20, 23]. For example, the Bi, Tl and Hg based compounds can be grouped into families represented by the general formulae, $Bi_2Sr_2Ca_{n-1}Cu_nO_{2n+4+x}$ (Bi-22($n-1$)n, BSCCO), $Tl_mBa_2Ca_{n-1}Cu_nO_{2n+2+m+x}$ (Tl-m2($n-1$)n) and $HgBa_2Ca_{n-1}Cu_nO_{2n+2+x}$ (Hg-12($n-1$)n), respectively. Here m and n denote two integers with n representing the number of CuO_2 layers per unit cell. The superconducting transition temperatures, T_c of the members of a series depend on n. In a homologous series, T_c of an individual member increases with the number n for n equal to one, two or three. For example, Bi2201 ($n = 1$), Bi2212 ($n = 2$) and Bi2223 ($n = 3$) of the BSCCO family of superconductors have T_c equal to 20°K, 85°K and 110°K, respectively (see Ref. [20]). There are also compounds having the value of n greater than three. However, T_c is found to decrease when n increases beyond three. The Hg based compounds are found to have the highest values of T_c amongst the cuprates discovered currently. In the Hg-Ba-Ca-Cu-O family, Hg1201 (n=1), Hg1212 (n=2) are Hg1223 (n=3) have T_c equal to 94°K, 127°K and 133°K, respectively. The critical temperature of $HgBa_2Ca_2Cu_3O_{8+x}$ (Hg1223) has been raised to above 150°K under very high pressure[16], and it is one of the highest observed T_c so far.

1.1.2 Universal phase diagram

The phase diagrams of the high-T_c superconductors are marked by a number of universal features (see Ref. [24, 25, 26, 27] for detailed discussion). The undoped compounds, called parent compounds, of all the high-T_c superconductors are antiferromagnetic insulators. Upon doping with charge carriers, the antiferromagnetic order diminishes and superconductivity appears after a finite carrier concentration at low temperatures. To elaborate on the details, we discuss below the phase diagrams of two well known compounds, $La_{2-x}Sr_xCuO_4$ and $YBa_2Cu_3O_{6+x}$. Fig. 1.2(a) shows the phase diagram of $La_{2-x}Sr_xCuO_4$. Undoped La_2CuO_4 ($x = 0$) is an insulator. The free state electronic configurations of the constituent atoms in

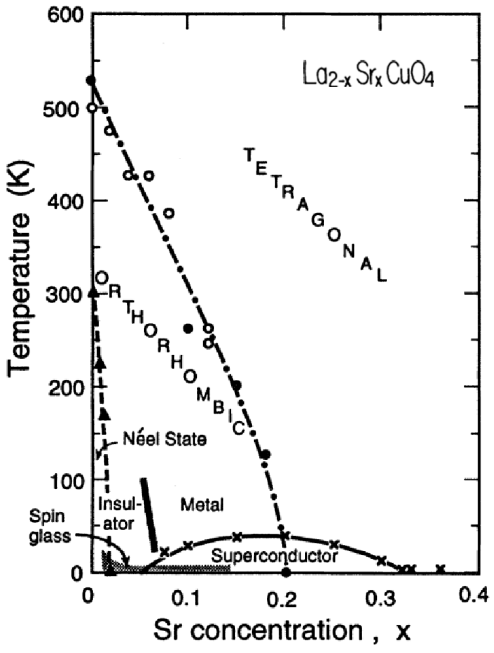

(a) Phase diagram of $La_{2-x}Sr_xCuO_4$ (Source: Ref. [28]).

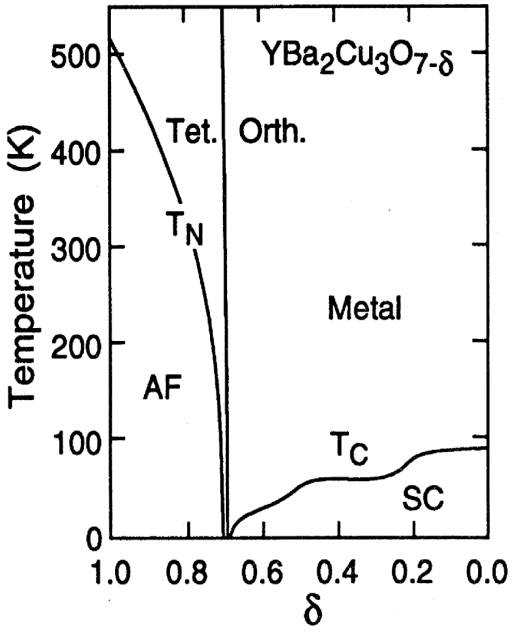

(b) Phase diagram of $YBa_2Cu_3O_{6+x}$, where $x = (1-\delta)$ (Source: Ref. [29]).

FIGURE 1.2: Phase diagrams of two well studied high-T_c superconductors.

this compound are given by, La(57)→[Xe]$(5d)^1(6s)^2$, Cu(29)→[Ar]$(3d)^{10}(4s)^1$ and O(8)→[He]$(2s)^2(2p)^4$. In La_2CuO_4, lanthanum loses three electrons and attains the stable configuration La^{3+}. Oxygen accepts two electrons to complete its valence shell and is in state O^{2-}. To conserve charge neutrality copper must be in state Cu^{2+}, which is achieved by losing one $4s$ and one $3d$ electron. Thus in La_2CuO_4, copper ions are in an incomplete valence shell configuration $3d^9$. With one hole per copper atom (in the $3d_{x^2-y^2}$ orbital), the valence band is

half-filled and according to the band theory the compound should have been a metal. However it is an antiferromagnetic insulator, a fact which underlines the dramatic consequences of strong electronic correlation[30]. Charge fluctuations are prevented in La_2CuO_4, because it costs a large amount of energy for two holes or electrons to occupy a single copper $3d_{x^2-y^2}$ orbital due to strong repulsive interaction between them[30, 31]. Such an insulator where charge carriers are localized due to strong electronic correlations is called a Mott insulator as opposed to a band insulator. Indeed, the charge excitation gap in La_2CuO_4 is of the order of 2 eV as observed in various optical measurements[32, 33, 34]. The magnetic ordering in $La_{2-x}Sr_xCuO_4$ has been extensively studied by neutron scattering experiments (see Ref. [25, 35] for review). Because of the partially filled $3d^9$ configuration, each Cu^{2+} ion in La_2CuO_4 carry a magnetic moment which was found to be of magnitude $\sim 0.5\mu_B$ and lying almost parallel to a CuO_2 plane[36]. At half-filling ($x = 0$), the magnetic moments are ordered antiferromagnetically with a Néel temperature, T_N of 325°K[37]. The magnetic correlations are two dimensional in nature with strong exchange coupling between the spins in a CuO_2 plane and weak coupling between spins in different layers. The nearest neighbour antiferromagnetic exchange coupling energy in a CuO_2 plane is found to be ~ 0.13 eV[38, 39] which is one of the largest value of exchange energy observed. When La_2CuO_4 is doped with Sr atoms, La^{3+} ions are replaced by Sr^{2+} and consequently holes (charge carriers) are introduced into the CuO_2 planes. Several phase transitions occur in the material with introduction of holes. T_N decreases dramatically as seen in Fig. 1.2(a) with the AF long range order (AFLRO) vanishing completely at hole doping, $x \sim 0.02$. However 2D short range AF correlations survive and extends upto the superconducting state which appears at $x \sim 0.05$. With further increase in Sr concentration, the superconducting transition temperature, T_c rises gradually till it becomes maximum at $x \sim 0.15$. Beyond this doping level, T_c starts decreasing slowly and eventually superconductivity vanishes at $x \sim 0.30$. The doping range (around $x \sim 0.15$) at which T_c is maximum is called optimally doped region, while the region to the left of the peak ($x < 0.15$) in the phase diagram is called underdoped region. The higher hole doping range ($x > 0.15$) is called overdoped region. In the underdoped region above about 2% doping, the material behaves as a 2D disordered metal at higher temperature and makes gradual crossover to an insulating spin glass phase at low temperature. A structural phase transition also occurs in the compound as shown in the phase diagram. The tetragonal phase at high temperature makes a phonon driven transition into orthorhombic phase at lower temperatures[40, 41].

The phase diagram for $YBa_2Cu_3O_{6+x}$, a bilayered compound, is shown in Fig. 1.2(b). In

this compound Cu atoms exist both in the CuO_2 conduction planes and in the charge reservoir between the conduction planes. In the charge reservoir, Cu atoms form the linear Cu-O chains which have varying oxygen content. By changing x (or δ in the notation of Fig. 1.2(b)), oxygen is added to or removed from the Cu-O chains. The Cu-O chains provide and control charge carriers for electrical conduction in the CuO_2 planes[29]. For $x \lesssim 0.3$, the crystal structure is tetragonal and the material is insulating. The Cu^{2+} spins in the copper oxide planes are ordered antiferromagnetically with the Néel temperature, T_N being about 410°K near half-filling ($x = 0.0$) [42, 43] which is considerably higher than that in single layered LSCO. The three dimensional (3D) AF long range order diminishes with increasing x and vanishes completely at $x \sim 0.3$. Adding further oxygen to the Cu-O chains provides holes into the CuO_2 planes and consequently superconductivity starts developing with the crystal structure making transition to an orthorhombic phase. The transition temperature, T_c rises with increasing oxygen content but not monotonically. There is a plateau region between $x \sim 0.5$ and 0.7 where T_c remains fixed at about 60°K. The T_c becomes maximum ($\sim$ 93°K) for fully oxygenated compound $YBa_2Cu_3O_7$ ($x = 1.0$). It may be mentioned that there are electron doped compounds, such as $Nd_{2-x}Ce_xCuO_{4-y}$, whose phase diagrams show similar evolution with carrier (electron) concentration as the hole doped compounds[24].

In general, the under- and optimally doped regions of the phase diagrams of all high-T_c superconductors have been intriguing. In this region of hole doping, the physical properties show a host of anomalous features which do not follow the Landau Fermi liquid (FL) theory (to be discussed in §1.1.3). The normal state above T_c in the optimally doped region show a strange 2D metallic behaviour in which electrical transport is strictly confined to the copper oxide planes. Some of the non-Fermi liquid (NFL) behaviours in this metallic state are - linear dependence of resistivity on temperature, temperature dependence of Hall coefficient, unusual optical conductivity etc. Also the underdoped phase shows the phenomenon of pseudogap, where below a characteristic temperature T^* ($\gg T_c$), an energy gap exists without any phase coherence. On the other hand, normal 3D metallic behaviour is recovered gradually in the overdoped region with the restoration of Fermi liquid like features. These universal features of high-T_c superconductors are schematically depicted in the generic phase diagram shown in Fig. 1.3.

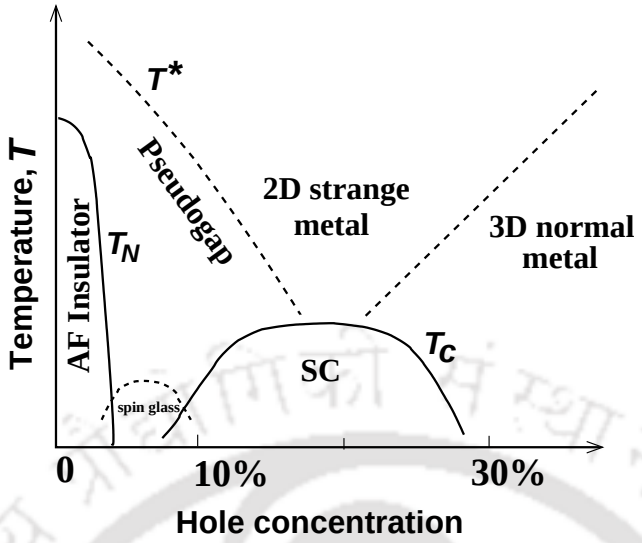

FIGURE 1.3: A schematic phase diagram of hole doped high-T_c superconductors.

1.1.3 Anomalous behaviour

High-T_c superconductors have been under intense investigation because of its puzzling features which challenge existing condensed matter theories. Apart from the highly unconventional superconductivity, the normal metallic state in these materials itself is unusual in many respects and is believed to hold the key to understanding high-T_c superconductivity. Here we state some of the important properties of the high-T_c superconductors which are strikingly different from those of conventional superconductors. For detailed description, see Ref. [25, 26, 44, 45, 46, 47, 48].

We first focus on the normal state properties. Electrical transport properties in the cuprates have been studied quite extensively and experimental data on many different compounds show a strikingly unusual behaviour. The resistivity, ρ_{ab} of these compounds parallel to the CuO_2 planes is almost linear in temperature, T over a wide range of temperature. This is illustrated in Fig. 1.4(a) which shows the experimental results for resistivity in $La_{2-x}Sr_xCuO_4$ in the optimal and underdoped region[49]. However it is only a representative figure and similar behaviour is observed in other compounds[51, 52, 53]. It is to be noted that the exact nature of ρ_{ab} dependence on T changes with hole concentration. In the optimally doped region (around $x = 0.15$), ρ_{ab} is linear in T upto a very high temperature ($\sim 1000^\circ K$) and it is given by $\rho_{ab} \sim A + BT$ with the residual resistivity, A being very nearly zero. The value of B scaled by number of CuO_2 layers, remarkably remains constant ($\sim 1.5\ \mu\Omega$cm/°K)[54]

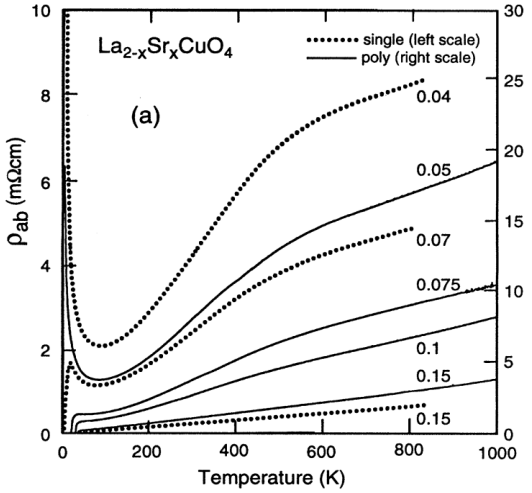

(a) Temperature dependence of in-plane resistivity, ρ_{ab} for optimal and underdoped $La_{2-x}Sr_xCuO_4$ (Source: Ref. [49]).

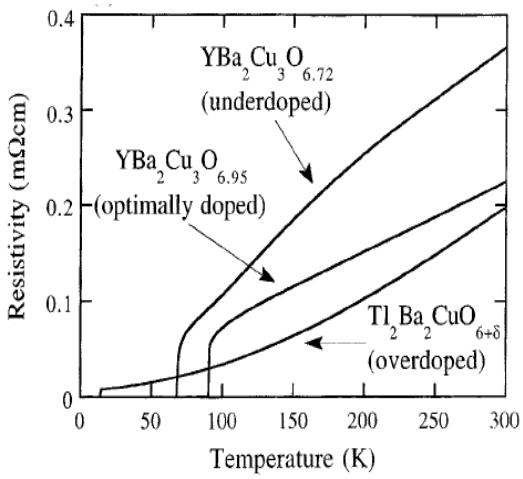

(b) Evolution of $\rho_{ab}(T)$ with doping (Source: Ref. [50]).

FIGURE 1.4: In-plane resistivity, $\rho_{ab}(T)$ in high-T_c superconductors.

for different materials. In contrast, resistivity of a conventional Fermi liquid varies as $\rho \sim T^2$, arising from electron-phonon scattering. In the underdoped region, dependence of ρ_{ab} on temperature is slightly deviated from linearity at low T and it has a different power-law behaviour. In the overdoped regime, it is found that the FL behavior is gradually restored with ρ_{ab} starting to show a T^2 variation. The evolution of in-plane resistivity, $\rho_{ab}(T)$ with doping is nicely demonstrated in Fig. 1.4(b) which shows the representative plots for $\rho_{ab}(T)$ in the three different regimes of hole doping. Apart from the T-linear resistivity, another striking feature in the transport properties of high-T_c superconductors is the huge anisotropy between in-plane and out-of-plane resistivities. In the normal state of all cuprates, c-axis resistivity, ρ_c is very high as compared to ρ_{ab}. In the optimally doped compounds, ρ_c can be larger than ρ_{ab} by a factor of the order $\sim 10^2$ to 10^6. This is anomalous because the factor ρ_c/ρ_{ab} is much greater than what the electronic band structure calculations would suggest and it strongly vary with T[55]. The anisotropy between ρ_c and ρ_{ab} in $YBa_2Cu_3O_{7-x}$ is shown in Fig. 1.5(a)[56]. Moreover, the temperature dependence of ρ_c itself is unusual. For underdoped cuprates, ρ_c can be expressed as $\rho_c \sim A/T + BT$[26]. In this regime, ρ_c is non-metallic and increases with decreasing temperature in sharp contrast to the metallic behaviour of ρ_{ab}. The evolution of $\rho_c(T)$ with doping level for $La_{2-x}Sr_xCuO_4$ is shown in Fig. 1.5(b)[57]. In the heavily overdoped regime, ρ_c/ρ_{ab} becomes temperature independent signaling formation of a coherent c-axis charge motion and development of a 3D electronic ground state[54]. Another puzzling experimental fact about high-T_c superconductors is the temperature dependence of

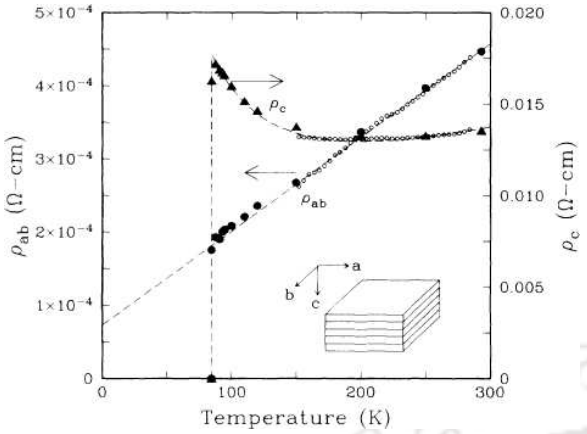

(a) Anisotropy between c-axis and in-plane resistivities, ρ_c and ρ_{ab}, in $YBa_2Cu_3O_{7-x}$ (Source: Ref. [56]).

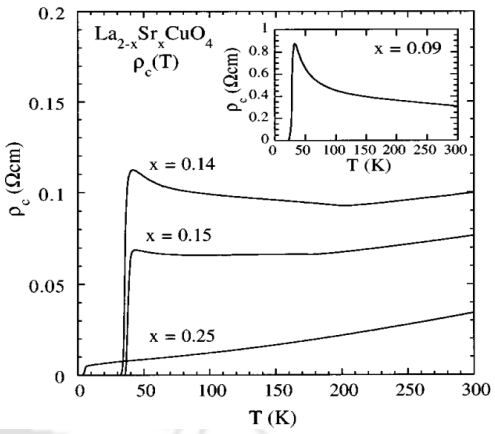

(b) Temperature dependence of ρ_c for $La_{2-x}Sr_xCuO_4$ at various doping levels (Source: Ref. [57]).

FIGURE 1.5: Out-of-plane resistivity, $\rho_c(T)$ in high-T_c superconductors.

Hall coefficient, R_H. While according to the FL theory, R_H should be temperature independent, experimental results for the cuprates show R_H to be strongly T dependent. As an example, Hall coefficient for YBCO measured as a function of T is shown in Fig. 1.6[58]. It is clear

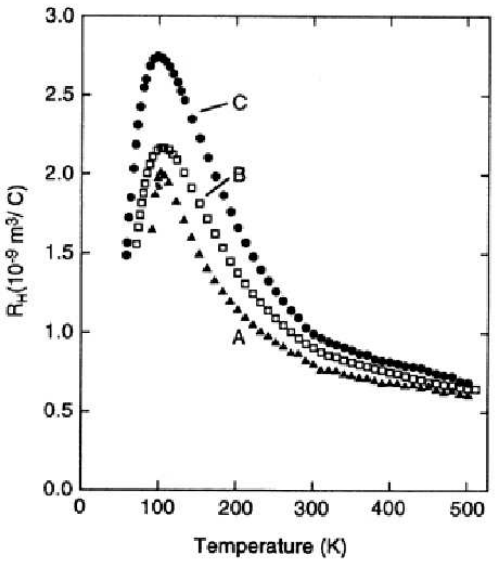

FIGURE 1.6: Hall coefficient, R_H as a function of T for YBCO. Samples A, B and C have T_c values 91°K, 74°K and 60°K, respectively (Source: Ref. [58]).

that R_H have a strong T dependence, in fact it goes as $1/T$ at higher temperatures. Anomalous behaviour of charge transport in high-T_c cuprates is further exemplified by the experimental data on optical conductivity, $\sigma(\omega)$. Both ab-plane and c-axis conductivities, $\sigma_{ab}(\omega)$ and $\sigma_c(\omega)$

have features beyond the Drude like behaviour for ordinary metals (see Ref. [26, 59] and references therein).

Another non-Fermi liquid nature of the normal state of high-T_c superconductors is the phenomenon of pseudogap observed in the underdoped phase of the cuprates (see Ref. [60, 61] for a review). In this phase, low-energy electronic density of states get highly suppressed instead of getting totally eliminated. Existence of the pseudogap and its nature is confirmed by a variety of experiments. In NMR and neutron scattering studies[62, 63], Knight shift and spin susceptibility of underdoped cuprates show a fall below the corresponding values for a Heisenberg antiferromagnet at low temperatures. The coefficient of the temperature dependent term in the expression for electronic specific heat drops rapidly with decreasing T implying the loss of spin entropy at low temperature[64]. These facts are indication of onset of spin singlet pairing leading to the formation of the pseudogap in underdoped cuprates. Angle-resolved photoemmission spectroscopy (ARPES) probes the variation of the energy gap in $\mathbf{k}$-space and its evolution with temperature[65, 66, 67]. The $\mathbf{k}$-dependence of the pseudogap resembles that of the superconducting gap. As temperature is decreased below a certain value T^* ($\gg T_c$) in underdoped cuprates, an energy pseudogap opens up at the Fermi line, first near $(0, \pi)$ direction. The gap has a maximum magnitude here and it gradually extends with decreasing magnitude towards the $k_x = k_y$ line as temperature is further lowered. Eventually at $T = T_c$, the whole Fermi line becomes gaped except at $k_x = k_y$, giving rise to the superconducting energy gap. Thus in other words, as one goes above T_c from lower temperatures, a considerable portion of the Fermi line still remain gaped upto a much higher temperature T^* in the underdoped region, whereas in the overdoped region the superconducting gap closes everywhere at T_c. Indeed, T^* is maximum in heavily underdoped region and decreases with increasing hole doping eventually merging with T_c at optimal doping (Fig. 1.3). The origin of the pseudogap and its connection with superconductivity have been under intense theoretical investigation.

The superconducting (SC) phase of the high-T_c superconductors has always been fascinating due its striking differences with conventional low-T_c superconductors which are well explained by the BCS theory. Apart from the unusually high value of T_c, it exhibits a number of other features that are fundamentally different from those of BCS superconductors. First and foremost is the pairing mechanism. Direct evidence of existence of Cooper pairs in high-T_c superconductors was provided by SQUID measurement of magnetic flux quantization in a superconducting ring[68]. However the phonon mediated attractive interaction between

electrons as the origin of pair formation as in BCS theory, has been under doubt in high-T_c superconductors[26]. Indeed, a number of experimental facts point to a mechanism of pairing originating from strong electronic correlations in the CuO_2 planes. One fact that stands out in this regard is the symmetry of the superconducting gap, $\Delta(\mathbf{k})$. In BCS superconductors, the superconducting gap is isotropic in $\mathbf{k}$-space, or in other words, the symmetry of the pair wavefunction is of *s*-wave type. In contrast, the superconducting gap in high-T_c superconductors is found to be anisotropic in $\mathbf{k}$-space. In fact it has a predominantly $d_{x^2-y^2}$-wave (*d*-wave) symmetry as clearly evidenced from photoemmission and tunneling spectroscopy (see Ref. [46] for a review). Angle-resolved photoemission spectroscopy (ARPES)[21, 69] can directly investigate the topology of the Fermi surface and momentum dependence of the superconducting gap. The highly anisotropic nature of the SC gap obtained by a ARPES

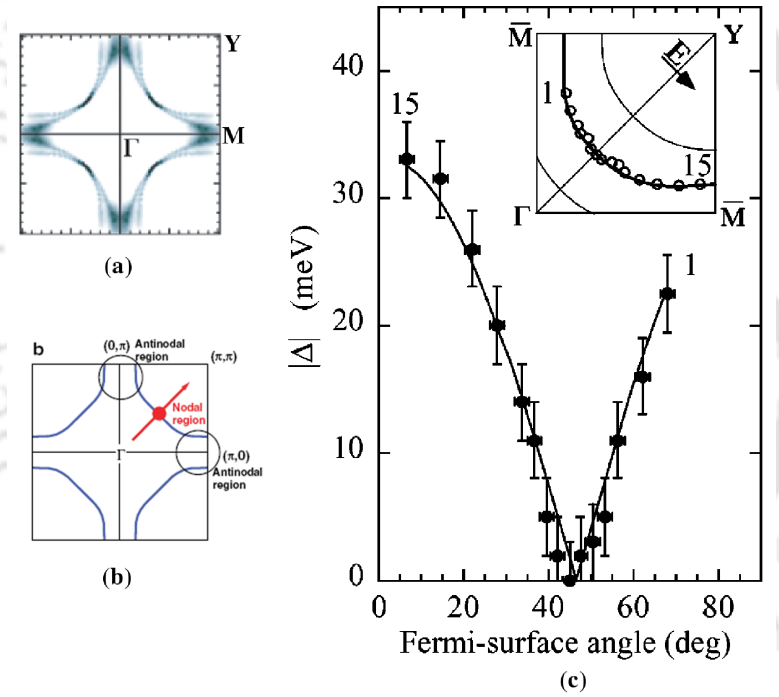

FIGURE 1.7: Anisotropy of the SC gap in high-T_c superconductors. (a) Normal-state Fermi surface in Bi2212 determined by ARPES (Source: Ref. [70]). (b) Schematic diagram of the Fermi surface identifying different regions (Source: Ref. [71]). (c) SC gap in Bi2212 (T_c = 87°K) measured at 13°K by ARPES plotted as function of angle along the normal-state Fermi surface. The solid line fits the data with a *d*-wave gap function, $\Delta(\mathbf{k}) = \Delta_0(\cos k_x - \cos k_y)$ (Source: Ref. [72]).

study of Bi2212[72] is shown Fig. 1.7. The underlying Fermi surface of the compound identifying the high symmetry points is also shown. The figure shows that the magnitude of the

SC gap is maximum near the $(0, \pi)$ region (antinodal region) and is nearly zero near the region along Γ-Y direction (nodal region). The experimental data for the magnitude of the SC gap agrees well with the *d*-wave gap function ($\Delta(\mathbf{k}) = \Delta_0(\cos k_x - \cos k_y)$). The sign of the *d*-wave state is confirmed by phase-sensitive tests based on the Josephson tunneling and flux quantization experiments[73, 74, 75]. Such a highly anisotropic nature of the SC gap is not expected in a superconductivity resulting from phonon mediated pairing of electrons. Instead, it is compatible with a pairing based on electronic mechanism. Also the magnitude of the gap in high-T_c superconductors, which is of the order of 20-30 meV ($|\Delta(\mathbf{k})|_{max}$ at $T = 0$), is too high (almost double the value of the energy gap in BCS superconductors) to be accounted for by a electron-phonon interaction. Another notable fact is that the ratio $2\Delta/k_BT_c$ for the BCS superconductors remains constant ($\sim$ 3.51) while it varies from 4.5 – 5.5 for high-T_c superconductors.

The ARPES in the superconducting state of high-T_c superconductors shows a number of other anomalous features that are not expected in any weak coupling theories such as the BCS theory (see Ref. [21] for a review). An well known phenomenon in this regard is the dramatic

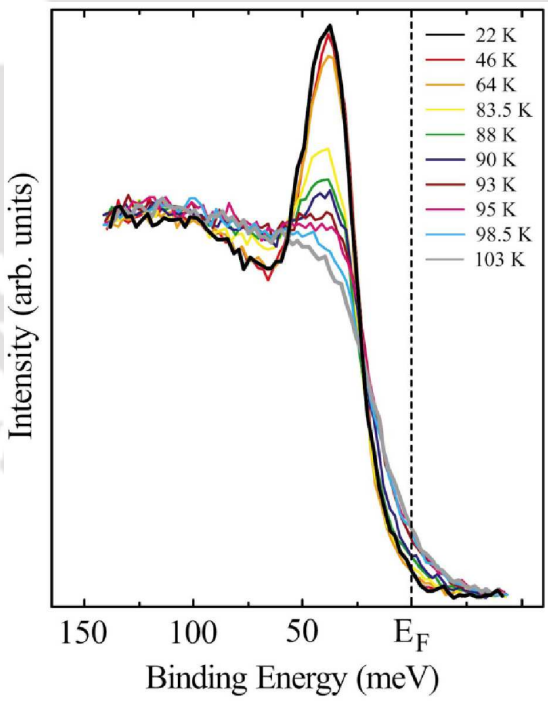

FIGURE 1.8: Temperature dependence of photoemission spectra for optimally doped Bi2212 ($T_c = 91°K$), angle integrated over a narrow cut around $(0, \pi)$ (Source: Ref. [76]).

change in the line shape of photoemission spectra near the $(0, \pi)$ point of Fermi surface as

temperature is lowered just below T_c[76, 77]. This is illustrated in Fig. 1.8 which shows ARPES spectra, angle integrated over a finite cut around $(0, \pi)$ point for optimally doped Bi2212[76]. The ARPES intensity, $I(\mathbf{k}, \omega)$ which is plotted in the figure as a function of binding energy, ω gives information about the single-particle density of states. Within certain approaximations, it is given by $I(\mathbf{k}, \omega) \propto f(\omega)A(\mathbf{k}, \omega)$, where $f(\omega)$ is the Fermi function and $A(\mathbf{k}, \omega)$ is the single-electron spectral function[21]. The figure shows that the spectra have broad line shapes above T_c. As temperature is lowered below T_c, spectral weights in the region around the Fermi level, E_F drops. The lost intensity appears in an energy level below E_F where it gives rise to a peak. This shifting of spectral intensity from the Fermi level signifies formation of the SC gap. The striking feature in the spectra below T_c is the sharpening of the peak with decreasing T. This indicates that the scattering rate of the quasiparticles which determines the linewidth of $A(\mathbf{k}, \omega)$, drops sharply below T_c underlining the role of electron-electron interaction in the superconducting state[78]. Another striking feature in the spectra below T_c is the appearance of the dip in the spectra at a binding energy that is slightly higher than that of the sharp quasiparticle peak, followed by the appearance of a broader hump. The origin of the dip is still debated. One more important indication of an unconventional pairing mechanism comes from angle-integrated photoemission spectroscopy, which gives the single-particle density of state, $N(\omega)$ $(= \sum_{\mathbf{k}} A(\mathbf{k}, \omega))$. In BCS superconductors, one electron intensity moves up in energy from the gap region. This results in a increase in net electronic kinetic energy in the SC state which is overcompensated by a gain in potential energy due to pairing. In contrast, angle-integrated spectroscopy in high-T_c cuprates[79] shows that one electron intensity is shifted downward from the superconducting gap implying a gain in kinetic energy in the SC state[26]. This demonstrates the fact that superconductivity in the high-T_c cuprates is kinetic energy driven while BCS superconductivity is potential energy driven.

Apart from these, high-T_c superconductivity is distinguished from BCS superconductivity by other facts like the coherence length, ξ. The coherence length, ξ signifies the average size of a Cooper pair. For conventional superconductors, ξ is very large, of the order of 500 Å to 10000 Å. This length is much larger than the average distance between two Cooper pairs. In high-T_c cuprates, ξ is very small in comparison. The coherence length of Cooper pair in the *ab*-planes, ξ_{ab} is $\sim$ 12 Å to 15 Å which 3 to 4 times the lattice spacing in a plane. The coherence length along *c* direction is even smaller. ξ_c is of the order of 2 Å to 5 Å, which is smaller than the interplanar distance between two CuO_2 layers.

1.2 Electronic models for high-T_c superconductors

1.2.1 Basic electronic structure

Theoretically, it has been recognized that the key player in the physics of cuprate superconductors are the CuO_2 layers which are responsible for the low lying electronic excitations in these systems. In the parent compounds of high-T_c cuprates, such as La_2CuO_4, the Cu^{2+} ions are in $3d^9$ configuration. Each Cu^{2+} ions is surrounded by six oxygen atoms in an octahedral configuration, four oxygen atoms being in a CuO_2 plane and two perpendicular to the plane (apical oxygen). The resulting crystal field splits the five degenerate Cu 3*d*-orbitals as shown schematically in Fig. 1.9[71, 80]. First the orbitals are split into e_g and t_{2g} states. A distortion

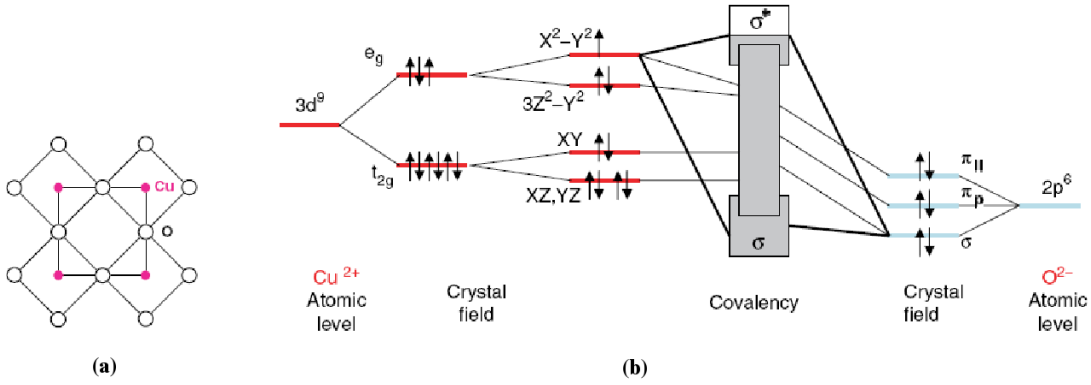

FIGURE 1.9: Electronic structure of the cuprates. (a) A CuO_2 plane. (b) Splitting of the Cu 3*d* and O 2*p* orbitals in crystal field and their hybridization. (Source: Ref. [71])

from perfect octahedron due to a shift of the two apical O atoms, causes these two levels to further split. The four lower energy orbitals, *xy*, *xz*, *yz* and $3z^2 - r^2$ are fully occupied by electrons, while the orbital with the highest energy, i.e. $x^2 - y^2$ is half-filled. Since the energies of the Cu 3*d* orbitals and O 2*p* orbitals are close, there is a strong hybridization between them. As a result, the antibonding Cu $3d_{x^2-y^2}$ - O $2p_{x,y}$ hybridized orbital lies topmost in the spectrum.

1.2.2 Three-band Hubbard model

Thus the electronic state of the cuprates can be described by a three-band Hubbard Hamiltonian corresponding to electronic motion in one Cu $d_{x^2-y^2}$ and two O $p_{x,y}$ orbitals per unit

cell[81, 82]. In terms of a hole notation, where the vacuum is defined as all the orbitals in Fig. 1.9 occupied, the Hamiltonian can be written as,

$$\begin{aligned}\mathcal{H} &= -t_{pd}\sum_{\langle ij\rangle,\sigma}\left(p^{\dagger}_{j\sigma}d_{i\sigma}+h.c.\right)-t_{pp}\sum_{\langle jj'\rangle,\sigma}\left(p^{\dagger}_{j\sigma}p_{j'\sigma}+h.c.\right)\\ &+\epsilon_d\sum_{i\sigma}n^{d}_{i\sigma}+\epsilon_p\sum_{j\sigma}n^{p}_{j\sigma}+U_d\sum_{i}n^{d}_{i\uparrow}n^{d}_{i\downarrow}+U_p\sum_{j}n^{p}_{j\uparrow}n^{p}_{j\downarrow}\\ &+U_{dp}\sum_{\langle ij\rangle,\sigma\sigma'}n^{d}_{i\sigma}n^{p}_{j\sigma'} \qquad (1.1)\end{aligned}$$

The operator $d^{\dagger}_{i\sigma}$ creates a Cu $3d_{x^2-y^2}$ hole of spin σ at site i and $p^{\dagger}_{j\sigma}$ creates a O $2p_{x,y}$ hole at site j. $n^{d}_{i\sigma}=d^{\dagger}_{i\sigma}d_{i\sigma}$ is the number operator for holes and so is $n^{p}_{j\sigma}$. $\langle ij\rangle$ refers to pairs of nearest neighbour (nn) i (Cu) and j (O) sites. The hopping term t_{pd} corresponds to hybridization between two nn copper d and oxygen p orbitals, while the t_{pp} represents direct hopping between two nn oxygen p orbitals. ϵ_d and ϵ_p are the energies of a hole in the d and p orbitals, respectively. U_d and U_p are two positive constants that represent the repulsive potential between two holes occupying same d and p orbitals, respectively. Finally, U_{pd} represent the interaction potential between two holes occupying two nn d and p orbitals.

The values of different parameters in the Hamiltonian can be obtained from electronic band structure calculations. These values estimated thus[83] are listed in Table 1.1. It shows

$\epsilon_p-\epsilon_d$	t_{pd}	t_{pp}	U_d	U_p	U_{dp}
3.6	1.3	0.65	10.5	4	1.2

TABLE 1.1: Values of various parameters (in eV) in the three-band Hamiltonian obtained from electronic band structure calculation[83]

that the hole energy in a copper d orbital, ϵ_d is lower than that in oxygen p orbital, ϵ_p. As a result, the first hole added to the system will occupy the Cu $3d$ orbitals as is observed in undoped CuO_2 planes. This is schematically shown in Fig. 1.10. The energy to doubly occupy the Cu d orbitals, U_d is $\sim$ 10.5 eV which is very large compared with all other energies in the problem. The lowest energy excitation in the system is the charge transfer excitation, in which a hole from d orbital hops to a nearest p orbital with amplitude $-t_{pd}$. However as $(\epsilon_p-\epsilon_d)$ is sufficiently large compared with t_{pd}, the hole is essentially localized in the d orbital forming a magnetic moment in the corresponding Cu atom. When an extra hole is added to the system by way of doping, the new hole will occupy a oxygen p orbital because of the large

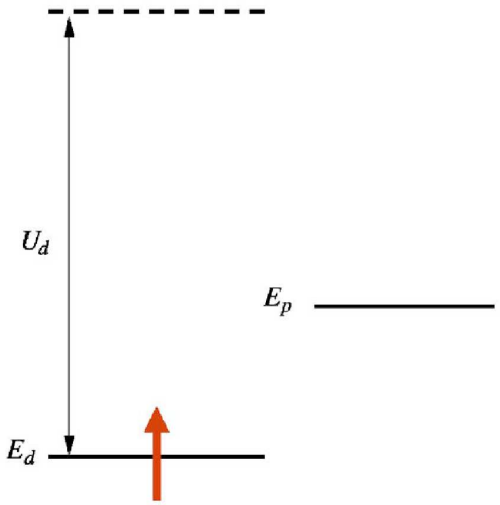

FIGURE 1.10: The copper $3d_{x^2-y^2}$ and oxygen $2p_{x,y}$ orbitals in hole picture. In undoped CuO_2 planes, a single hole occupies the copper d orbital. (Source: Ref. [27])

energy cost, U_d in doubly occupying a d orbital. The holes can hop via t_{pd} and thus can get delocalized to form a metallic state.

1.2.3 One-band models

The full description of hole doping the three-band model is complicated because of the large number of parameters involved. However it has been realized that the low-energy physics of the problem can be understood in terms of an effective one-band model. The idea is that, a doped hole resonates between the four oxygen sites surrounding a copper atom[84]. These states combine with the spin of the central copper atom to form a singlet, known as the Zhang-Rice singlet. Thus the doped hole originally located in an oxygen atom get replaced by a spin singlet state centered at copper atom. This is equivalent to removing a copper spin from the square arrangement of copper spins in an undoped CuO_2 layer. The Zhang-Rice singlet can hop from site to site with an effective hopping integral, t of the order of $t_{pd}^2/(\epsilon_p - \epsilon_d)$. In this picture, the oxygen atoms are no longer present in the system. This is schematically shown in Fig. 1.11.

By focusing on the low-lying energy states of the singlet, the hole doped three-band model simplifies to an effective one-band model. In the limit of large $(\epsilon_p - \epsilon_d)$ this maps on the t-J

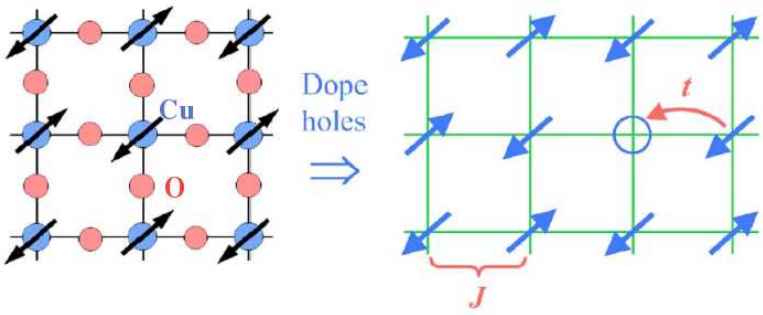

FIGURE 1.11: A two dimensional copper oxide layer (left) simplified to a picture in one-band model (right). (Source: Ref. [27])

model[85], given by

$$\mathcal{H} = \mathcal{P}_G \left[-\sum_{\langle i,j\rangle,\sigma} t_{ij} \left(c^{\dagger}_{i\sigma} c_{j\sigma} + h.c. \right) + J \sum_{\langle i,j\rangle} \left(\boldsymbol{S}_i . \boldsymbol{S}_j - \frac{1}{4} n_i n_j \right) \right] \mathcal{P}_G \tag{1.2}$$

Here $c^{\dagger}_{i\sigma}$ ($c_{i\sigma}$) is the fermion operator that creates (annihilates) an electron of spin σ at site i while n_i is the number operator given by, $n_i = \sum_\sigma c^{\dagger}_{i\sigma} c_{i\sigma}$. $\boldsymbol{S}_i$ is the spin operator at site i, given by $S^{\alpha}_i = \psi^{\dagger}_i (\frac{1}{2}\boldsymbol{\sigma}_\alpha)\psi_i$, where $\psi_i = \begin{pmatrix} c_{i\uparrow} \\ c_{i\downarrow} \end{pmatrix}$ and $\boldsymbol{\sigma}_\alpha$ ($\alpha = x, y, z$) are the Pauli spin matrices. t_{ij} is the hopping integral between two nearest neighbour sites $\langle ij \rangle$ and J is the antiferromagnetic exchange interaction between two spins at $\langle i, j \rangle$. The operator, $\mathcal{P}_G = \prod_i (1 - n_{i\uparrow} n_{i\downarrow})$ is the *Gutzwiller* projector that restricts the Hilbert space into a subspace of singly occupied sites. The parameter values of the Hamiltonian determined from theory[86] and experiment[39, 87] are found to be, $t_{ij} = t = 0.44$ eV and $J = 0.13$ eV.

In addition to the above, another model relevant to the high-T_c superconductors that has been widely studied, is the two dimensional one-band Hubbard model[88]. This Hamiltonian is written as,

$$\mathcal{H} = -\sum_{\langle ij\rangle,\sigma} t_{ij} \left(c^{\dagger}_{i\sigma} c_{j\sigma} + h.c. \right) + U \sum_i n_{i\uparrow} n_{j\downarrow} \tag{1.3}$$

The first term represents the hopping of electrons from one site to another as before and the second term represents the repulsive Coulomb energy between two spins occupying the same site. The on-site interaction potential, U in the model plays the role of the charge transfer gap, $\Delta = \epsilon_p - \epsilon_d$ in the electronic structure. The value of U relevant to the high-T_c cuprates is $\sim 8t$,

which is regarded as moderately large. In the strong coupling limit, it can be shown that the Hubbard model reduces to the *t*-*J* model as far as low-energy excitations are concerned.

1.3 Theoretical studies of high-T_c superconductors

1.3.1 Alternative approaches

From the large number of experimental evidences showing various anomalous features of cuprate superconductors, it was very clear from the beginning that superconductivity in these materials can not be described by the BCS theory[89] of conventional superconductors. The most basic questions are the origin of pairing and the nature of the superconducting state in these materials. Various theories were proposed that try to address these issues as well as explain other observed anomalies in the cuprates, but many of them are invalidated by one experimental evidence or the other[26].

The initial idea was to construct theories in the BCS framework that consider the presence of strong planar antiferromagnetic correlations in high-T_c superconductors. These Fermi-liquid based theories include the spin-bag theory[90], spin-fluctuation based theories[91, 92] and theories based on Van Hove singularity scenario[93, 94] among others. Another approach that treats antiferromagnetism and superconductivity on the same footing is the SO(5) theory[95]. On the other hand, a number of other theories have been proposed that are based on quite new physics. The most notable ones are the bipolaron theory[96], the marginal Fermi-liquid theory (MFT)[97] and the Luttinger liquid theory[26]. The bipolaron theory is based on the fact that an electron motion is accompanied by a lattice distortion due to strong electron-phonon coupling. The resulting motion is described by a polaron. A bipolaron is a bound pair of two polarons which are mutually attracted by lattice distortion. The bipolarons are spin singlets and form a Bose condensate at the SC transition temperature. The marginal Fermi-liquid theory proposes that in high-T_c superconductors, electron-electron interactions are so strong that it drives the quasiparticle weight, Z, the jump in momentum distribution at the Fermi level, towards zero. However, it assumes that $Z \rightarrow 0$ very slowly (logarithmically) so that a Fermi surface remains just barely. In such a state, other physical properties of the system show non-Fermi liquid behaviour.

Amongst the various theories put forward so far, the theory due to Anderson[26] seems to be the most rigorous. The theory is able to explain many of the experimental observations in high-T_c superconductors. According to this theory, superconductivity originates in the individual CuO_2 layers of high-T_c superconductors due to pairings caused by some electronic mechanism. A single-band Hubbard model of intermediate coupling strength is good enough to describe the electronic excitations in a CuO_2 layer. The electronic system described by the 2D Hubbard model at finite T exhibits Luttinger liquid behaviour, which are characterized by features, such as, fractionation of quantum numbers, a power-law singularity of momentum distribution at the Fermi surface, unusual exponents of correlation functions etc. Collective excitations in Luttinger liquids are described by spin-1/2 spinons and $\pm e$ spinless holons which propagates with different velocities leading to spin-charge separation. The c-axis conductivity in the normal state of high-T_c superconductors is blocked due the confinement property of Luttinger liquids which prohibits coherent single particle hopping across the planes. However in the superconducting state, pairs can tunnel across the layers coherently lowering the kinetic energy substantially. This interlayer pair tunneling (ILPT) amplifies superconductivity preformed in the CuO_2 planes and provides almost all the condensation energy in these superconductors leading to the high values of T_c. Though quite successful, the theory is still incomplete in the sense that, it does not explain the mechanism of pairing in the CuO_2 planes. Moreover, certain experiments seem to contradict the ILPT scenario. As an example, the measured c-axis penetration depth in $Tl_2Ba_2CuO_{6+x}$[98, 99] is found to differ from the value predicted by the ILPT theory by roughly one order of magnitude.

1.3.2 Success with the t-J model

The electronic system described by the t-J Hamiltonian is strongly correlated because of the projection operator, $\mathcal{P}_G$ in it (Eq. (1.2)) which prohibits doubly occupied sites. Theoretical studies on the t-J model have shown that the strong correlations present in the model is enough to capture the essential physics of high-T_c superconductors (see Ref. [27] for a review).

The t-J model has often been used to study high-T_c superconductivity from the viewpoint of doping an antiferromagnetic Mott insulator[27]. The undoped compounds of high-T_c superconductors behave as Mott insulators. It has one electron per unit cell but is insulating by virtue of strong Coulomb repulsion between two electrons on the same site. In the CuO_2

planes, virtual hopping to a doubly occupied state leads to an antiferromagnetic exchange coupling, J between two nearest neighbour Cu spins[100]. In fact, a variety of experimental and theoretical studies[101, 102, 103, 104] have shown the copper spin systems in the CuO_2 planes to be a close realization of the spin-1/2 2D AF Heisenberg model, $\mathcal{H}_J = J \sum_{\langle ij \rangle} \boldsymbol{S}_i.\boldsymbol{S}_j$, which is same as the *t-J* model at half-filling.

To describe evolution of the ground state and excited states of *t-J* model with hole doping, an important idea introduced by Anderson[85] is the concept of resonating-valence-bond (RVB) liquid (see Ref. [105] for a review). The RVB state can be described as a coherent superposition of states in which various pairs of electrons form singlet bonds between them. It is a unique spin-singlet ground state of the spin-1/2 AF Heisenberg Hamiltonian and have no long range AF order. It was suggested that the RVB state would give a better description of the ground state of the *t-J* model doped with holes. The Néel ordered AF state is incompatible with hole doping which can be seen as follows. As soon as holes are introduced into an undoped CuO_2 plane, it will tend to hop around in order to lower its kinetic energy. In an Néel antiferromagnetic background, this will cause two nearest neighbour spins to align ferromagnetically thereby destroying the AF order and increasing energy. On the other hand, a better compromise between the hole kinetic energy and spin exchange energy can be achieved, if instead the holes are envisioned to hop around in the background of a liquid of spin-singlet states. These ideas were quantified by a number of analytical and numerical calculations. Elementary excitations in the RVB state are obtained by breaking some of the singlet bonds in it. It give rise to neutral spin-1/2 fermionic excitations called spinons. When doped, the holes combine with the spinons to form bosonic excitations called holons[106, 107]. A spinon carries spin but no charge whereas a holon carries charge but no spin, thus spin and charge excitations are separated.

An important realization regarding the RVB state is that it can be generated as a Gutzwiller projection of a suitable trial wavefunction,

$$|\Psi_{RVB}\rangle = \mathcal{P}_G |\Psi_0\rangle \tag{1.4}$$

where $\mathcal{P}_G$ is given by Eq. (1.2). The physical properties of the *t-J* model can be readily studied within such a wavefunction because it takes care of the constraint no doubly occupied site. However the difficulty lies in the implementation of $\mathcal{P}_G$. Analytically, it has been implemented

approximately in a variety of ways. Numerically, the restriction of the projection operator has been enforced exactly using computers.

The slave-boson mean field formalism for the *t*-*J* model[108, 109, 110] is a powerful analytical method to implement the projection operator. In this formalism the effect of projection is replaced by introducing an auxiliary boson field and the resultant Hamiltonian is decoupled using mean-field approaximations. The incorporation of fluctuations around the mean-field provides a way for systematic extension of the slave-boson mean field theory (SBMFT). This is done in the U(1) gauge theory[111, 112, 113] and the SU(2) gauge theory[114] for the *t*-*J* model. These studies showed that the *t*-*J* model indeed supports superconductivity with a *d*-wave pairing symmetry ($\Delta_{\mathbf{k}} = \Delta(\cos k_x - \cos k_y)$) and a pseudogap phase in underdoped region. This is illustrated in Fig. 1.12 which shows the phase diagram for the *t*-*J* model obtained by the SU(2) mean-field theory[114]. The figure shows six different phases for the *t*-*J* model.

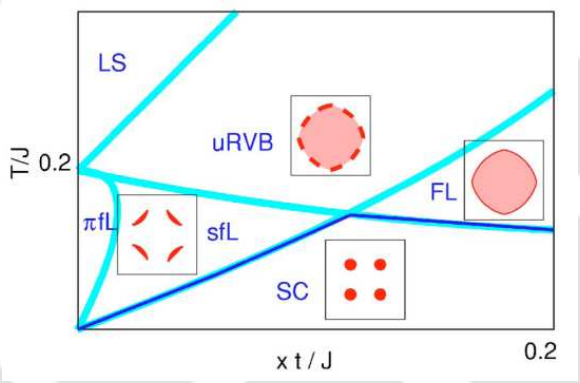

FIGURE 1.12: SU(2) mean-field phase diagram for the *t*-*J* model for $t/J = 1$, as a function of temperature, T and hole concentration, x. Also shown are the Fermi surface topology in various phases which consists of Fermi surface, Fermi arcs and Fermi points (Source: Ref. [27]).

The localized spin phase (LS), uniform RVB (μRVB), π-flux Liquid (πfL) and the staggered flux liquid (sfL) phases all correspond to some unusual metallic states[27]. As temperature is lowered, the μRVB state changes into the πfL or sfL phases at underdoping. A gap opens up near $(0, \pi)$ points of the Fermi surface and these two phases correspond to the pseudogap phase. At low T and away from half-filling, the phase is a *d*-wave superconducting state of the electrons. The Fermi surface is gaped except along (π, π) directions. The FL phase represents a Fermi liquid metallic state of the electrons.

The renormalization mean-field theory (RMFT) due to Zhang *et al*[115] provides another way of tackling the projection operator in the *t-J* Hamiltonian (see Ref. [116] for a review). The RMFT is based on the Gutzwiller approaximation (GA)[117] within which the effects of projection are absorbed by statistical weight factors, called renormalization factors. In GA, one writes

$$\frac{\langle\Psi_0|\mathcal{P}_G\hat{O}\mathcal{P}_G|\Psi_0\rangle}{\langle\Psi_0|\mathcal{P}_G\mathcal{P}_G|\Psi_0\rangle} \approx O_s\frac{\langle\Psi_0|\hat{O}|\Psi_0\rangle}{\langle\Psi_0|\Psi_0\rangle} \tag{1.5}$$

Where the expectation value of $\hat{O}$ within the projected state $\mathcal{P}_G|\Psi_0\rangle$ is approaximated by a corresponding statistical weight O_s multiplying the expectation value within the unprojected state. This approaximation for the kinetic and exchange energy terms of the *t-J* model leads to two renormalization factors, g_t and g_s respectively, given by

$$g_t = 2x/(1+x) \quad \text{and} \quad g_S = 4/(1+x)^2 \tag{1.6}$$

where x represent the average concentration of holes in the lattice. Consequently the *t-J* model gets modified to

$$\mathcal{H}_{eff} = -g_t t\sum_{\langle ij\rangle,\sigma} t_{ij}\left(c^{\dagger}_{i\sigma}c_{j\sigma} + h.c.\right) + g_s J\sum_{\langle ij\rangle}\left(\boldsymbol{S}_i.\boldsymbol{S}_j - \frac{1}{4}n_i n_j\right) \tag{1.7}$$

If the renormalized *t-J* Hamiltonian is treated within the Hartree-Fock-BCS approaximation, then one arrive at a modified BCS gap equation[115]. Optimum solution of the gap equation gives a superconducting gap, Δ_k which have a *d*-wave pairing symmetry. The SC state is characterized by an order parameter (OP) defined as,

$$\Phi = \langle c^{\dagger}_{i\uparrow}c^{\dagger}_{j\downarrow}\rangle \tag{1.8}$$

In GA, Φ is renormalized by g_t as $\Phi \approx g_t\Delta$, where Δ is the maximum of Δ_k. Results for Δ and Φ calculated thus were compared by Anderson *et al*[105] with the SC gap obtained by ARPES and the corresponding T_c for Bi2212. Here we reproduce the comparison in Fig. 1.13. As seen in the figure, Δ is maximum near half-filling and decreases uniformly with doping. The parameter Δ corresponds to the crossover temperature T^* which marks the onset of the pseudogap in underdoped cuprates. On the other hand, Φ has a non-monotonic dependence on x resembling the variation of T_c with doping. The comparison shows that the theoretical

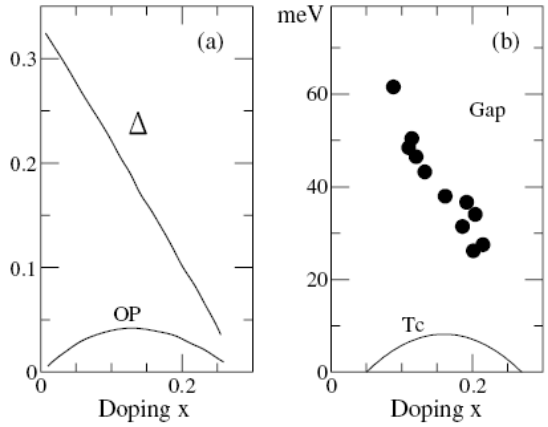

FIGURE 1.13: (a) The *d*-wave gap parameter, Δ and the SC order parameter, Φ as a function of hole doping, x in the *t*-*J* model for $J/t = 0.2$ calculated using the RMFT[115]. (b) The spectral gap (in meV) for Bi2212 as measured by ARPES[118] and T_c as a function of hole doping. (Source: Ref. [105]).

prediction agrees very well with the results obtained from experiments.

The properties of the *t*-*J* model as well as the Hubbard model have also been extensively investigated using a variety of numerical methods (see [24] for a review). These include various Quantum Monte Carlo (QMC) techniques[119] for finite size lattices, Lanczos diagonalization of small clusters[120, 121], density-matrix-renormalization group (DMRG)[122] studies of *n*-leg ladders, dynamical mean-field theory (DMFT)[123] for bulk lattice etc. The early proposal of using the projected RVB wavefunctions as quantum states of the *t*-*J* model was implemented numerically in Variational Monte Carlo (VMC) calculations by Gros[124, 125] and others (see §1.3.3). Studies using all these techniques show that the *t*-*J* model supports an antiferromagnetic phase at half-filling, a pseudogap phase at underdoping and a *d*-wave superconducting phase for a wide range of hole doping away from half-filling. Particularly, Sorella and co-authors[126, 127, 128, 129, 130] using much more refined calculations based on several numerical techniques have shown the *d*-wave SC state to be a robust ground state of the two dimensional *t*-*J* model away from half-filling. Thus it is clear that the *t*-*J* Hamiltonian is a worthwhile candidate for studying superconductivity in the high-T_c cuprates.

1.3.3 Variational Monte Carlo studies

The Variational Monte Carlo (VMC) method is a powerful numerical technique to study Gutzwiller projector based variational wavefunctions. Unlike the analytical methods describe above, VMC allows one implement the Gutzwiller projector, $\mathcal{P}_G$ exactly. It can be employed to study the physical properties of a variational wavefunction for a wide range of parameter values. The fermion sign problem that plague the other Quantum Monte Carlo methods is absent here. However it a variational study and hence the obtained results are dependent on the choice of the variational wavefunction. Also one is limited to studying mainly the ground state properties only. Nevertheless, VMC has been extensively used over the years to study the physical properties of various lattice fermion models with great success.

The Variational Monte Carlo (VMC) method was first applied to study the ground state properties of ^{4}He[131] and later on it was extended to study fermionic systems (^{3}He)[132, 133]. Since then the method has been applied to different lattice fermion models to study various ground state phases, such as a Fermi liquid metallic, a paramagnetic, a long-range AF ordered state etc[134, 135, 136]. Following the idea of using RVB type wavefunctions to study the quantum states of high-T_c superconductors, Gros[124, 125] applied the VMC technique to the t-J Hamiltonian by taking a projected BCS superconducting state with d-wave pairing symmetry as trial wavefunction. The study showed that the d-wave SC state is indeed a variational ground state of the t-J model for a wide range of hole doping. Similar result was obtained by Yokoyama *et al*[137] who studied the t-J model using a grand canonical VMC. In an extensive study of the phase diagram of a two dimensional t-J model using VMC by Yokoyama *et al*[138], several pairing symmetries for the SC state were considered and it was found that the d-wave state give lower energy for t, J parameter values that correspond to experimental results. The phase diagram in the $n - J/t$ plane, n being the electron density, is shown in Fig. 1.14. As seen in figure, at half-filling ($n = 1$) and for $J/t \lesssim 1.4$, the phase is AF insulating. The $d_{x^2-y^2}$-wave SC phase emerges as the stable ground state away from half-filling for a broad range of n and J/t. As hole doping is increased, the SC phase makes transition to a paramagnetic metallic phase at a critical density that depends on J/t. For low electron density and a range of larger J/t, a SC state with extended s-wave symmetry ($\Delta_{\mathbf{k}} = \Delta(\cos k_x + \cos k_y)$) (S) appears in the phase diagram. For higher value of J/t, we get a phase separated (P.S.) state in which holes and electrons get separated into islands of hole and electron rich regions. The ferromagnetic state (FM) is obtained for $J/t \to 0$ and $n \gtrsim 0.7$. The

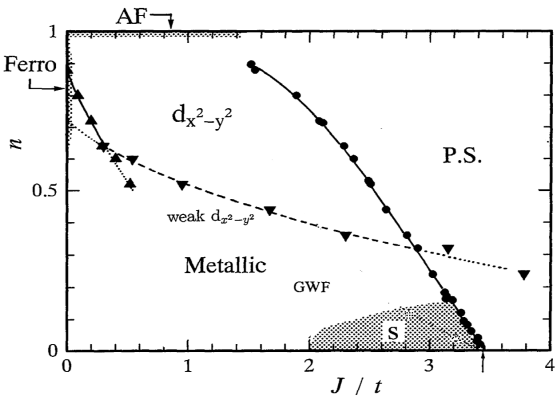

FIGURE 1.14: Ground state phase diagram of the 2D t-J model as a function of electron density, n and exchange coupling J/t obtained by VMC (Source: Ref. [138]).

interplay of antiferromagnetism and superconductivity in the two-dimensional t-J model has also been examined using VMC by several authors[139, 140] and it was found that AF long range order coexists with the d-wave SC phase in the underdoped region.

The usefulness of VMC was demonstrated more recently by Paramekanti *et al*[141, 142], who extensively studied the 2D Hubbard model in strong coupling limit using VMC by considering the $d_{x^2-y^2}$ wave SC state as the variational wavefunction. Several key physical properties were calculated and comparison of the results with experimental data on cuprates showed fairly good agreements. An exciting prospect is the application of VMC to study the finite temperature properties of the superconducting state. This has already started in recent past and various aspects of the quasiparticle excitation spectrum in the Gutzwiller projected BCS wavefunction are being examined using this technique[143, 144, 145]. Thus VMC can be expected to give more wider information about the crucial low-lying excited states in high-T_c superconductors in future.

1.4 Interlayer coupling

It is generally agreed that the key physics of the cuprate superconductors lies in a single CuO_2 plane. The electronic system in these copper oxide layers are strongly correlated. Theoretical studies over the years have shown that, indeed such a two dimensional strongly interacting

electron system can give rise to many of the unusual properties observed in high-T_c superconductors. Thus a number of theories proposed for the high-T_c superconductors have concentrated mainly on the isolated copper oxide layers and the physics that emerges from the presence of more than one CuO_2 layer have received limited attention.

Nevertheless, interlayer coupling between different CuO_2 layers in the cuprate superconductors influences many of its physical properties (see Ref. [55] for a review). The crystal structure of these materials consists well separated blocks of n closely spaced CuO_2 layers, where n can be 1, 2, 3 or 4 (see §1.1.1). The separation between the layers in a block or unit cell in multilayered compounds is very small ($\sim$ 3.5 Å), whereas the blocks itself are separated by large distances ($\sim$ 6-8 Å). Therefore the coupling between different copper oxide layers within a unit cell (intracell) is generally distinguished from that between two adjacent blocks of the closely spaced CuO_2 layers (intercell coupling). The nature of intercell coupling in the cuprate superconductors and its role in the observed large c-axis anisotropies in various physical properties has been intriguing. For example, electronic band structure calculations predict that c-axis charge transport in the normal state should be metallic due to the finite hopping integral between layers[80]. However experimental evidences suggest that single particle hopping of electrons across the CuO_2 layers is highly incoherent. Several mechanism have been proposed to explain this phenomenon, such as, c-axis charge confinement due to a non-Fermi liquid ground state in the layers[146, 147, 148], renormalization of the interlayer hopping by inplane scattering[149] etc.

As regard to the CuO_2 layers in a single unit cell of multilayered cuprates, it is reasonable to expect coherent single particle motion across the layers because of their proximity. In fact, band structure calculations on bilayered superconductors, such as $Bi_2Sr_2CaCu_2O_{8+x}$ (Bi2212), predict a splitting of the main electronic band crossing the Fermi level into a bonding $\varepsilon_+(\mathbf{k})$ and an antibonding $\varepsilon_-(\mathbf{k})$ band, with $\mathbf{k}$ representing a two dimensional wavevector in the first Brillouin zone for a single CuO_2 layer[150]. Such a splitting would originate from a coherent hopping electrons between the two CuO_2 layers in a unit cell. Further, calculations show that the splitting is $\mathbf{k}$ dependent and can be quantified as,

$$t_\perp(\mathbf{k}) = \frac{t_\perp}{4}\left[\cos(k_x a) - \cos(k_y a)\right]^2 \tag{1.9}$$

with $t_\perp$ being $\sim$ 0.1 – 0.15 eV. Thus the splitting is maximum at $(0,\pi)$ or $(\pi,0)$ points and zero along the (π,π) direction. However, early ARPES study on Bi2212 reported absence of

any such bilayer band splitting[151]. But later ARPES studies with improved resolution on overdoped Bi2212 have clearly shown the presence of the band splitting as suggested by band theory[152, 153]. More recently, finite bilayer band splittings in optimally doped Bi2212 and YBCO have been observed even in the nodal region[154, 155, 156].

The implications of these interlayer couplings on the physical properties of the cuprate superconductors are profound. The famous peak-dip-hump structure observed in the ARPES spectra of bilayer superconductors near the $(\pi, 0)$ point of the Fermi surface[76, 77, 157] is shown to be a consequence of the bilayer splitting (see [158] and references therein). In the magnetic excitation spectra away from half-filling, a commensurate (π, π) resonance peak in inelastic neutron scattering data is observed only in bilayer materials, such as, YBCO[159, 160] and Bi2212[161], whereas the the feature is absent in monolayer LSCO[162]. Further a gap in the spin spectrum observed in bilayered YBCO constitutes another distinguishing feature when compared with the monolayer compounds[163]. In the superconducting state, tunneling of Cooper pairs across the layers is believed to play a crucial role in high-T_c superconductors[26]. It has been proposed that interlayer pair tunneling provides the large condensation energy in high-T_c cuprates leading to the high values of superconducting transition temperature. In fact, the transition temperature, T_c of multilayered compounds are much higher than that of their single layered counterparts with the T_c of different members in homologous series of compounds increasing linearly with the number, n of CuO_2 layers per unit cell (for $n \leq 3$) (see §1.1.1). However, reliable theoretical work on multilayered systems are very few and hence the role played by the interplanar couplings in determining the physical properties, especially in the superconducting state is largely left unexplored. This is the motivation for us to proceed with the current project on coupled bilayered systems.

Chapter 2

Bilayer t-J model and variational Monte Carlo method

2.1 Introduction

In this chapter, we introduce the model for bilayer superconductors used in this study. Previous results for this model in literature are discussed briefly. Next we describe the variational Monte Carlo method which we use for studying the model. The formalism and the algorithm for the method are described in details. For verification of our codes, we show comparison of our results with that of the published works.

The second part of the chapter (§2.4) briefly deals with a problem which is somewhat different from the main focus of the thesis. Here we have studied the effects of nonmagnetic impurities on the magnetic properties of the Hubbard model in a two dimensional lattice and a two-leg ladder using the Quantum Monte Carlo method. The results are interesting and agree with experiments on impurity doping in the cuprates.

2.2 Bilayer t-J model

Often the first step in any theoretical study of a physical system is to model the system by a representative Hamiltonian in such a way that it remains tractable to the available tools of

study. In our case, the task is to decide on a minimal Hamiltonian that would represent the bilayered superconductors, such as, $YBa_2Cu_3O_{6+x}$ (YBCO), $Bi_2Sr_2CaCu_2O_{8+x}$ (Bi2212) etc. We have seen that (§1.3.2) a single CuO_2 layer in the high-T_c cuprates is well described by a two dimensional *t-J* Hamiltonian (Eq. 1.2). Therefore it is reasonable to extend this Hamiltonian to the closely coupled CuO_2 planes in the bilayer compounds mentioned above. Here we have considered a Hamiltonian for bilayer superconductors where each layer is represented by the two dimensional *t-J* model and a single particle interlayer hopping and an exchange term connects the two layers. Thus our model for bilayer superconductors is given by,

$$\begin{aligned}\mathcal{H} &= \mathcal{P}_G\Bigg[-t\sum_{\langle i,j\rangle\sigma}\left(c^{\dagger}_{i\sigma}c_{j\sigma}+h.c.\right)+J\sum_{\langle i,j\rangle}\left(\boldsymbol{S}_i.\boldsymbol{S}_j-\frac{1}{4}n_in_j\right)\\ &\quad -t_{\perp}\sum_{\langle\langle i,k\rangle\rangle\sigma}\left(c^{\dagger}_{i\sigma}c_{k\sigma}+h.c.\right)+J_{\perp}\sum_{\langle\langle i,k\rangle\rangle}\left(\boldsymbol{S}_i.\boldsymbol{S}_k-\frac{1}{4}n_in_k\right)\Bigg]\mathcal{P}_G \qquad (2.1)\end{aligned}$$

Here t and J are the planar hopping and exchange integrals respectively. The fermion operators $c_{i\sigma}$ ($c^{\dagger}_{i\sigma}$) annihilates (creates) an electron of spin σ at site i. $\boldsymbol{S}_i$ is the spin operator at site i, given by $S^{\alpha}_i=\psi^{\dagger}_i(\frac{1}{2}\boldsymbol{\sigma}_{\alpha})\psi_i$, where $\psi_i=\begin{pmatrix}c_{i\uparrow}\\ c_{i\downarrow}\end{pmatrix}$ and $\boldsymbol{\sigma}_{\alpha}$ ($\alpha=x,y,z$) are the Pauli spin matrices. The Gutzwiller projection operator, $\mathcal{P}_G=\prod_i(1-n_{i\uparrow}n_{i\downarrow})$ imposes the condition of no double occupancy of the sites. The summation index $\langle i,j\rangle$ runs over the pairs of nearest neighbour sites i, j in each individual layers. Thus, the first two terms in Eq. (2.1) represent the *t-J* Hamiltonian for two uncoupled single layers. The last two terms in the equation provide the interlayer couplings via the single particle interplanar hopping and exchange integral, $t_{\perp}$ and $J_{\perp}$, respectively. The summation index $\langle\langle i,k\rangle\rangle$ runs over the pairs of interplanar nearest neighbor sites i, k. It may be mentioned that the observed band splitting in bilayer superconductors due to single particle interlayer hopping is anisotropic in $\boldsymbol{k}$-space (planar) as described in §1.4. However here we consider a $\boldsymbol{k}$-independent hopping integral, $t_{\perp}$ for simplicity.

Such a model has been studied previously in connection with bilayer superconductors, mostly within mean-field approaximations. Biagini[164, 165, 166] using the slave-boson mean field theory (SBMFT) studied the effects of interlayer coupling on the superconducting properties of a bilayer. He found that larger interplanar hopping strongly reduces the superconducting (SC) transition temperature, but it enhances the magnitude of the SC gap in underdoped regime. On the other hand, the interlayer exchange coupling was found to have

negligible effect. Yuan *et al*[167] studied charge transport in the bilayer *t*-*J* model with interlayer interaction and observed qualitatively similar behaviour as in single layered systems. The effects of the interlayer exchange coupling on the magnetic excitation spectra of bilayers was studied by Krüger *et al*[168]. The interlayer coupling was shown to give rise to bilayer band splitting of the magnon band. The observed magnon dispersion near the antiferromagnetic wave vector was found to be in agreements with neutron scattering experiment results. The phase diagram of the bilayer *t*-*J* Hamiltonian as a function of the interlayer parameters and hole doping was examined using SBMFT by Zhao *et al*[169] who identified several flux phases apart from the *d*-wave SC state as the stable states of the Hamiltonian at various parameter values. Zhou *et al*[170] considered a similar model to study the doping dependence of the spin resonance peak in the odd and even channels of bilayer superconductors. Recently, Yamase *et al*[171] in a comprehensive study, explained the magnetic excitations and their anisotropy in the bilayer YBCO on the basis of the bilayer *t*-*J* model.

2.3 The variational Monte Carlo method

The method we choose here for studying the bilayer *t*-*J* Hamiltonian is the variational Monte Carlo (VMC) technique. It is essentially a variational study where calculations are carried out using the Monte Carlo technique. The usefulness of VMC in studying the strongly correlated electronic models of high-T_c superconductors was stated earlier in §1.3.3. As mentioned, the chief advantage of VMC is its ability to treat the constraint of no double occupancy in the *t*-*J* Hamiltonian exactly. In fact, it is trivial to implement the Gutzwiller projection operator in this technique whereas analytical methods achieve it only approaximately. Also a larger system size can be studied in comparison with exact diagonalization (ED). The details of this method in the context of the superconducting wavefunction considered in our study is described below.

2.3.1 Representation of the wavefunction in real space

A variational study starts with choosing a trial wavefunction for the ground state of the Hamiltonian. For VMC simulation, the trial wavefunction is first expressed in real space representation. Here, we demonstrate the procedure by considering a wavefunction which describes

a state of paired electrons. The wavefunction is the Gutzwiller projected BCS wavefunction which we shall consider later for studying the superconducting state of the bilayer *t-J* Hamiltonian. The wavefunction is given by,

$$|\Psi_{var}\rangle = \mathcal{P}_G \mathcal{P}_N |\Psi_{BCS}\rangle \tag{2.2}$$

where $\mathcal{P}_G = \prod_i (1 - n_{i\uparrow} n_{i\downarrow})$ is the Gutzwiller projector which imposes the condition of no doubly occupancy and $\mathcal{P}_N$ is an operator which projects out the state with a fixed electron number, N. $|\Psi_{BCS}\rangle$ is the BCS wavefunction given by,

$$|\Psi_{BCS}\rangle = \prod_{\mathbf{k}} \left(u_{\mathbf{k}} + v_{\mathbf{k}} c^{\dagger}_{\mathbf{k}\uparrow} c^{\dagger}_{-\mathbf{k}\downarrow}\right)|0\rangle \tag{2.3}$$

where $u_{\mathbf{k}}$ and $v_{\mathbf{k}}$ are the BCS coefficients which are related to each other by $|u_{\mathbf{k}}|^2 + |v_{\mathbf{k}}|^2 = 1$. The product index '$\mathbf{k}$' runs over all points in the first Brillouin zone. Eq. (2.3) describes a wavefunction with a varying number of particles which is not convenient for numerical simulation. Therefore the projection operator $\mathcal{P}_N$ in Eq. (2.2) is used to project out the states with fixed electron number. To express $|\Psi_{BCS}\rangle$ in fixed N representation, we write it as

$$\begin{aligned}
|\Psi_{BCS}\rangle &= \left(\prod_{\mathbf{k}} u_{\mathbf{k}}\right) \prod_{\mathbf{k}} \left(1 + \varphi(\mathbf{k}) c^{\dagger}_{\mathbf{k}\uparrow} c^{\dagger}_{-\mathbf{k}\downarrow}\right)|0\rangle \\
&= C' \prod_{\mathbf{k}} \exp\left(\varphi(\mathbf{k}) c^{\dagger}_{\mathbf{k}\uparrow} c^{\dagger}_{-\mathbf{k}\downarrow}\right)|0\rangle \\
&= C' \exp\left(\sum_{\mathbf{k}} \varphi(\mathbf{k}) c^{\dagger}_{\mathbf{k}\uparrow} c^{\dagger}_{-\mathbf{k}\downarrow}\right)|0\rangle \\
&= \sum_{N=0,2,\ldots} C_{N/2} \left(\sum_{\mathbf{k}} \varphi(\mathbf{k}) c^{\dagger}_{\mathbf{k}\uparrow} c^{\dagger}_{-\mathbf{k}\downarrow}\right)^{N/2} |0\rangle
\end{aligned} \tag{2.4}$$

where C', C_N are constants. $\varphi(\mathbf{k})$ represents the pairing amplitude and is given by,

$$\varphi(\mathbf{k}) = \frac{v_{\mathbf{k}}}{u_{\mathbf{k}}} = \frac{\Delta_{\mathbf{k}}}{(\varepsilon_{\mathbf{k}} - \mu) + \sqrt{(\varepsilon_{\mathbf{k}} - \mu)^2 + \Delta^2_{\mathbf{k}}}} \tag{2.5}$$

where $\Delta_{\mathbf{k}} = \Delta f(\mathbf{k})$ is the superconducting (SC) gap function, μ is the chemical potential. In general, Δ and μ are treated as the variational parameters. For the $d_{x^2-y^2}$-wave (d-wave) state $f(\mathbf{k}) = (\cos k_x - \cos k_y)$. The quantity $\varepsilon_{\mathbf{k}}$ is the free electron dispersion relation which for the

bilayer model is given by

$$\varepsilon_{\mathbf{k}} = -2t\left(\cos k_x + \cos k_y\right) - 2t_\perp \cos k_z \tag{2.6}$$

with k_z being 0 or π. Thus from Eq. (2.4), for even N we can write

$$\mathcal{P}_N|\Psi_{BCS}\rangle \equiv \left(\sum_{\mathbf{k}} \varphi(\mathbf{k}) c^\dagger_{\mathbf{k}\uparrow} c^\dagger_{-\mathbf{k}\downarrow}\right)^{N/2} |0\rangle \tag{2.7}$$

Therefore our variational wavefunction of Eq. (2.2) becomes,

$$|\Psi_{var}\rangle = \mathcal{P}_G \left(\sum_{\mathbf{k}} \varphi(\mathbf{k}) c^\dagger_{\mathbf{k}\uparrow} c^\dagger_{-\mathbf{k}\downarrow}\right)^{N/2} |0\rangle \tag{2.8}$$

The wavefunction is represented in real space by using the Fourier transformation,

$$c^\dagger_{\mathbf{k}\sigma} = \frac{1}{\sqrt{N_s}} \sum_i e^{-i\mathbf{k}\cdot\mathbf{r}_i} c^\dagger_{i\sigma} \tag{2.9}$$

so that we get,

$$|\Psi_{var}\rangle = \mathcal{P}_G \left(\sum_{ij} \varphi(\mathbf{r}_i - \mathbf{r}_j) c^\dagger_{i\uparrow} c^\dagger_{j\downarrow}\right)^{N/2} |0\rangle \tag{2.10}$$

where N_s is the number of lattice sites, $\mathbf{r}_i$ and $\mathbf{r}_j$ are the position coordinates of i_{th} and j_{th} electrons, respectively.

$$\varphi(\mathbf{r}) = \frac{1}{N_s} \sum_{\mathbf{k}} \varphi(\mathbf{k}) e^{-i\mathbf{k}\cdot\mathbf{r}} \tag{2.11}$$

The wavefunction in Eq. (2.10) in that form represent a resonating-valence-bond (RVB) state (§1.3.2) with singlets in all possible pairs of sites of the bilayered lattice. Let R be a configuration of P (=$N/2$) up and P down spins represented by a ordered set of indices, $\{\{i_1, i_2, \ldots, i_P\}, \{j_1, j_2, \ldots, j_P\}\}$, such that up spins occupy sites $i_1, \ldots, i_P$ and down spins occupy sites $j_1, \ldots, j_P$. Then the set of all fermion configurations without double occupancies is given by,

$$\begin{aligned} B_{P,N_s} \;=\; & \Big\{\{\{i_1, i_2, \ldots, i_P\},\ \{j_1, j_2, \ldots, j_P\}\} \,\Big|\, 1 \le i_1 < \ldots < i_P \le N_s, \\ & 1 \le j_1 < \ldots < j_P \le N_s \text{ with } i_m \ne j_n \text{ for any } m, n\Big\} \end{aligned} \tag{2.12}$$

Expanding the right hand side of Eq. (2.10) and rearranging the terms, the wavefunction can be written as

$$|\Psi_{var}\rangle = \sum_{R \in B_{P,N_s}} C(R)|R\rangle \tag{2.13}$$

where $|R\rangle = \left(c^{\dagger}_{i_1\uparrow}c^{\dagger}_{i_2\uparrow}\ldots c^{\dagger}_{i_P\uparrow}c^{\dagger}_{j_1\downarrow}c^{\dagger}_{j_2\downarrow}\ldots c^{\dagger}_{j_P\downarrow}\right)|0\rangle$. The summation over R excludes configurations with any doubly occupied site. The coefficients $C(R)$ can be expressed as determinants of the amplitudes $\varphi(\mathbf{r}_{i\uparrow} - \mathbf{r}_{j\downarrow})$ as

$$C(R) \equiv \begin{vmatrix} \varphi(\mathbf{r}_{i_1\uparrow} - \mathbf{r}_{j_1\downarrow}) & \cdots & \varphi(\mathbf{r}_{i_1\uparrow} - \mathbf{r}_{j_P\downarrow}) \\ \vdots & & \vdots \\ \varphi(\mathbf{r}_{i_P\uparrow} - \mathbf{r}_{j_1\downarrow}) & \cdots & \varphi(\mathbf{r}_{i_P\uparrow} - \mathbf{r}_{j_P\downarrow}) \end{vmatrix} \tag{2.14}$$

Here $\mathbf{r}_{i_p\uparrow}$ represents the position vector of the i_p*-th site* occupied by the *p-th up electron*.

2.3.2 Lattice boundary condition

For calculation of the determinantal coefficients $C(R)$ in Eq. (2.14), one needs to first calculate the amplitudes $\varphi(\mathbf{r})$ by Fourier transforming $\varphi(\mathbf{k})$ as in Eq. (2.11). However numerical evaluation of $\varphi(\mathbf{r})$ is not possible if $\varphi(\mathbf{k})$ has singularities. For example, for the $d_{x^2-y^2}$ wave SC state,

$$\varphi(\mathbf{r}) = \frac{1}{N_s}\sum_{\mathbf{k}} \frac{\Delta(\cos k_x - \cos k_y)}{(\varepsilon_{\mathbf{k}} - \mu) + \sqrt{(\varepsilon_{\mathbf{k}} - \mu)^2 + \left[\Delta(\cos k_x - \cos k_y)\right]^2}} e^{-i\mathbf{k}\cdot(\mathbf{r}_{i\uparrow} - \mathbf{r}_{j\downarrow})} \tag{2.15}$$

where the sum is over all the allowed points in the first Brillouin zone. Clearly, $\varphi(\mathbf{k})$ is singular for points with $k_x = k_y$ and $\varepsilon_{\mathbf{k}} \leq \mu$. These singularities in $\varphi(\mathbf{k})$ can be avoided by choosing special boundary conditions or lattice geometries. Some possible choices in this regard for a two dimensional lattice are - (1) a periodic-antiperiodic (PA) boundary condition along the two directions[135, 139], (2) a tilted lattice with periodic boundary condition[124, 142] (PBC) along both directions, and (3) a rectangular lattice whose dimensions are mutually co-prime with PBC along both directions. For a bilayered lattice, any of the above conditions can be applied to the individual layers. Here we take periodic boundary condition along planar *x*-

and antiperiodic boundary condition along planar y-direction, i.e.

$$\left.\begin{aligned} e^{ik_x(x+L_x)} &= e^{ik_x x} \\ e^{ik_y(y+L_y)} &= -e^{ik_y y} \end{aligned}\right\} \tag{2.16}$$

Eq. (2.16) determines the allowed values of k_x and k_y. The k_z values are taken to be 0 and π. The allowed points in the first Brillouin zone in a fixed k_z plane for a $8 \times 8 \times 2$ lattice are shown in Fig. 2.1.

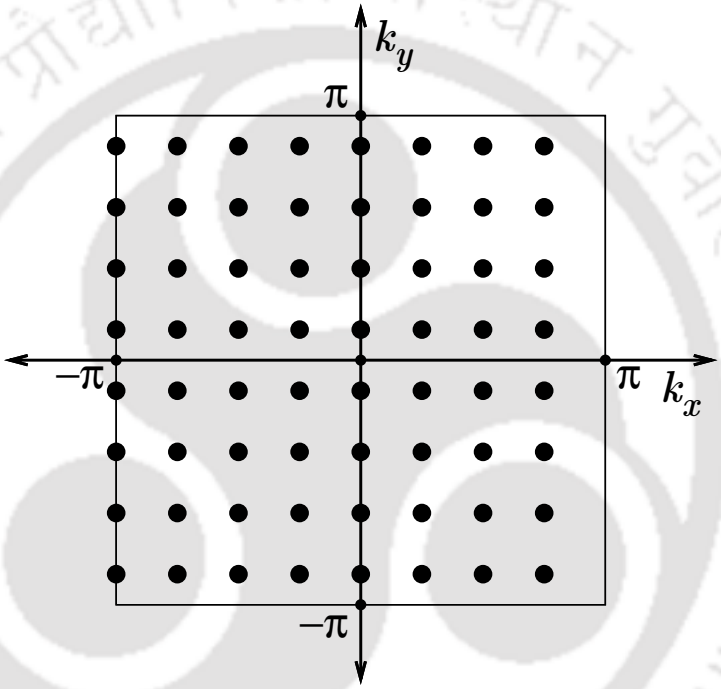

FIGURE 2.1: Allowed momentum values in the first Brillouin zone in a fixed k_z plane for a $8 \times 8 \times 2$ lattice with periodic (antiperiodic) boundary condition along x (y) direction.

2.3.3 Calculation of the expectation values

Expectation value of a physical quantity represented by $\hat{A}$ is given by

$$\langle \hat{A} \rangle = \frac{\langle \Psi_{var} | \hat{A} | \Psi_{var} \rangle}{\langle \Psi_{var} | \Psi_{var} \rangle} \tag{2.17}$$

We can write it as

$$\langle \hat{A} \rangle = \sum_R P(R) \frac{\langle \Psi_{var} | \hat{A} | R \rangle}{C^*(R)} \tag{2.18}$$

where

$$P(R) = \frac{|C(R)|^2}{\sum_{R'} |C(R')|^2} \tag{2.19}$$

From Eq. (2.18), $\langle \hat{A} \rangle$ may be considered as a weighted sum of $A_R = \langle \Psi_{var} | \hat{A} | R \rangle / C^*(R)$ over R with $P(R)$ as the weights. Numerically, evaluation of the sum in the equation is usually not possible as the dimension of the Hilbert space is very large. However in general, owing to the nature of $P(R)$, only a fraction of the total number of configurations contribute to the sum significantly. In the Monte Carlo technique[172], the exact sum is approaximated by a sum consisting of terms only a few percent of the total number of configurations, as follows. We generate a large number of configurations, $|R_1\rangle, |R_2\rangle, \ldots, |R_M\rangle$ from probability distribution $P(R)$ (see §2.3.4). Then the sum in Eq. (2.18) is approaximated by

$$\langle \hat{A} \rangle \approx \langle \hat{A} \rangle_M = \frac{1}{M} \sum_{i=1}^{M} A_{R_i} \tag{2.20}$$

Theoretically, $\langle \hat{A} \rangle_M$ converges to $\langle \hat{A} \rangle$ in the limit $M \to \infty$. However in practice, a value of M which is only a small fraction of the dimension of the Hilbert space is enough to get an estimate $\langle \hat{A} \rangle_M$ fairly close to the exact value $\langle \hat{A} \rangle$.

2.3.4 The Markov chain Monte Carlo method

The theory of Markov chain Monte Carlo method (MCMC) has been described in detail elsewhere[172, 173, 174, 175]. Here, we mention the essential ideas and results without proofs. Consider a sequence of random variables, X_t (t is referred to as time) taking values from a given state space $\{a_1, a_2, \ldots, a_n\}$. This sequence is called a Markov chain if the transition probabilities from X_t to X_{t+1} depend solely on X_t. That is,

$$\Pr\left(X_{t+1} = a_j \,|\, X_t = a_i, \ldots, X_0 = a_s\right) = \Pr\left(X_{t+1} = a_j \,|\, X_t = a_i\right) \tag{2.21}$$

The term in the left hand side of the above equation is the conditional probability that X_{t+1} has value a_j, given that X_t has values a_i and so on. Let $W(i \to j)$ be the transition probability,

defined as

$$W(i \to j) = \Pr\left(X_{t+1} = a_j \,|\, X_t = a_i\right). \tag{2.22}$$

A Markov chain is called homogeneous if W is independent of t.

Let $\rho_t(a_i)$ be the probability that the chain is in state a_i at time t, i.e.

$$\rho_t(a_i) = \Pr\left(X_t = a_i\right) \tag{2.23}$$

Clearly, the initial probability, $\rho_0(a_j)$ must be specified. During the Markov process, $\rho_t(a_j)$ evolves with t. Now, clearly

$$\begin{aligned} \rho_{t+1}(a_j) &= \sum_i \Pr\left(X_{t+1} = a_j \,|\, X_t = a_i\right) \Pr\left(X_t = a_i\right) \\ &= \sum_i W(i \to j)\rho_t(a_i) \end{aligned} \tag{2.24}$$

Eq. (2.24) is known as the Master equation (also as Chapman-Kolmogorov equation). The n-step transition probability is defined as,

$$W^{(n)}(i \to j) = \Pr\left(X_{t+n} = a_j \,|\, X_t = a_i\right) \tag{2.25}$$

Then,

$$\rho_t(a_j) = \sum_i W^{(t)}(i \to j)\rho_0(a_i) \tag{2.26}$$

Now, a Markov chain is said to be irreducible or ergodic if, there exists an integer n such that

$$W^{(n)}(i \to j) > 0 \quad \forall\, i, j \tag{2.27}$$

That is, each state is reachable from any other state in finite time. In addition, a Markov chain is said to be aperiodic if none of the eigenvalues of the matrix $\mathbf{W}$ is -1.

One of the main results on Markov chains is that if a Markov chain is ergodic and aperiodic, ρ_t evolves to a stationary distribution defined as,

$$\bar{\rho}(a_j) = \sum_i W(i \to j)\bar{\rho}(a_i) \tag{2.28}$$

However, usually the converse question is asked. Will a Markov chain with given **W**, reach a desired probability distribution, $\bar{\rho}$? It is easy to see that if the detailed balance (reversibility) condition,

$$\bar{\rho}(a_i)W(i \to j) = \bar{\rho}(a_j)W(j \to i) \tag{2.29}$$

holds for all i and j, then $\bar{\rho}$ is a stationary distribution of the Markov chain. Another result is that if a Markov chain satisfies Eq. (2.29) and is ergodic, then irrespective of the initial probability distribution, ρ_0, it reaches $\bar{\rho}$ for large t.

Metropolis Algorithm: Suppose that we wish to draw samples a_i with a distribution $\bar{\rho}(a_i)$ from the state space. Metropolis gave an algorithm that generates a sequence of draws from this distribution. It is as follows:

1. Start with any initial state a_0 with $\rho(a_0) > 0$.

2. From the current state a_i, generate a trial state a' by using an appropriate Monte Carlo move from a_i. Let $q(a', a_i)$ be the probability of generating a trial state a' from the current state a_i. The only restriction on the Monte Carlo moves in the Metropolis Algorithm is that it is symmetric, i.e. $q(a', a_i) = q(a_i, a')$.

3. Given the trial state a', calculate the ratio,

$$\alpha = \frac{\bar{\rho}(a')}{\bar{\rho}(a_i)} \tag{2.30}$$

4. If the move increases the weight, $\bar{\rho}$ (i.e. $\alpha > 1$), accept the trial state a' as the new state, a_{i+1} in the Markov chain. If the move decreases the weight ($\alpha < 1$), then accept a' with probability α. If rejected, consider a_i as the new state, a_{i+1}. Return to step 2.

The Metropolis sampling can be summarized as first computing

$$\alpha = \min\left\{1, \frac{\overline{\rho}(a')}{\overline{\rho}(a_i)}\right\}. \tag{2.31}$$

and then accepting a trial state with probability α. The corresponding transition probability which satisfies Eq. (2.29) is given by

$$W(a_i \to a') = \alpha \times q(a', a_i). \tag{2.32}$$

The above algorithm generates a Markov chain (a_0, a_1, ..., a_i, ...). Following a sufficient warm up period, it is guaranteed that the chain approaches its stationary distribution $\overline{\rho}(a_i)$.

2.3.5 VMC simulation

The adaptations of MCMC to VMC simulation have been described extensively in literature[116, 132, 135]. The procedure to construct a Markov chain is described above. In this case, we draw samples R from the state space formed by various possible configuration of the electrons. The desired stationary probability distribution is $P(R)$ given by Eq. (2.19). The Monte Carlo moves consists of hopping a spin to a vacant site and exchanging two antiparallel spins. The choice of the spins or vacant site are made randomly.

After each accepted move, the current state of the system needs to be updated, that is, we need to calculate the determinantal coefficient $C(R)$ for the new configuration. Actually the quantity that we need to calculate is the ratio,

$$r = \frac{C(R')}{C(R)} \tag{2.33}$$

between a new and old coefficients for calculation of the transition probability as well as the expectation values. As given in Eq. (2.14), the coefficients are expressed as a determinant, $C(R) = \det|B|$ where B is a $P \times P$ matrix of the form,

$$B = \begin{bmatrix} \varphi(\mathbf{r}_{i_1\uparrow} - \mathbf{r}_{j_1\downarrow}) & \cdots & \varphi(\mathbf{r}_{i_1\uparrow} - \mathbf{r}_{j_P\downarrow}) \\ \vdots & & \vdots \\ \varphi(\mathbf{r}_{i_P\uparrow} - \mathbf{r}_{j_1\downarrow}) & \cdots & \varphi(\mathbf{r}_{i_P\uparrow} - \mathbf{r}_{j_P\downarrow}) \end{bmatrix} \tag{2.34}$$

P is the number of up or down electrons and $2P = N \leq N_s$. Calculating $C(R)$ directly for a new configuration from the above equation is a $O(P^3)$ process and hence computationally very expensive. This can be minimized by using the inverse update method of Ceperley[132]. In this scheme, the inverse of B is also calculated and maintained which enables us to calculate the ratio, r easily without the need of calculating a new $C(R)$ afresh. The updating of the inverse of B is $O(P^2)$ process which is much less expensive. To describe the procedure, let us define matrix D to be the transpose inverse of B,

$$D = \left[B^T\right]^{-1} \tag{2.35}$$

We also define a $N_s \times N_s$ matrix, Φ as

$$\Phi = \begin{bmatrix} \varphi(\mathbf{r}_{1\uparrow} - \mathbf{r}_{1\downarrow}) & \cdots & \varphi(\mathbf{r}_{1\uparrow} - \mathbf{r}_{N_s\downarrow}) \\ \vdots & & \vdots \\ \varphi(\mathbf{r}_{N_s\uparrow} - \mathbf{r}_{1\downarrow}) & \cdots & \varphi(\mathbf{r}_{N_s\uparrow} - \mathbf{r}_{N_s\downarrow}) \end{bmatrix} \tag{2.36}$$

Now let us examine how the coefficient matrix B changes after each hopping move. There can be two types hopping move corresponding to selecting (a) an up spin or (b) a down spin.

(a) Let us consider the p-th up spin hopping to the s-th vacant site. In that case, the p-th row of the B matrix of Eq. (2.34) corresponding to the current configuration will change according to the new position of the spin. The new position vector of the spin is $\mathbf{r}_s$, so the p-th row will be replaced by new row whose elements are,

$$\Phi_{sj_q}, \quad q = 1, 2, \ldots, P \tag{2.37}$$

where $\mathbf{r}_{j_q\downarrow}$ represent the position of the down spin electrons in the configuration. Now the ratio between the new and old coefficients can be shown to be

$$r = \frac{\det|B^{new}|}{\det|B^{old}|} = \sum_{q=1}^{P} \left[D^{old}\right]_{pq} \Phi_{sj_q} \tag{2.38}$$

The inverse matrix for the new configuration can be calculated by updating the old inverse matrix as follows

$$[D^{new}]_{kl} = \left[D^{old}\right]_{kl}/r \quad \text{for } k = p,\ l = 1, 2, \ldots, P \tag{2.39}$$

$$[D^{new}]_{kl} = \left[D^{old}\right]_{kl} - \left[D^{old}\right]_{pl} \sum_{n=1}^{P} \frac{\left[D^{old}\right]_{kn} \Phi_{s j_n}}{r} \tag{2.40}$$

$$\text{for } k \neq p,\ l = 1, 2, \ldots, P$$

(b) For the case of hopping the q-th down spin to the s-the vacant site, the q-th column of the B matrix is replaced by a new column whose elements are given by,

$$\Phi_{i_p s}, \quad p = 1, 2, \ldots, P \tag{2.41}$$

The ratio between the new and old determinant is

$$r = \frac{\det|B^{new}|}{\det|B^{old}|} = \sum_{p=1}^{P} \left[D^{old}\right]_{pq} \Phi_{i_p s} \tag{2.42}$$

And the inverse matrix is updated as

$$[D^{new}]_{kl} = \left[D^{old}\right]_{kl}/r \quad \text{for } l = q,\ k = 1, 2, \ldots, P \tag{2.43}$$

$$[D^{new}]_{kl} = \left[D^{old}\right]_{kl} - \left[D^{old}\right]_{kq} \sum_{n=1}^{P} \frac{\left[D^{old}\right]_{nl} \Phi_{i_n s}}{r} \tag{2.44}$$

$$\text{for } l \neq q,\ k = 1, 2, \ldots, P$$

For exchange of two antiparallel spins, the above scheme can be implemented in a two step process to calculate the ratio of determinants. First we move the up electron to the position of the down electron making the site doubly occupied. The ratio of the two determinants is calculated using the formalism of (a). Next the down electron is moved to the previous position of the up electron and the second ratio of determinants is calculated using the formalism of (b). The product of these two ratios give the final ratio between the coefficient of the new configuration after exchange to that before exchange. The inverse matrix is also updated through the intermediate step.

The process of generating new states in the Markov chain is continued by visiting different lattice sites and hopping or exchanging spins. This process of visiting the lattice sites and making the Monte Carlo moves is called sweep. Generally in one Monte Carlo sweep (MCS), N_s (number of lattice sites) moves are made which consists of hopping an electron to an empty site and exchanging two antiparallel spins. The percentage of hopping and exchange moves should be tuned so as to maximize the overall acceptance ratio of moves. Before measurement is started, we need to warm up the system to a the desired stationary distribution. Usually a few thousand MCS is enough for warming up for a typical 200 sites lattice. Once the warm up is over, measurement process can be started on the subsequent states. However successive states generated by a Monte Carlo move are highly correlated. In order to get a true statistical estimate of a quantity, it is desirable to have samples which are independent of each other. Therefore measurement are performed on the states in the sequence separated by a certain interval. Here we consider an interval of 5 MCS, which is equivalent to $5 \times N_s$ Monte Carlo moves. Average values are calculated using Eq. (2.20) by considering samples from the total generated by about 10^5 to 10^7 MCS. However, the results of individual measurements for all the samples are not averaged together. The total number of sweeps is divided into G (= 10−20) groups and the measurement results for each groups are collected separately in *bins*. We then calculate the bin averages separately, using

$$A_i = \frac{1}{M_i} \sum_{j=1}^{M_i} \frac{\langle \Psi_{var} | \hat{A} | R_j \rangle}{C(R_j)} \tag{2.45}$$

where M_i is number of samples collected in the i-th bin. These averages $\{A_1, A_2, \ldots, A_G\}$ can be regarded as true random variables and the final expectation value is calculated using,

$$\langle \hat{A} \rangle = \frac{1}{G} \sum_{i=1}^{G} A_i \tag{2.46}$$

The statistical error in $\langle \hat{A} \rangle$ is estimated as

$$\sigma_A = \sqrt{\frac{\sum_i^G \left(\langle \hat{A} \rangle - A_i \right)^2}{G}} \tag{2.47}$$

2.3.6 Verification of the VMC code

We developed the complete code for the VMC in C programming language. We performed rigorous checks of the codes by comparing our results with some well known results. By switching off one layer in our code, we calculated energies for the two dimensional *t*-*J* model at various hole doping. For the two dimensional model there are plenty of results available in the literature. Here, we show the comparison of our results with those by Yokoyama *et al*[138]

We consider the *d*-wave SC state in a 10×10 lattice and take the exchange coupling in the planar *t*-*J* Hamiltonian to be $J/t = 0.5$. We found the optimal values of the variational parameter of the wavefunction to be $\tilde{\Delta} = 0.57, 0.72, 0.56, 0.38$ and 0.25 for electron densities, $n = 1.00, 0.96, 0.88, 0.80$ and 0.72, respectively. These values match closely with those given in Ref. [138]. Next we show comparison of energies corresponding to different terms in the *t*-*J* Hamiltonian. We define E_t, E_J and E_d as

$$E_t = \left\langle -t \sum_{\langle i,j\rangle\sigma} \left(c^{\dagger}_{i\sigma} c_{j\sigma} + h.c. \right) \right\rangle \tag{2.48}$$

$$E_J = \left\langle J \sum_{\langle i,j\rangle} \mathbf{S}_i . \mathbf{S}_j \right\rangle \tag{2.49}$$

$$E_d = \left\langle J \sum_{\langle i,j\rangle} \left(-\frac{n_i n_j}{4} \right) \right\rangle \tag{2.50}$$

Values of these three energy components (in *per site* and in units of *t*) obtained from our calculations and its comparison with the corresponding values in Ref. [138] are shown in Fig. 2.2. The excellent agreements between the two results as seen in the figures indicate the correctness of our codes

For bilayer lattice, we could not directly compare our calculations with others as we are not aware of any published VMC results on bilayer *t*-*J* model. However we made a check of the codes for bilayers in another way as follows. For a small lattice of size $4 \times 4 \times 2$, we calculated the energy of the *d*-wave SC state at half-filling by exactly carrying out the sum in Eq. (2.18) by considering all possible the states of the system. The determinantal coefficients were calculated directly without going through any updating procedure. The energy thus obtained with all parameter values set to unity, is -1.6518 per site. The energy obtained for

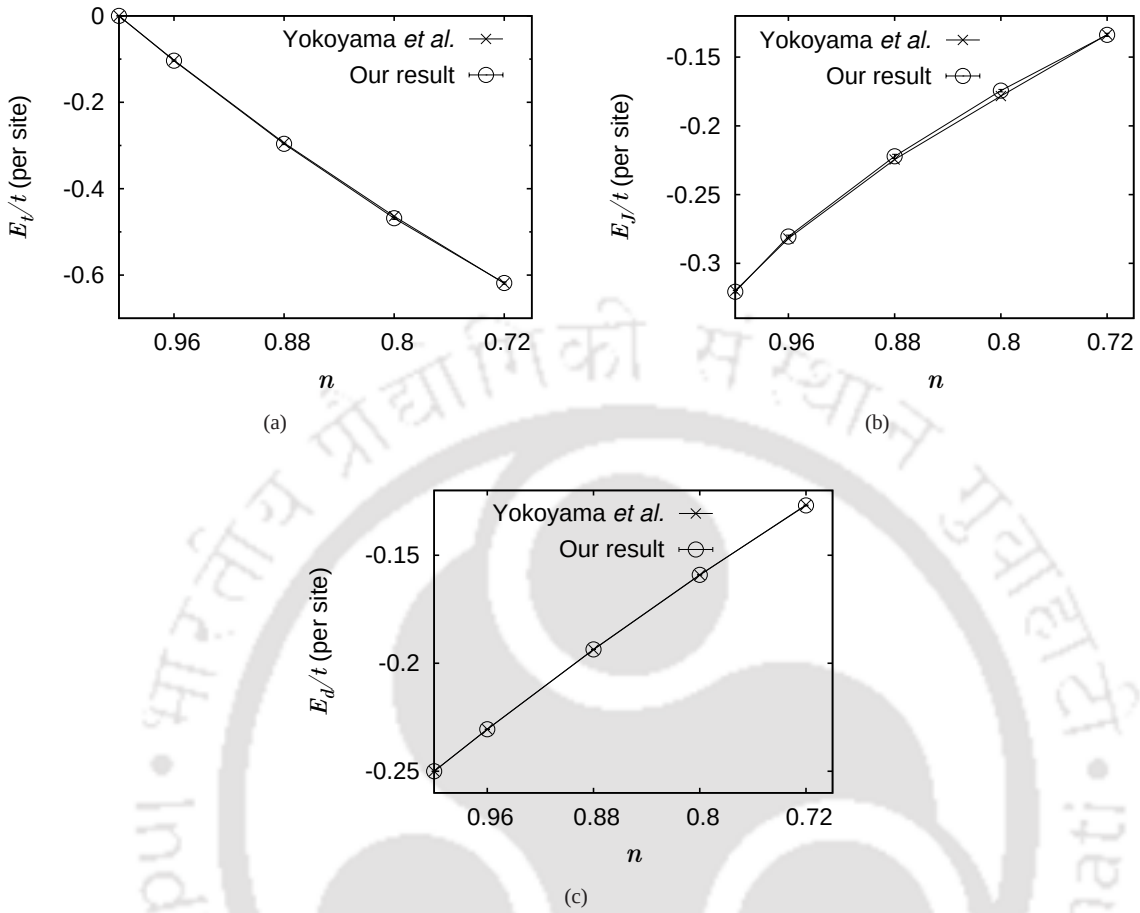

FIGURE 2.2: Comparison of our VMC results with those by Yokoyama *et al*[138]. Energies (a) E_t (b) E_J and (c) E_d (per site in units of t) for the d-wave superconducting state as a function of electron density, n. Lattice size is 10×10 and $J = 0.50t$.

the same case, by using the Monte Carlo procedure is -1.6504, showing good agreement between the two.

2.4 A quantum Monte Carlo (QMC) study of the Hubbard model doped with nonmagnetic impurities

Substitution of nonmagnetic impurities in the cuprate compounds has been used as an effective probe to study the nature of electronic correlations in the materials, specially in the underdoped region. The Cu^{2+} ions in the CuO_2 planes of the cuprate superconductors have a

net magnetic moment, whereas ions like Zn^{2+} having almost same ionic radius as Cu^{2+}, is nonmagnetic with a filled 3*d* shell. Thus local defects are created on the Cu sites by substituting them with Zn ions. One direct consequence of nonmagnetic impurity substitution in half-filled cuprates is the weakening of antiferromagnetism due to loss of magnetic moments and subsequent suppression of Néel temperature, T_N as observed in La_2CuO_4[37, 176, 177]. Interestingly in weakly hole doped $La_{2-x}Sr_xCuO_4$, T_N was found to increase when doped with a small amount of Zn impurity before decreasing eventually for large impurity concentration[178]. The experimental data indicates that the increase in T_N occurs due to reduction of hole mobility caused by the presence of Zn impurities. In the superconducting state, nonmagnetic impurities are found to suppress the transition temperature, T_c[179].

Effects of nonmagnetic impurities have also been studied on ladder compounds which are of special interest because of the existence of a spin gap. NMR studies of the the two-leg ladder compound $SrCu_2O_3$ (spin gap, $\Delta \sim 680K$) have revealed that the gap gets rapidly suppressed when doped with Zn impurity[180]. Other experiments involving magnetic susceptibility measurement have shown that dc magnetic susceptibility versus temperature curves for $Sr(Cu_{1-x}Zn_x)_2O_3$ shows a cusp-like anomaly at a particular temperature before showing a Curie-Weiss behavior at lower temperature[181].

To elucidate these features and also to investigate the interplay between holes and impurities, we model the physical system by a strong coupling Hubbard model with an additional potential term representing the presence of the impurities. The resulting Hamiltonian in a square lattice and in a two-leg ladder is studied using the finite temperature quantum Monte Carlo (FTQMC) method. A number of relevant macroscopic quantities are calculated as a function of impurity concentration at different levels of hole doping.

2.4.1 The Quantum Monte Carlo method

The Quantum Monte Carlo (QMC) method is a powerful numerical technique for studying the finite temperature properties of a strongly correlated electron system[182]. The advantage of QMC is that it gives fairly exact result of a finite size system and results are unbiased by choice of any variational wavefunction as in VMC. However, the negative sign problem limits its applicability away from half-filling and at very low temperature[183].

We developed the numerical code for the FTQMC method for studying the Hubbard model during the current project. The technical problem of stabilizing computations at low temperatures is adequately taken care of by using the method of matrix decomposition introduced by White *et al*[182]. The details of the method are described in appendix A. Here we show the verification of our codes by comparing a few results for the two dimensional Hubbard model. The Hubbard model is given by,

$$\mathcal{H} = -t \sum_{\langle ij\rangle,\sigma} \left(c^{\dagger}_{i\sigma} c_{j\sigma} + h.c. \right) + U \sum_{i} n_{i\uparrow} n_{j\downarrow} - \mu \sum_{i\sigma} n_{i\sigma} \tag{2.51}$$

where $c^{\dagger}_{i\sigma}$ ($c_{i\sigma}$) is the creation (annihilation) operator for an electron at site i with spin σ, and $n_{i\sigma} = c^{\dagger}_{i\sigma} c_{i\sigma}$. The sum $\langle ij\rangle$ is over all pairs of nearest neighbor sites. t is the hopping integral, U is on site Coulomb repulsion, μ is the chemical potential controlling the band filling.

For testing our QMC codes, we calculate the following three quantities for the Hamiltonian and compare with the corresponding results shown in Ref. [182]. These quantities are (a) squared local moment, $c(0,0) = \langle (n_{i\uparrow} - n_{i\downarrow})^2 \rangle$ (b) site double occupancy $\langle n_{i\uparrow} n_{i\downarrow} \rangle$ and (c) spin-spin correlation function, $c(i,j) = \left\langle (n_{i\uparrow} - n_{i\downarrow})(n_{j\uparrow} - n_{j\downarrow}) \right\rangle$. Results for these quantities calculated using our QMC codes are shown in the Fig. 2.3. Comparing the results with that obtained for the same quantities by White *et al.*[182], we find very good quantitative agreement between the two, thus indicating correctness of our codes.

2.4.2 Effects of nonmagnetic impurities

We study the effects of nonmagnetic impurity doping on the magnetic properties of Hubbard model at and slightly away from half-filling. We also examine the mobility of holes in the vicinity of an impurity to determine whether the impurities effect the hole mobility. The impurities are modeled by adding an extra potential term to the usual Hubbard model. Thus we consider a Hamiltonian given by,

$$\mathcal{H} = -t \sum_{\langle ij\rangle,\sigma} \left(c^{\dagger}_{i\sigma} c_{j\sigma} + h.c. \right) + U \sum_{i} n_{i\uparrow} n_{j\downarrow} - \mu \sum_{i\sigma} n_{i\sigma} + \sum_{i'} V_0 n_{i'} \tag{2.52}$$

where the first three terms represent the usual Hubbard model defined in Eq. (2.51). The summation index i' in the last term denote an impurity site. The presence of an impurity can be

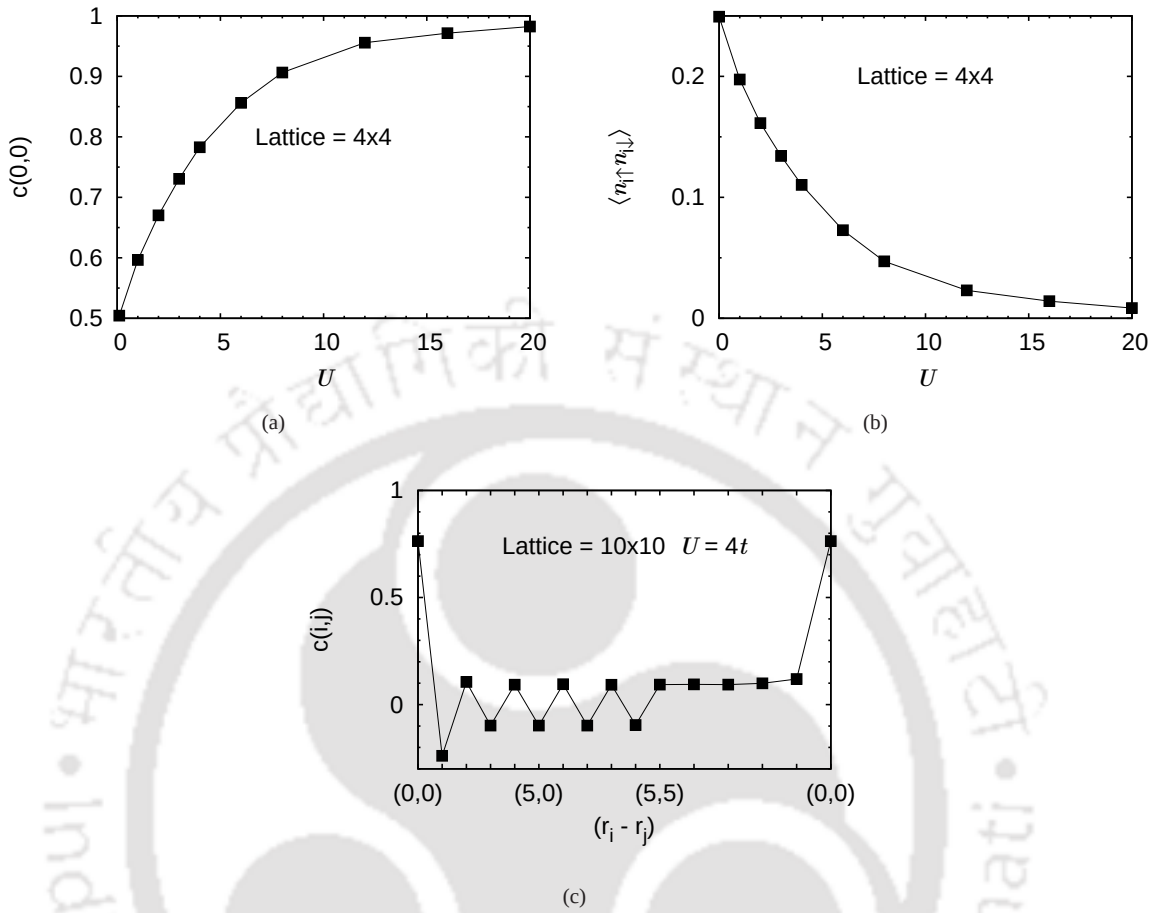

FIGURE 2.3: Results for a few quantities for the two dimensional Hubbard model obtained by our QMC. The results are in good quantitative agreement with those in Ref. [182]. The data shown are for inverse temperature $\beta = 16/t$ and band filling, $\langle n \rangle = 1.0$. (a) The squared local moment, $c(0,0)$ as a function U. (b) Double occupancy, $\langle n_{i\uparrow} n_{i\downarrow} \rangle$ as a function of U. (c) Spin-spin correlation, $c(i, j)$ as a function of distance. The paired numbers in parenthesis along the horizontal axis are the coordinates of a few chosen lattice points in a 10×10 lattice.

simulated by taking V_0 to be either a large (as compared U) negative or large positive[184]. For large negative value of V_0, the corresponding sites are always doubly occupied making them magnetically inert. On the other hand for large positive V_0, the sites will be rarely occupied by electrons resulting in null magnetic moments in it. We take V_0 to be large negative, that is $V_0 = -20t$. We have checked that occupancies of the impurity sites are very close to 2 for this potential. In case of multiple impurities, the impurity sites are chosen randomly.

2.4.3 Two dimensional lattice

We consider a lattice of size 10×10. The Hubbard interaction potential is taken to be $U = 4t$. The simulations are performed at an inverse temperature of $\beta = 1/kT = 6/t$. We calculate the local magnetic moment, $m_i = \langle (n_{i\uparrow} - n_{i\downarrow})^2 \rangle^{1/2}$, spin-spin correlation function, $c(i, j) = \left\langle (n_{i\uparrow} - n_{i\downarrow})(n_{j\uparrow} - n_{j\downarrow}) \right\rangle$ and spin structure factor, $S(\mathbf{q}) = (1/N_s) \sum_{ij} e^{-i\mathbf{q}.(\mathbf{r}_i - \mathbf{r}_j)} c(i, j)$ (N_s is the number of lattice sites) for the impurity doped lattice at two values of band filling, e.g. $\langle n \rangle = 1.0$ and $\langle n \rangle = 0.93$. We observe interesting effects of impurity, such as, enhancement of magnetic correlations around an impurity, destruction of AF long range order by finite concentration of impurities etc. The results are described in the following.

At half-filling, with one nonmagnetic impurity the value of the local magnetic moment m_i is found to be 0, 0.882(3) and 0.867(2) at the impurity site, sites neighbouring the impurity and sites far away from the impurity respectively, indicating a slight enhancement of the value near the impurity site. Qualitatively same behaviour was seen for band filling $\langle n \rangle = 0.93$. Fig. 2.4 shows the nearest neighbour (nn) spin correlations around, and along $\hat{x}$ and diagonal directions with reference to the impurity site, respectively. The nn spin correlations are found to increase

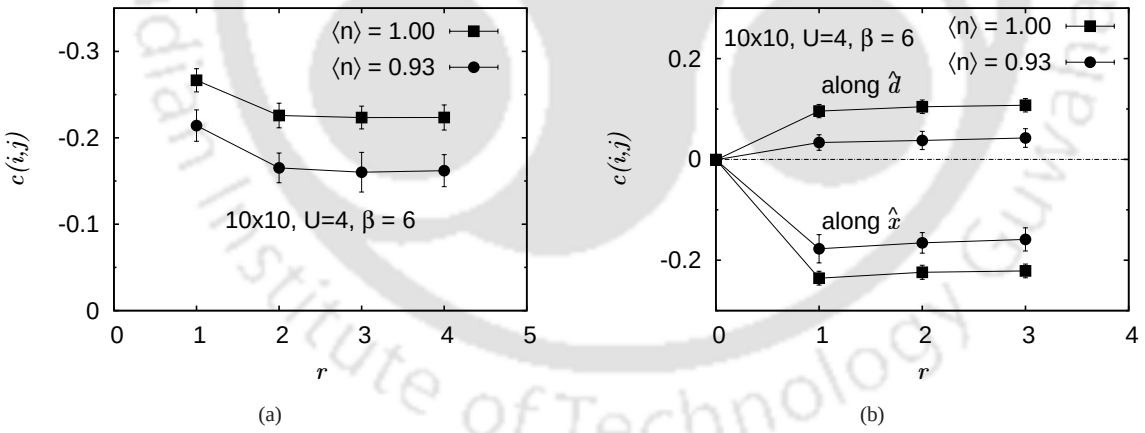

FIGURE 2.4: Spin-spin correlation, $c(i, j)$ for two nearest neighbour (nn) sites i, j as a function of distance, $\mathbf{r}_i$ of the site i from the impurity. (a) $\mathbf{r}_i$ is along $\hat{x}$ and the bonds i-j are transverse to $\mathbf{r}_i$. (b) $\mathbf{r}_i$ is along $\hat{x}$ and diagonal direction ($\hat{d}$), and the bonds i-j lie along $\mathbf{r}_i$.

in the vicinity of the impurity site which is in agreement with previous studies[185]. The enhancement decreases as one moves away from the impurity. Qualitatively similar behavior is seen for the hole doped case. The origin of this effect can be understood on the basis of the fact that configurations with lower energy are favoured more. The four neighbours of the

impurity experience constrained hopping because of the impurity. To compensate for this, a spin at these sites would prefer to have its other three nearest neighbour sites not to be occupied by the same species of spin, so that it can minimize energy by hopping to those sites more frequently. This increases the spin correlations near the impurity. On the other hand the increase in local moment at sites near the impurity is because of reduced probability of double occupancy at those sites which happens because the sites are surrounded by only three 'active' sites. Fig. 2.5 shows the spin structure factor $S(\mathbf{q})$ calculated for wave vector $\mathbf{q} = (\pi, \pi)$, with different number of randomly positioned impurities. The initial rapid decrease

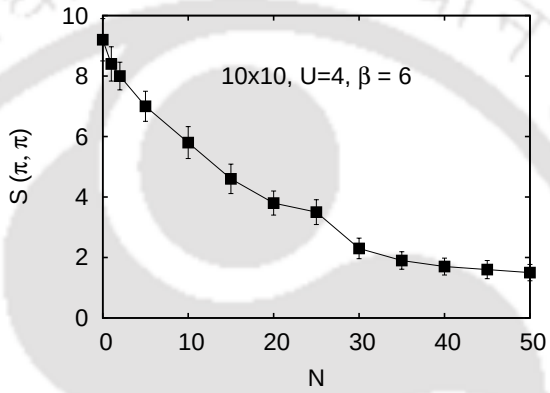

FIGURE 2.5: Spin structure factor, $S(\pi, \pi)$ as a function of number, N of impurities. Parameter values are shown in figure.

of $S(\pi, \pi)$ with increasing number of impurities is due to the suppression of AFLRO. The order seems to get destroyed completely at around 35% of impurity concentration in accordance with experiments[177]. The slow decrease beyond this concentration is due to the impurity induced dilution of the lattice.

2.4.4 Two-leg ladder

Next we examine the effects of nonmagnetic impurity doping in a two-leg Hubbard ladder of size 20×2. The interaction potential is taken to be $U = 6t$. The impurity site configurations are chosen in such a way that the ladder remains always connected.

We calculate the magnetic susceptibility defined as,

$$\chi(\mathbf{q}) = \frac{1}{N} \sum_{ij} e^{-i\mathbf{q}(\mathbf{r}_i - \mathbf{r}_j)} \int_0^\beta d\tau \left\langle (n_{i\uparrow}(\tau) - n_{i\downarrow}(\tau))(n_{j\uparrow}(0) - n_{j\downarrow}(0)) \right\rangle \tag{2.53}$$

as a function of temperature, T for the pure and doped ladder. Here β is the inverse temperature and τ is the imaginary time. The results for the uniform magnetic susceptibility, $\chi_0(T)$ $(= \chi(q = 0, T))$ where $T = 1/\beta$, are shown in Fig. 2.6. For the pure case, suscepti-

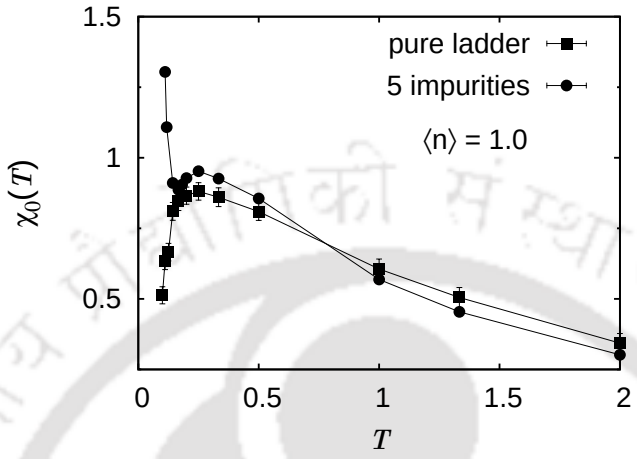

FIGURE 2.6: Uniform susceptibility, $\chi(q = 0)$ versus temperature, T for the pure and doped ladder at half filling.

bility increases initially with decreasing temperature, reaches a maximum and then decreases sharply at further lower temperatures. However when the ladder is doped with nonmagnetic impurities, $\chi_0(T)$ shows a cusp-like feature followed by a dramatic increase at lower temperatures. Similar behavior of magnetic susceptibility was observed experimentally in Ref. [181]. The results for the pure case can be understood as follows. At higher temperatures spins are almost *free* due to weak magnetic correlations and hence susceptibility shows the expected Curie-Weiss like increase with decreasing temperature. As the temperature is further lowered, spin fluctuations are reduced and spins start to form singlet pairs which results in the decrease of susceptibility below a certain critical temperature. When the ladder is doped with nonmagnetic impurities, free local moments are induced around impurity sites[186] giving rise to the rapid increase in susceptibility at low temperatures. The occurrence of the cusp has the following explanation. There exists two characteristic temperature scales in the system. One, below which susceptibility starts to decrease, marks the onset of spin singlet formation. The other, slightly lower, signals the onset of localization of induced free magnetic moment as indicated by the sharp increase in susceptibility. The observed cusp is a result of these two phenomena occurring at two different temperatures.

To examine the enhancement of magnetic correlations by nonmagnetic impurities, we calculate the spin spin correlation function, $c(i, j) = \langle (n_{i\uparrow} - n_{i\downarrow})(n_{j\uparrow} - n_{j\downarrow}) \rangle$ at various temperatures

at and away from half filling. Fig. 2.7 shows the results for spin correlations along a leg for the pure ladder and the ladder doped with one nonmagnetic impurity, at half filling. It is observed

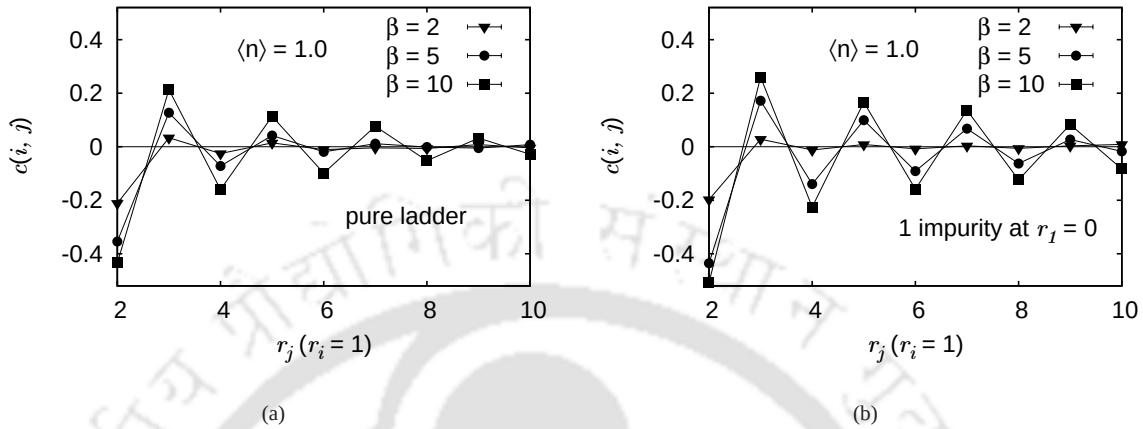

FIGURE 2.7: Spin spin correlations, $c(i, j)$ between sites r_i (=1) and r_j (=2,...,10) belonging to the same leg for (a) the pure ladder and (b) the ladder doped with one nonmagnetic impurity placed at site $r_i = 0$. The sites in the leg are numbered as $0, 1, 2, \ldots$ respectively. Band filling, $\langle n \rangle = 1.0$. The values of β (in units of t) are shown in the figures.

that in the presence of the impurity, the antiferromagnetic (AF) correlations are enhanced, a feature also noted in studies on Heisenberg ladders[185, 187]. This effect is more prominent at lower temperatures. For $\beta = 2$ shown in figure, no noticeable impurity effect is observed. For the two other values of β, *viz*. 5 and 10, it is interesting to note that in addition to the nearest neighbor, the long distance spin correlations are also enhanced by the impurity. We carried out similar calculations for a 10×10 square lattice and found that the enhancement at larger distances for the ladder is greater than that in the square lattice. Away from half filling, at electron densities $\langle n \rangle = 0.95$ and 0.90, the effect of an impurity on spin correlations for $\beta < 5$ is found to be weaker. Simulation at still lower temperatures is prevented by the negative sign problem. Further, we calculate the spin structure factor $S(\boldsymbol{q}) = 1/N \sum_{ij} e^{i\boldsymbol{q}.(\boldsymbol{r}_i - \boldsymbol{r}_j)} c(i, j)$ at $\boldsymbol{q} = (\pi, \pi)$ for various band fillings with different number of impurities, to study the effect of finite impurity concentration on the magnetic order. The results are shown in Fig. 2.8. At half filling, $S(\pi, \pi)$ increases for small impurity concentration indicating strengthening of AF order in the ladder, which is in agreement with experimental results[181]. For larger impurity concentrations, long range spin correlations are heavily destroyed by the presence of impurities and thus $S(\pi, \pi)$ decreases. Away from half filling, the enhancement of spin correlations by impurity is anyway small for the range of temperatures considered here. Hence $S(\pi, \pi)$

decreases slowly with increasing impurity concentration due to the dilution of magnetic sites.

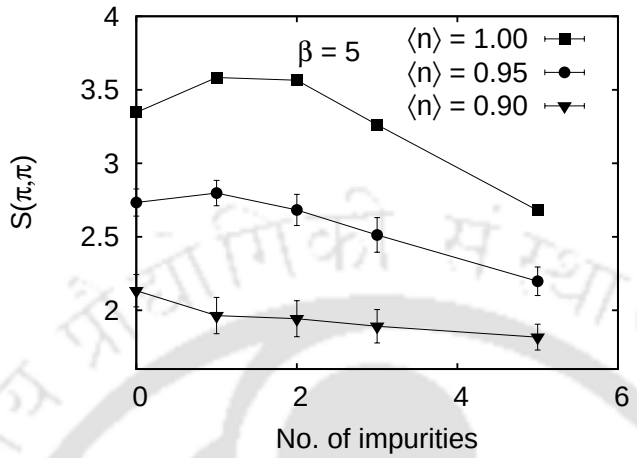

FIGURE 2.8: $S(\pi,\pi)$ versus number of nonmagnetic impurities at various band fillings.

We also examine the effects of nonmagnetic impurities on the spin wave excitation modes in the ladder. We calculate the spin wave velocity, v_{sw} as a function of impurity concentration in the following way. The magnon dispersion, $\omega(q)$ was calculated for the two dimensional Hubbard model using an approximate relation given by, $\omega(q) = 2S(q)/\chi(q)$[188]. We use the same relation to calculate magnon dispersion for the ladder. Then the spin wave velocity for long wavelength ($q \to 0$) spin wave modes is obtained using $v_{sw}(q) = \omega(q)/q$. In Fig. 2.9, we show the results for $v_{sw}(q)$ for a few small values of q calculated for different number of impurities for $\beta = 8$. The plot clearly suggests that spin wave velocity gets suppressed due to softening of the spin wave excitations.

Finally, to verify whether nonmagnetic impurity affects hole mobility as suggested by experiments[178], we calculate the kinetic energy, $\langle c^{\dagger}_{i\sigma} c_{j\sigma}\rangle$ of the electrons around an impurity site for the doped ladder and compare it with that for the pure ladder, slightly away from half filling. The results of our calculation do not show any evidence of any effect of the impurities on the mobility of the electrons neighboring it. To quote some numbers, the value of $\langle c^{\dagger}_{i\sigma} c_{j\sigma}\rangle$ for two nearest neighbor sites i, j for the pure ladder is 0.165 for $\beta = 5$, $\langle n\rangle = 0.95$. For the doped case also, the value for any pair around an impurity site is found to be the same within statistical error bars.

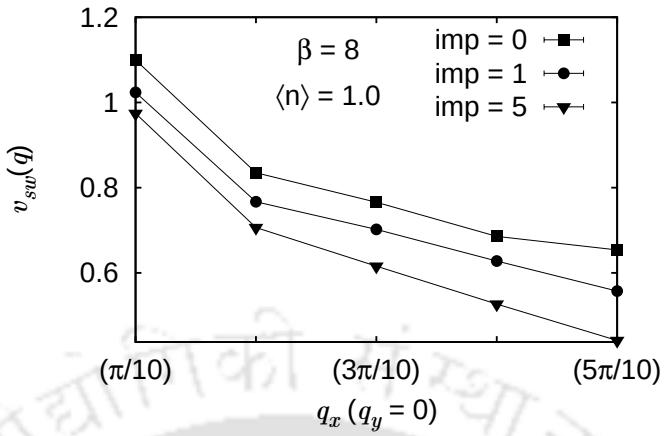

FIGURE 2.9: Long wavelength spin wave velocity, $v_{sw}(q)$ for the pure and impurity doped ladder. $\beta = 8$ and $\langle n \rangle = 1.0$.

2.5 Summary

In this chapter, we have introduced our model for bilayer superconductors and mentioned previous results obtained for the model. We have described the variational Monte Carlo method in details. The numerical code for the method developed by us was tested for correctness by comparing our results with other published results.

We have also reported the results of a brief QMC study on nonmagnetic impurity doping in the Hubbard model. We developed the numerical code for the finite temperature QMC method and tested for its correctness. Using QMC, we studied the effects of nonmagnetic impurity doping on the Hubbard model for square lattice and for a two-leg ladder at and away from half-filling. We observed interesting effects of nonmagnetic impurities on the magnetic properties. Antiferromagnetic correlations are enhanced around an impurity. However AF long range order (AFLRO) is destroyed by a finite concentration of impurities. For ladder, the uniform magnetic susceptibility as a function of temperature for the doped system shows a sharp increase at lower temperatures, a feature not seen in pure ladders. In addition the spin wave modes softens which is signaled by the spin wave velocity going down for the doped systems. Further, we found no evidence of any effect of impurity on the mobility of electrons neighboring impurity sites.

Chapter 3

Superconducting and magnetic properties of t-J bilayer

3.1 Introduction

Superconductivity in the two dimensional (2D) t-J model has been studied in considerable details in the past using variational Monte Carlo (VMC). Significant contributions include early works by Gros[124, 125], Yokoyama *et al*[138], Sorella *et al*[128] and others. In these studies, the superconducting as well as several other competing phases based for the 2D t-J model were described in terms of Gutzwiller projected variational wavefunctions. The results obtained in these studies have established a ground state phase diagram for the model. It is found that the half-filled phase is AF insulating, the hole doped phase for a wide range of doping is superconducting and the heavily overdoped phase is a normal metallic. A number of symmetries were considered for the superconducting gap function, however the most favourable state in the physical range of t, J parameter values was found to have the $d_{x^2-y^2}$-wave (d-wave) symmetry in agreement with experiments. The Gutzwiller projected BCS wavefunction with d-wave symmetry has been quite successful in explaining many of the observed properties of high-T_c superconductors as demonstrated more recently by Paramekanti *et al*[141, 142]. However such studies have been lacking in bilayers and it provides a motivation for our current study.

The interplay of antiferromagnetism and superconductivity in high-T_c cuprates has been of utmost interest owing to their proximity in the phase diagram. A basic question has been whether the AF interactions between the copper spins in the CuO_2 layers play a role in the pairing mechanism of high-T_c superconductors[85, 189, 190]. In the phenomenological $SO(5)$ theory, antiferromagnetism and superconductivity are assumed to have a common microscopic origin and are treated on an equal footing[95, 191]. A natural extrapolation of finding the connection between AF and SC is the issue of their coexistence. Experimentally, inelastic neutron scattering studies on underdoped YBCO suggest that magnetic ordering, though may be of short range, exists in the SC state[192, 193, 194]. A Cu-NMR study on a five-layered Hg-based compound finds that AF and SC ordering exist at the same time in alternating copper oxide layers of the material[195]. In contrast, the two dimensional Hubbard and t-J models are found to support a coexisting scenario where the magnetic ordering is rather robust with AF long range order (AFLRO) surviving in the superconducting state upto a large value of hole doping[128, 139, 140, 196].

Here we examine these issues, e.g. the pairing symmetry of the superconducting state and coexistence of AF and SC in bilayers using VMC by taking the Hamiltonian parameter values within a range as suggested by theory and experiments. First we consider a variational wavefunction describing a purely superconducting state. Three possible pairing symmetries for the SC state are considered. Our variational calculations indicate that the favourable pairing symmetry of the SC state is d-wave. We study the dependence of the optimal gap parameter for the d-wave state on hole doping, lattice size and the interplanar parameters. Next we examine the coexistence of antiferromagnetic and superconducting correlations by considering a variational wavefunction which describe both the orders simultaneously. We find that the underdoped regime supports a coexisting phase, beyond which the (d-wave) superconducting state becomes stable. The superconducting and magnetic properties in the coexisting phase are compared with those in the pure SC state. The results show that both the SC and AF correlations are enhanced in coexisting phase as compared to those in the pure SC state. A larger interplanar hopping, is found to reduce planar correlations at optimal doping, while an opposite behaviour, that is stabilization of the superconducting state is observed in the overdoped regime, with the interplanar exchange all the while playing a dormant role.

3.2 Model parameters and other numerical details

The bilayer *t*-*J* Hamiltonian is described in §2.2. For referring to different terms in the Hamiltonian later, we write it as

$$\begin{aligned}\mathcal{H} &= \mathcal{P}_G\Bigg[-t\sum_{\langle i,j\rangle\sigma}\left(c^{\dagger}_{i\sigma}c_{j\sigma}+h.c.\right)+J\sum_{\langle i,j\rangle}\left(\boldsymbol{S}_i.\boldsymbol{S}_j-\frac{1}{4}n_in_j\right)\\ &\quad -t_{\perp}\sum_{\langle\langle i,k\rangle\rangle\sigma}\left(c^{\dagger}_{i\sigma}c_{k\sigma}+h.c.\right)+J_{\perp}\sum_{\langle\langle i,k\rangle\rangle}\left(\boldsymbol{S}_i.\boldsymbol{S}_k-\frac{1}{4}n_in_k\right)\Bigg]\mathcal{P}_G\\ &= \mathcal{H}^t_{\parallel}+\mathcal{H}^J_{\parallel}+\mathcal{H}^t_{\perp}+\mathcal{H}^J_{\perp}\end{aligned} \tag{3.1}$$

The planar parameter values of the *t*-*J* model are estimated from ab initio calculations to be $t \sim 0.35 - 0.44$ eV and $J \sim 0.13$ eV[86, 150] giving a J/t value of $\sim 0.30 - 0.37$. Such a value of the planar exchange coupling parameter (~ 0.13 eV) is confirmed by experiments measuring magnon excitation spectra in both single layer $La_{2-x}Sr_xCuO_4$[39, 87] and bilayer $YBa_2Cu_3O_{6+x}$[197, 198, 199]. However it is not possible to measure the hopping parameter directly in experiment. In this work we fix the planar hopping and exchange parameters at constant values and take $J = 0.35t$ throughout.

To study the effect of interplanar interaction on the properties, we have varied $t_\perp$ and $J_\perp$ over a small range compatible with experiments and ab-initio calculations. The interplanar exchange, $J_\perp$ is estimated to be of $\sim$ 0.01 eV by Millis *et al*[200] and also in the above references mentioned for bilayer. The band structure calculations of Andersen *et al*[150] give $t_\perp = 0.05$ eV and $J_\perp = 0.02$ eV. A recent ab-initio calculation by Muñoz *et al*[201] concludes that for different multilayer cuprates, $t_\perp$ varies from $0.091 - 0.121$ eV and $J_\perp$ from $0.004 - 0.014$ eV. Here we have considered $t_\perp = 0.05t, 0.20t$, and $J_\perp = 0.03t, 0.10t$. These values are approaximately in the range as suggested by the above studies.

The method (VMC) used to study the Hamiltonian is described in §2.3. The numerical details of our calculations are calculations are as follows. Simulation was performed mainly on a lattice of size $8 \times 8 \times 2$. We have examined the finite size effects by calculating a few quantities for different lattice sizes. The Monte Carlo (MC) moves consists of moving a randomly chosen electron to a random vacant site and exchanging two randomly chosen antiparallel spins. The system is warmed up for about 500 Monte Carlo sweeps (MCS), where

one MCS consists of N_s (number of lattice sites) random moves. Out of the N_s moves within one MCS, the percentages of hopping and exchange moves are chosen so as to maximize the acceptance ratio of the Monte Carlo moves. After a move is accepted, the configurations are updated using the inverse update method[132]. For calculation of the expectation values, we have taken comparatively larger sample sizes in order to get a good accuracy. The size of the Hilbert space increases rapidly upto about 30% hole concentration and then falls off. One therefore has to increase the sample size accordingly in order to get similar accuracy in calculated quantities at various doping levels. For energy calculations, we have taken about 10^5 sweeps at half-filling which was increased upto about 10^7 sweeps away from half-filling, making measurements at an interval of 5 MCS. For calculation of other properties, the number of sweeps was 10^6 at half-filling and larger away for non-zero hole doping. The energy and parameter values mentioned in all the subsequent discussions are in units of t. In addition, the energy values are quoted as energy per site.

3.3 The superconducting state

The variational wavefunction that we have considered for describing the superconducting state, is the Gutzwiller projected BCS wavefunction, which in fixed N (number of electrons) formulation (§2.3.1) can be written as,

$$|\Psi_{var}\rangle = \mathcal{P}_G \left(\sum_{\mathbf{k}} \varphi(\mathbf{k}) c^{\dagger}_{\mathbf{k}\uparrow} c^{\dagger}_{-\mathbf{k}\downarrow} \right)^{N/2} |0\rangle \tag{3.2}$$

where $\mathcal{P}_G = \prod_i (1 - n_{i\uparrow} n_{i\downarrow})$ is the Gutzwiller projector which projects out the states with no doubly occupied site. The summation index '$\mathbf{k}$' runs over all points in the first Brillouin zone. The pairing amplitude, $\varphi_{\mathbf{k}}$ is given by

$$\varphi(\mathbf{k}) = \frac{\Delta_{\mathbf{k}}}{(\varepsilon_{\mathbf{k}} - \mu) + \sqrt{(\varepsilon_{\mathbf{k}} - \mu)^2 + \Delta^2_{\mathbf{k}}}} \tag{3.3}$$

where $\Delta_{\mathbf{k}}$ is the superconducting gap function, $\varepsilon_{\mathbf{k}} = -2t\left(\cos k_x + \cos k_y\right) - 2t_\perp \cos k_z$ with k_z being 0 or π, is the dispersion relation for bilayers and μ is the chemical potential. The wavefunction of Eq. (3.2) reduces to the the normal state when $\Delta_{\mathbf{k}} \to 0$ uniformly for all $\mathbf{k}$.

We get,

$$\lim_{\Delta_{\mathbf{k}}\to 0} \varphi(\mathbf{k}) = 0 \quad \text{for } \varepsilon(\mathbf{k}) > \mu \tag{3.4}$$

and consequently if μ is equal to μ_0 (chemical potential for the noninteracting case), $|\Psi_{var}\rangle$ becomes the projected Fermi sea upto a normalization constant. That is

$$|\Psi_{var}\rangle_{\Delta_{\mathbf{k}}\to 0} = \mathcal{P}_G \prod_{k\le k_F} c^{\dagger}_{\mathbf{k}\uparrow} c^{\dagger}_{\mathbf{k}\downarrow} |0\rangle \tag{3.5}$$

3.3.1 The gap function

The momentum dependence of the superconducting gap, $\Delta_{\mathbf{k}}$ has been one of the major issues in the high-T_c superconductors. The general conclusion from angle resolved photoemission spectroscopy (ARPES) and tunneling experiments is that $\Delta_{\mathbf{k}}$ has d-wave symmetry ($\Delta(\mathbf{k}) = \Delta(\cos k_x - \cos k_y)$)[21, 46]. It is maximum near the antinodal $(0,\pi)$ or $(\pi,0)$ points and is zero along the nodal (π,π) direction. However, there exists a number of experimental evidences which suggest that the gap function is more complex than a simple d-wave. An early report in this regard is the ARPES result for the energy gap in $Bi_2Sr_2CaCu_2O_{8+x}$ (Bi2212) by Ding *et al.*[202] They find that the gap does not vanish along (π,π) direction, instead the node is split into two and lies near the (π,π) line on its either side. Similar result was obtained by Vobornik *et al.*[203] who found an energy gap of ~ 9 meV along the Brillouin zone diagonal for heavily overdoped Bi2212. More recently, analyzing high-resolution spectroscopic data on Bi2212, Zhao[204] concludes that the diagonal superconducting gap in the compound is of ~ 7 meV. These results are in direct contrast to a d-wave scenario of the superconducting gap. Zhao argues that the photoemission and tunneling experiments are surface sensitive and hence may not reveal the true gap characteristics of the bulk materials. In fact, his results support a gap with an extended s-wave symmetry having eight line nodes. However such evidences contradicting the d-wave scenario seem to be coming only from bilayer materials. A very recent ARPES study on high quality single crystal $La_{2-x}Sr_xCuO_4$ (LSCO) shows that the superconducting gap in this material follows the simple d-wave variation with the gap magnitude vanishing along (π,π).

These facts put together, lead one to believe that the situation in bilayered materials might be different and it may be a consequence of interlayer coupling. The possibility of interlayer

pairing and its effect on the overall energy gap structure in bilayers was investigated by Lee *et al*[205] in the framework of the *t*-*J* model. Using the slave-boson mean field theory (SBMFT), they showed that introduction of interlayer hopping and exchange coupling lead to a state having both an interlayer pairing amplitude and a *d*-wave pairing amplitude in a layer. The stable state was found to have a $d \pm s$ symmetry with the gap function being given by $\Delta_{\mathbf{k}} = \Delta_d \pm \Delta_\perp$, where Δ_d has *d*-wave symmetry and $\Delta_\perp$ is constant. The - (+) sign correspond to the bonding (antibonding) band. Such a gap structure explains the observation of Ref. [202] on Bi2212, since the minima of $|\Delta_d \pm \Delta_\perp|$ would be shifted from the (π, π) line. Here we also consider such a gap function (we call the $\pm\Delta$ state as d_z-wave here) for the superconducting state in addition to a pure *d*-wave gap. Our ansatz functions for the superconducting gap are the following,

$$\Delta_{\mathbf{k}} = \begin{cases} \text{(a)} & \Delta_d \left(\cos k_x - \cos k_y\right) \quad (d\text{-wave}) \\ \text{(b)} & \Delta_\parallel \left(\cos k_x - \cos k_y\right) + \Delta_\perp \cos k_z \quad (d + d_z) \\ \text{(c)} & \Delta_\parallel \left(\cos k_x - \cos k_y\right) + \Delta_\perp (1 - \cos k_z) \quad (d - d_z) \end{cases} \tag{3.6}$$

3.3.2 Stable pairing symmetry

As with any variational calculation, we have optimized the wavefunction by calculating the energy,

$$\langle \mathcal{H} \rangle = \frac{\langle \Psi_{var} | \mathcal{H} | \Psi_{var} \rangle}{\langle \Psi_{var} | \Psi_{var} \rangle} \tag{3.7}$$

as a function of the variational parameters and then minimizing it. The stable pairing symmetry of the superconducting state is determined by choosing the lowest energy state among the ones considered. The variational parameters for the *d*-wave state is Δ_d and μ. For the other two states listed above (Eq. (3.6)), the parameters consist of $\Delta_\parallel$, $\Delta_\perp$ and μ. The parameter μ can practically be taken to be the chemical potential for the corresponding noninteracting system, μ_0. This is because the energy improvement obtained by varying μ around μ_0 is found to be negligible, especially for small J, as observed in the two dimensional *t*-*J* model[138]. We found this to be true in bilayers also. This is illustrated in Fig. 3.1 where we plot the variational energy of the *d*-wave state at hole concentration, $x = 0.19$ as a function of Δ_d for various μ. The figure shows that the difference in energy between the lowest minimum (obtained for $\mu - \mu_0 = -0.20$) and the minimum for the noninteracting value of the chemical potential is

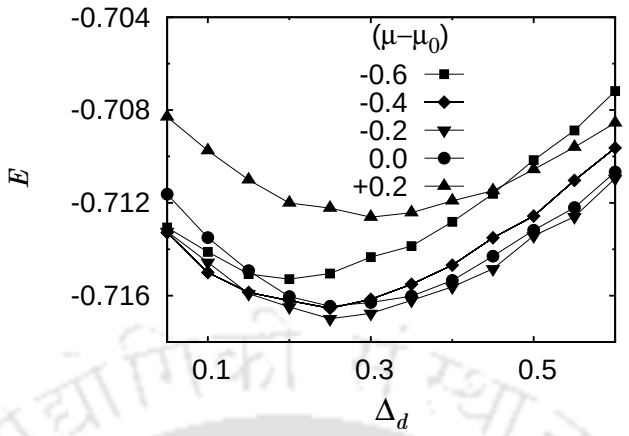

FIGURE 3.1: Variational energy, E for the d-wave SC state plotted as function of Δ_d for different values of μ. The numbers shown in figure are the values of $(\mu - \mu_0)$, where μ_0 $(= -0.37$ in this case) is the noninteracting chemical potential. Hole concentration, $x = 0.19$ and $(t_\perp, J_\perp) = (0.20, 0.10)$. Lattice size is $8 \times 8 \times 2$.

very small. More importantly the variational μ does not seem to shift values of optimal Δ_d which has a direct bearing on the physical properties. Similar feature was observed also for other values of interplanar coupling parameters. Hence we take, $\mu = \mu_0$ in all the calculations.

Optimizing with respect to rest of the variational parameters, we observed the following. The pairing symmetry (c) (Eq. (3.6)) is not favourable for any parameter value or hole doping. The lowest energy of the state is obtained only with $\Delta_\perp = 0$, which reduces it to the d-wave state. As for the $(d + d_z)$ state, it yields lowest energy (with nonzero $\Delta_\perp$) only for one case, e.g. for the smaller $t_\perp$ $(= 0.05)$, larger $J_\perp$ $(= 0.10)$ and at half-filling. For all other parameter values and hole doping, $\Delta_\perp$ raises the energy as compared to that for pure d-wave state. In Fig. 3.2, we plot the variational energy of the $(d + d_z)$ state as a function of $\Delta_\parallel$ and $\Delta_\perp$ for $(t_\perp, J_\perp) = (0.05, 0.10)$ at and slightly away from half-filling. The figure at $x = 0$ shows that the energy of the pure d-wave state $(\Delta_\perp = 0)$ is significantly lowered by the introduction of nonzero $\Delta_\perp$. The lowest energy is obtained at $\tilde{\Delta}_\parallel \sim 0.8$, $\tilde{\Delta}_\perp \sim 0.8$ signaling the stability of the $(d + d_z)$ state at this value of hole doping. On the other hand, the figure at $x = 0.02$ shows that even slightly away from half-filling, the $(d + d_z)$ state lies higher in energy in comparison to the pure d-wave state. Similar behaviour is observed at all hole doping for other values of interplanar parameters. This result is in sharp contrast to the mean-field results of Ref. [205], which finds the $(d + d_z)$ state to be favourable for bilayers for a wide range of hole doping. Thus except for the one case, the d-wave state the yield lowest

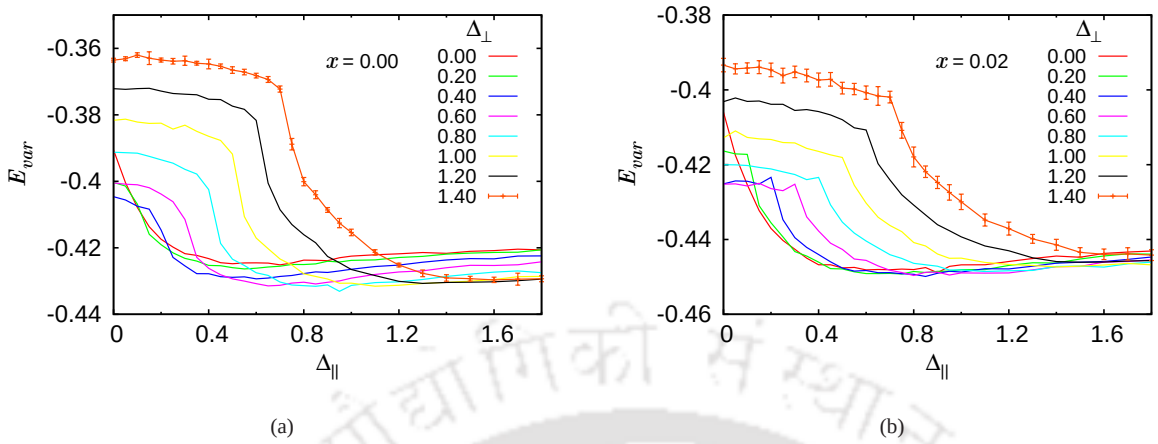

FIGURE 3.2: Variational energy, E_{var} for the $(d + d_z)$ state as function of $\Delta_{||}$ for various values of $\Delta_\perp$ (a) at half-filling and (b) at a hole doping, $x = 0.02$. Error bars are shown only for one curve in each figure for clarity. Interplanar parameters are, $(t_\perp, J_\perp) = (0.05, 0.10)$ and lattice size is $8 \times 8 \times 2$.

energy among the ones considered for a wide range of hole doping. To show the behaviour of the variational energy of the d-wave state, in Fig. 3.3 we plot the energy for the state as a function of its variational parameter, Δ_d for a few different values of hole concentration. The

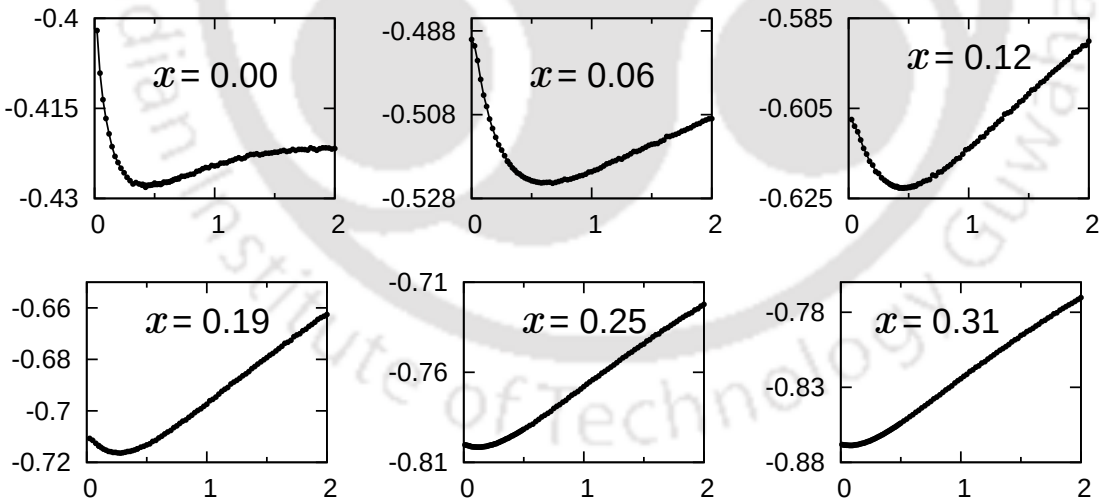

FIGURE 3.3: Variational energy, E_{var} (along the vertical axes) for the d-wave state as function of Δ_d (along the horizontal axes) at various hole concentrations shown in the figures. Interplanar parameters are, $(t_\perp, J_\perp) = (0.05, 0.10)$ and lattice size is $8 \times 8 \times 2$.

variational energy shows a shallow minimum as a function of Δ_d near half-filling. The depth of the minimum increases with doping, becoming maximum around optimal hole concentration

and then decreases again. The position of the minimum shifts gradually to lower Δ_d side with increasing x. The optimal energy of the d-wave state obtained from the such data as above for various values of interplanar parameter are shown in Fig. 3.4 as a function of hole concentration. In order to estimate the finite size effects on the magnitude of the optimal gap

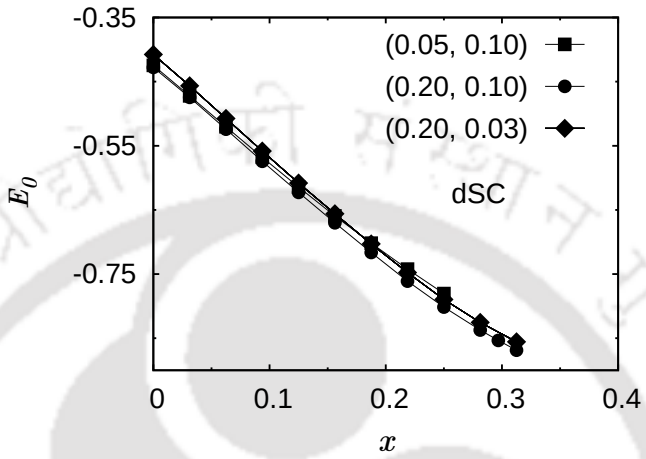

FIGURE 3.4: Optimal energy, E_0 (per site in units of t) for the d-wave state as function of hole concentration, x. The paired number in the parentheses shown in the figure are values of $(t_\perp, J_\perp)$. Lattice size is $8 \times 8 \times 2$.

parameter, $\tilde{\Delta}_d$ (for d-wave state), we optimized the wavefunction for three different lattice sizes, e.g. $6 \times 6 \times 2$, $8 \times 8 \times 2$ and $10 \times 10 \times 2$. This is presumably important as the physical properties of the wavefunction are crucially dependent on $\tilde{\Delta}_d$. However in this case, we found that the finite size effect on $\tilde{\Delta}_d$ is very little which will be evident in the following section.

Thus we conclude that the energy gap for the t-J bilayer for realistic parameter values has d-wave symmetry which has also been found to be the case in single layers. Having decided on the pairing symmetry, we now investigate the properties of the d-wave state in details.

3.3.3 Doping dependence of the superconducting gap

The doping dependence of the superconducting gap parameter, $\tilde{\Delta}_d(x)$ of the d-wave state for different lattice sizes and interplanar parameter values is shown in Fig. 3.5. The main features observed in the figures are as follows. Except near half-filling, the gap $\tilde{\Delta}_d$ decreases monotonically with increasing hole doping, x and vanishes at a critical concentration, x_c which is around 30%. The magnitude of $\tilde{\Delta}_d(x)$ is roughly the same among different lattice sizes,

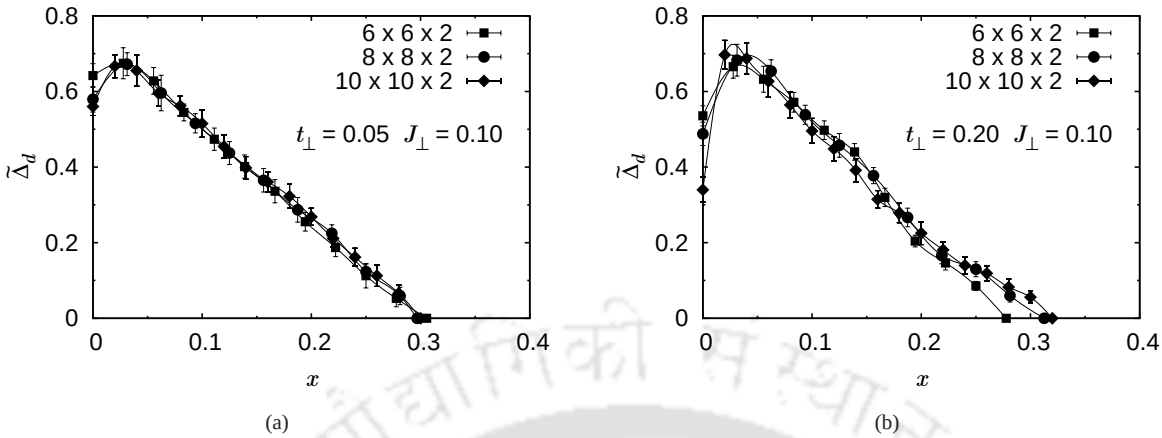

FIGURE 3.5: Doping dependence of the optimal variational parameter, $\tilde{\Delta}_d(x)$ of the d-wave SC state in bilayer for different lattice sizes and interplanar parameters.

except for some small differences in the overdoped region (near x_c) for the larger value of interplanar hopping, $t_\perp$. For this case, $\tilde{\Delta}_d(x)$ shows a increase with increasing lattice size as seen in Fig. 3.5(b). The interplanar exchange coupling, $J_\perp$ has no effect on the $\tilde{\Delta}_d$ and hence figures are shown only for one value of $J_\perp$. For comparison, we also optimized the d-wave superconducting wavefunction for the two dimensional t-J model for parameter values same as those of the planar parameters for the bilayer. The results for $\tilde{\Delta}_d(x)$ is shown in Fig. 3.6. It

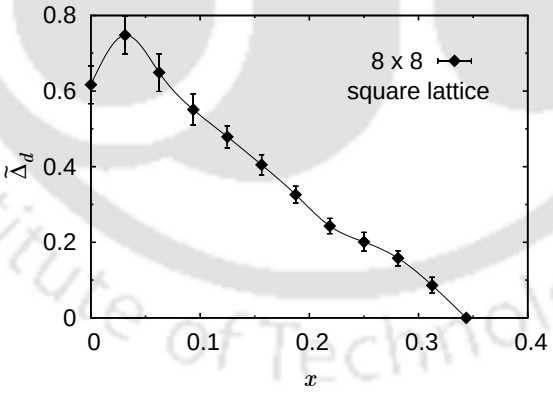

FIGURE 3.6: Optimal gap parameter, $\tilde{\Delta}_d(x)$ of the d-wave state as a function of hole doping for the two dimensional t-J model. Lattice size is 8×8 and J/t (= 0.35) is same as the value of planar exchange coupling parameter taken for the bilayer.

shows that the behaviour of $\tilde{\Delta}_d$ for bilayer and the two dimensional lattice is similar.

Another feature observed in Fig. 3.5 is that $\tilde{\Delta}_d$ increases initially just away from half-filing from its value at $x = 0$, before going down with x. This appear as humps near $x = 0$ in the

$\tilde{\Delta}(x)$ curves as seen in the figure. We find it to be a result of the competition between hopping and exchange energies. To see this, in Fig. 3.7 we plot the exchange and hopping energies, E_J ($= \langle \mathcal{H}_{\parallel}^J + \mathcal{H}_{\perp}^J \rangle$) and E_t ($= \langle \mathcal{H}_{\parallel}^t + \mathcal{H}_{\perp}^t \rangle$) respectively, versus the variational parameter, Δ_d, for a few small values of hole doping corresponding to the lattice size and parameter values shown. At half-filling, the exchange energy and hence the total energy shows a minimum for

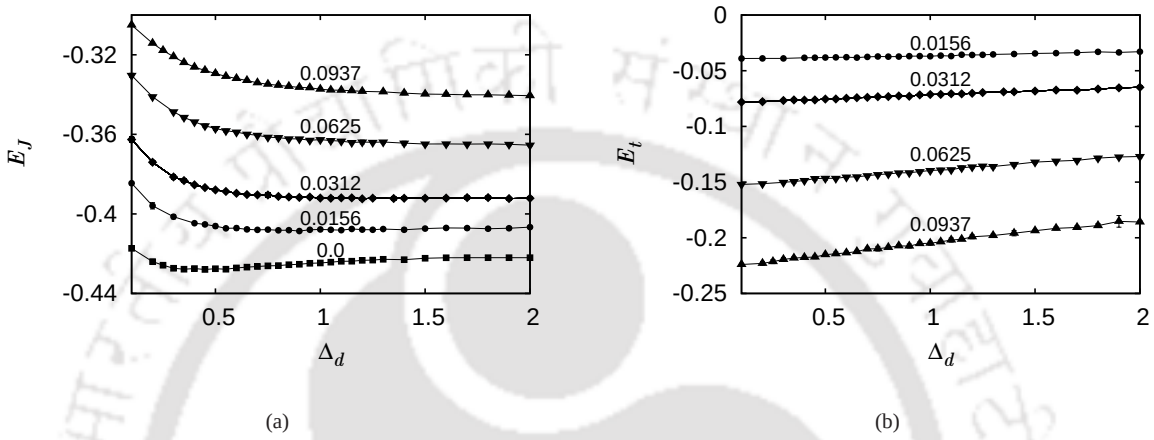

FIGURE 3.7: Variation of exchange energy E_J and hopping energy E_t (per site in units of t) of the d-wave state with variational parameter Δ_d, at different values of hole concentration shown in the figures. The lattice size is $8 \times 8 \times 2$ and $(t_\perp, J_\perp) = (0.20, 0.10)$.

$\Delta_d \sim 0.4$. Away from half-filling, the exchange energy does not really have a minimum. It decreases initially with increasing Δ_d and becomes almost constant afterwards. This tends to shift $\tilde{\Delta}_d$ towards the higher side as the hole concentration is increased. However, as soon as holes are introduced into the lattice the kinetic energy starts playing a role. The hopping energy E_t increases with increasing Δ_d, and at a faster rate at larger hole concentration. At small hole concentration, with initial increase of Δ_d, the energy gain due to decrease in E_J overcompensates for the energy loss due to increase in E_t. Thus $\tilde{\Delta}_d$ increases with increasing x up to a certain value. Beyond this value of x, the kinetic energy dominates the energy spectrum which results in the decrease of $\tilde{\Delta}_d$ with increasing hole concentration.

3.3.4 Magnetic and superconducting correlations

To study the magnetic properties in the d-wave SC state in the bilayer, we calculate the spin-spin correlation function, $\langle S_i^z S_j^z \rangle$ and the corresponding Fourier transform, $S(\mathbf{q})$, called as the

spin structure factor which is defined as,

$$S(\mathbf{q}) = \frac{1}{N}\sum_{ij} e^{i\mathbf{q}\cdot(\mathbf{r}_i-\mathbf{r}_j)}\langle S_i^z S_j^z\rangle \tag{3.8}$$

The results at various hole dopings and its comparison with the corresponding results for a square lattice are shown in Fig. 3.8. Fig. 3.8(a) shows the spin-spin correlation, $\langle S_i^z S_j^z\rangle$ as a

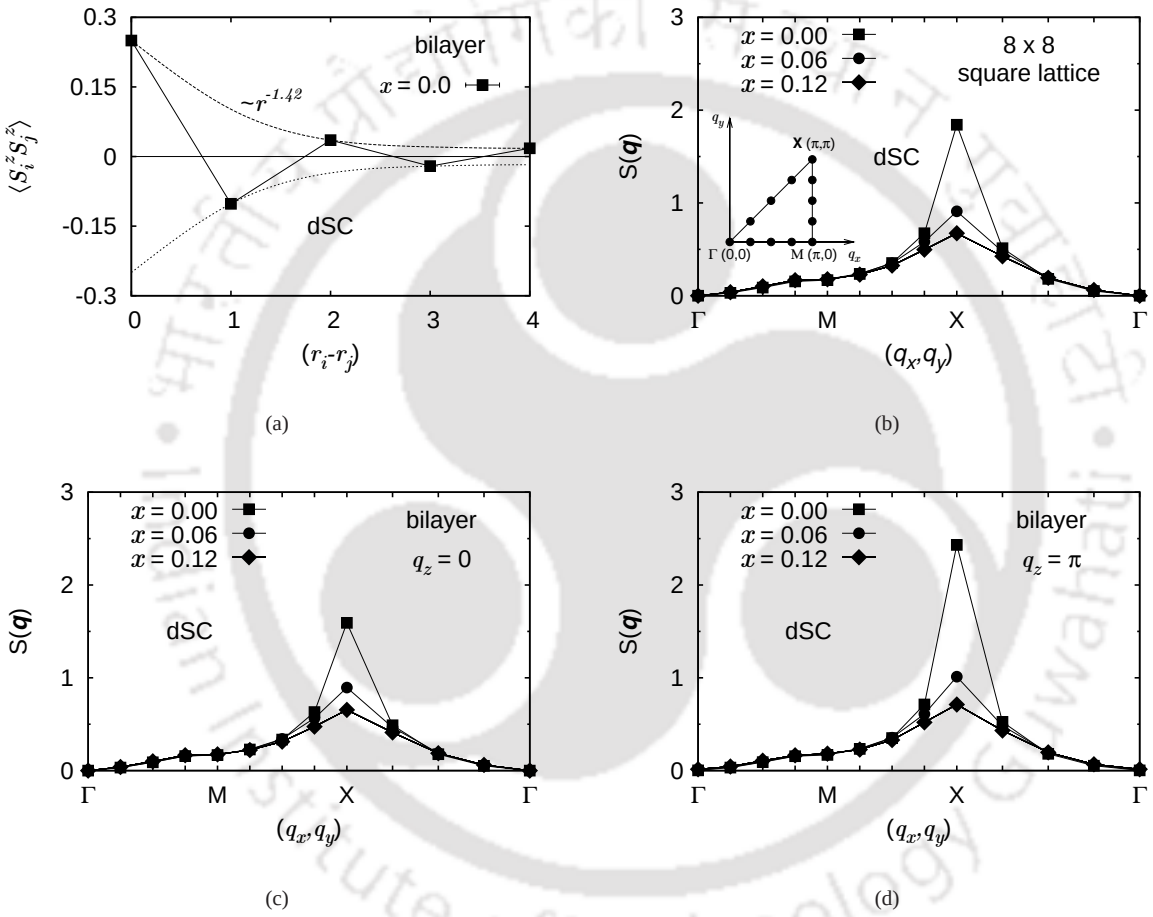

FIGURE 3.8: Magnetic correlations in the *d*-wave state (dSC) in bilayer and in a two dimensional lattice at various hole dopings. (a) Spin-spin correlation, $\langle S_i^z S_j^z\rangle$ in a plane as a function of distance along $\hat{x}$-direction at half-filling. The two envelopes represent the decay of correlation with distance which goes as $\sim r^{-1.42}$. (b) Spin structure factor, $S(\mathbf{q})$ as a function of $\mathbf{q}$ along a path (ΓMX triangle) shown in the figure, for a square lattice of size 8×8. (c) $S(\mathbf{q})$ as a function of planar $\mathbf{q}$ along the ΓMX triangle for $q_z = 0$. (d) Same as (c) but for $q_z = 0$. The bilayer lattice size is $8\times 8\times 2$ and $(t_\perp, J_\perp) = (0.20, 0.10)$. Planar J (= 0.35) is same in both the bilayer and the square lattice.

function of distance, $(\mathbf{r}_i - \mathbf{r}_j)$ along the planar $\hat{x}$-direction at half-filling. The correlations are

suggestive of the existence of AF order in the system. However the strength of correlations decays with distance as shown by the curves enveloping the magnitudes, indicating the absence of AF long range order (AFLRO). The decay obeys a power law behaviour and it was found to be given by $\langle S_i^z S_j^z \rangle \sim r^{-1.42}$. The value of the exponent, 1.42 is not too different from the value of 1.5 obtained for the *d*-wave state in a 2D Hubbard model[142]. The interplanar correlations, i.e. $\langle S_i^z S_j^z \rangle$ with i, j belonging to different layers, are found to be even smaller. In fact, it is negligible in comparison to planar correlations. For instance, the strength of the nearest neighbour spin correlation for two corresponding sites in different planes is approximately 10% of that for two sites in the same plane. The spin structure factor, $S(\mathbf{q})$ as a function of (q_x, q_y) along the ΓMX triangle for $q_z = 0$ and π are shown in Fig. 3.8(d) and Fig. 3.8(c) at different hole dopings. The peak at (π, π, π) indicates the AF correlations in the lattice, however it is not as sharp as is expected for a true AFLRO. Thus the *d*-wave state underestimates the magnetic correlations in the cuprates near half-filling as noted in earlier studies[142]. Also the magnitudes of $S(q_x, q_y, 0)$ and $S(q_x, q_y, \pi)$ are comparable suggesting again that the interplanar correlations are very weak. Away from half-filling the peaks in $S(\mathbf{q})$ decreases rapidly signaling the destruction of AF order. Qualitatively similar behaviour is observed for a square lattice whose results is also shown in the figure. The results for other values of the interplanar parameters are similar and hence not shown. It may be mentioned that the quantity that is usually measured in neutron scattering experiments is the dynamic structure factor, $S(\mathbf{q}, \omega)$. Away from half-filling, the experiments observe peaks in scattering intensity at certain incommensurate wave vectors at lower frequencies (see Ref. [171] and references therein for a recent progress on the subject). In bilayer compounds, such as YBCO, the incommensurate peaks merge into a single commensurate resonance peak at a higher frequency.

Next we examine the superconducting correlations in the *d*-wave SC state. The SC pair-pair correlation function is defined as,

$$F_{\alpha,\beta}(\mathbf{r} - \mathbf{r}') = \left\langle B^\dagger_{\mathbf{r}\alpha} B_{\mathbf{r}'\beta} \right\rangle \tag{3.9}$$

where B's are pair operators, given by $B_{\mathbf{r}'\beta} \equiv \frac{1}{2}(c_{\mathbf{r}'\uparrow} c_{\mathbf{r}'+\beta\downarrow} - c_{\mathbf{r}'\downarrow} c_{\mathbf{r}'+\beta\uparrow})$. $B_{\mathbf{r}'\beta}$ annihilates a singlet pair on bond $(\mathbf{r}', \mathbf{r}' + \boldsymbol{\beta})$ while $B^\dagger_{\mathbf{r}\alpha}$ creates one on $(\mathbf{r}, \mathbf{r} + \alpha)$. $\boldsymbol{\alpha}$ and $\boldsymbol{\beta}$ are unit vectors connecting to nearest neighbours in the $\hat{x}$, $\hat{y}$ (planar) and $\hat{z}$ (across the plane) directions. We have computed $F_{\alpha,\beta}$ as a function of distance $|\mathbf{r} - \mathbf{r}'|$ and obtained the superconducting order parameter, Φ as follows. The order parameter for the *d*-wave state is defined as[142] $F_{\alpha,\beta}(\mathbf{r} -$

$\mathbf{r}'$) $\rightarrow \pm{\Phi_d}^2$ for large $|\mathbf{r}-\mathbf{r}'|$, where the + (−) sign correspond to $\boldsymbol{\alpha}$ || (⊥) to $\boldsymbol{\beta}$ (with both $\boldsymbol{\alpha}$ and $\boldsymbol{\beta}$ lying in a single layer). Thus the quantity, Φ_d correspond to the planar SC correlations in the lattice. The interplanar correlations are obtained by taking both $\boldsymbol{\alpha}$, $\boldsymbol{\beta}$ to be along z-direction. The results for planar superconducting correlations for one particular case is shown in Fig. 3.9. We see that the planar correlations are strong and does not show any appreciable

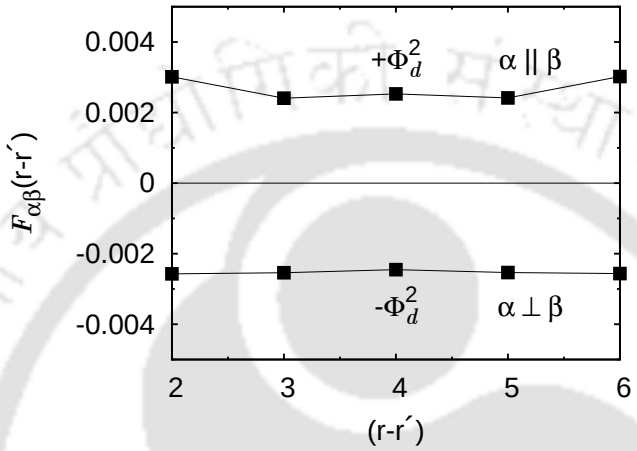

FIGURE 3.9: SC pair-pair correlation, $F_{\alpha,\beta}(\mathbf{r}-\mathbf{r}')$ for the d-wave state as a function of distance $(\mathbf{r}-\mathbf{r}')$ between two planar pairs along $\hat{x}$-direction. The points of maximum distance which are used to determine the order parameter, Φ_d are indicated in the figure. Hole concentration, $x = 0.19$. Lattice size is $8\times8\times2$ and $(t_\perp, J_\perp) = (0.20, 0.10)$.

decay with distance. The change in sign for $\boldsymbol{\alpha}$ || (⊥) β is due to the d-wave symmetry of the superconducting state. The interplanar correlations corresponding to both $\boldsymbol{\alpha}$, $\boldsymbol{\beta}$ along z-direction, which is not shown in the figure, are found to be negligibly small. The result appears as no surprise in view of the form of the gap function for the d-wave state.

The SC order parameter, Φ_d obtained from the pair-pair correlation function as described above is calculated at various values of hole doping and interplanar parameters. The results are shown in Fig. 3.10. The figure shows that Φ_d is zero at half-filling, increases with increasing x in the underdoped region and becomes maximum at an optimal doping of around 20% hole concentration. Beyond this level, Φ_d decreases with x and vanishes at a critical hole doping, x_c that depends on the interplanar hopping integral, $t_\perp$. The variation of Φ_d with x resembles the variation of T_c with hole concentration in the phase diagrams of high-T_c superconductors. Also it is in contrast to behaviour of the gap parameter, $\tilde{\Delta}_d$ which increases with decreasing x and becomes maximum near half-filling. The behaviour of Φ_d is understood as follows[142]. At underdoping, particle number fluctuations at individual sites are severely restricted by

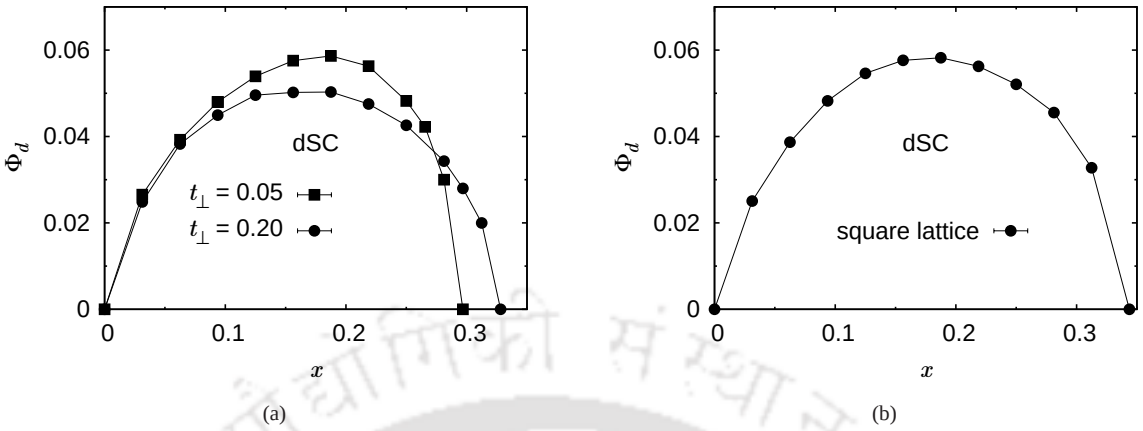

FIGURE 3.10: Superconducting order parameter, Φ_d of the d-wave SC state as a function of hole doping, x. (a) For a bilayer of size $8 \times 8 \times 2$ and interplanar parameter values as shown in the figure. (b) For a square lattice of size 8×8 with planar parameter values same as that for the bilayer.

the projection operator. Consequently, there is a large fluctuations in its conjugate variable, the phase of the order parameter. This quantum fluctuations destroy the order parameter increasingly as we approach half-filling. In the overdoped region, Φ_d decreases with x because more and more Cooper pairs are disrupted by the holes which tend to get delocalized in order to lower the kinetic energy. In the figure, we have also shown the results obtained by us for a two dimensional t-J model. The square lattice results are in good agreement with those in Ref. [142].

An important feature to be noted in Fig. 3.10 is the effect of interplanar hopping on the SC order parameter. In the optimally doped region, larger single particle hopping, $t_\perp$ clearly reduces the planar SC correlations. This is also confirmed by comparing the value of Φ_d for the square lattice with that for the bilayer for the case of higher $t_\perp$. This reduction of planar superconducting correlations by single particle interlayer hopping agrees with the corresponding mean-field results for the bilayer t-J model[164]. On the other hand, the interlayer exchange coupling, $J_\perp$ is found to play a dormant as far as the range of its values considered here is concerned. The SC correlations for $J_\perp = 0.03$ (not shown here) is almost the same as that for $J_\perp = 0.10$ shown above. Interestingly, we observe an opposite behaviour in the overdoped region. Here larger $t_\perp$ seems to enhance the superconducting correlations extending the stability of the SC state to a slightly higher hole doping. This is found to be due to a change in

momentum distribution by increased $t_\perp$ in the overdoped region. This issue shall be discussed in details in the next Chapter.

3.4 Coexistence of magnetism and superconductivity

We have seen in the above that a pure d-wave superconducting wavefunction is inadequate to describe the magnetic correlations in the Mott insulating phase of the high-T_c cuprates. The wavefunction is found to grossly underestimate the AF long range order near existing in these materials near half-filling. Here we consider a variational wavefunction which provides a better description of the ground state near half-filling. It incorporates both the superconducting and antiferromagnetic orders. The energy minimization procedure yield a state of coexisting AF and SC in the underdoped region. Magnetic and superconducting correlations in the coexisting state are calculated and compared with that of the pure SC state.

3.4.1 The variational wavefunction

The variational wavefunction which we consider for describing both the AF and SC orders is given by[139, 140]

$$|\Psi_{var}(\Delta_{SC}, \Delta_{AF})\rangle = \mathcal{P}_G \mathcal{P}_N \prod_{\mathbf{k}} \left(u_{\mathbf{k}} + v_{\mathbf{k}} d^\dagger_{\mathbf{k}\uparrow} d^\dagger_{-\mathbf{k}\downarrow}\right)|0\rangle \tag{3.10}$$

where the operator $\mathcal{P}_N$ projects out the states with a fixed electron number, N and $\mathcal{P}_G = \prod_i (1 - n_{i\uparrow} n_{i\downarrow})$, is the Gutzwiller projector which imposes the condition of no double occupancy. The product in Eq. 3.10 is over the first Brillouin zone and the amplitudes $u_{\mathbf{k}}$ and $v_{\mathbf{k}}$ are defined by,

$$\frac{v_{\mathbf{k}}}{u_{\mathbf{k}}} = \phi(\mathbf{k}) = \frac{\Delta_{\mathbf{k}}}{(\mp E_{\mathbf{k}} - \mu) + \sqrt{(\mp E_{\mathbf{k}} - \mu)^2 + \Delta^2_{\mathbf{k}}}} \tag{3.11}$$

where $\Delta_{\mathbf{k}} = \Delta_{SC} f(\mathbf{k})$ represents the SC gap, $f(\mathbf{k})$ being an appropriate symmetry function of $\mathbf{k}$ and $E_{\mathbf{k}} = \sqrt{\varepsilon^2_{\mathbf{k}} + \Delta^2_{AF}}$. $\varepsilon_{\mathbf{k}} = -2t(\cos k_x + \cos k_y) - 2t_\perp \cos k_z$, is the free electron dispersion for bilayer and μ is the chemical potential. The $-$ $(+)$ sign in the denominator of Eq. 2.5

corresponds to $\varepsilon_{\mathbf{k}} < 0$ ($\varepsilon_{\mathbf{k}} > 0$). The quasiparticle operators, $d^{\dagger}_{\mathbf{k}\sigma}$ diagonalizes the AF Hartree-Fock Hamiltonian (Appendix B) with a gap Δ_{AF} and are related to the electron operators by the following transformation,

$$\begin{bmatrix} d^{\dagger}_{\mathbf{k}\sigma} \\ d^{\dagger}_{\mathbf{k}+\mathbf{Q}\sigma} \end{bmatrix} = \begin{bmatrix} \alpha_{\mathbf{k}} & \eta(\sigma)\beta_{\mathbf{k}} \\ -\eta(\sigma)\beta_{\mathbf{k}} & \alpha_{\mathbf{k}} \end{bmatrix} \begin{bmatrix} c^{\dagger}_{\mathbf{k}\sigma} \\ c^{\dagger}_{\mathbf{k}+\mathbf{Q}\sigma} \end{bmatrix} \tag{3.12}$$

with

$$\alpha_{\mathbf{k}} = \frac{1}{\sqrt{2}}\left(1 - \frac{\varepsilon_{\mathbf{k}}}{E_{\mathbf{k}}}\right)^{1/2} \qquad \beta_{\mathbf{k}} = \frac{1}{\sqrt{2}}\left(1 + \frac{\varepsilon_{\mathbf{k}}}{E_{\mathbf{k}}}\right)^{1/2} \tag{3.13}$$

Here $\mathbf{Q} = (\pi, \pi, \pi)$, is the perfect nesting vector and $\eta(\sigma) = \pm 1$ for $\sigma = \uparrow, \downarrow$.

The wavefunction in Eq. 3.10 consists of two variational parameters, viz. Δ_{SC} and Δ_{AF}. Ideally the chemical potential, μ should also be treated as a variational parameter, however here we fix it at its noninteracting value, μ_0 for reason mentioned in §3.3.2. The wavefunction describes different phases depending upon the values of the variational parameters. For $\Delta_{AF} = 0$ and $\Delta_{SC} \neq 0$, it describes the usual BCS superconducting state, whereas in the limit $\Delta_{SC} \to 0$ and $\Delta_{AF} \neq 0$, the wavefunction reduces to a state with antiferromagnetic long range order[135]. For nonzero Δ_{SC} and Δ_{AF}, the wavefunction describes a phase with coexisting AF and SC state as will be shown later, while the normal state is recovered as both the parameters vanish.

In the following sections, results will be presented only for interplanar parameter values of $(t_{\perp}, J_{\perp}) = (0.20, 0.10)$. The results for other values considered here are found to be similar. The lattice size is chosen be $8 \times 8 \times 2$.

3.4.2 Optimal gap parameter and energy

As mentioned earlier, our variational calculations supports a d-wave symmetry for the SC state. Hence we have considered this state as the superconducting pairing symmetry in the coexisting wavefunction. We refer to the d-wave SC gap by Δ_d as before, that is, we write $\Delta_{\mathbf{k}} = \Delta_d(\cos k_x - \cos k_y)$. The optimization of the wavefunction with pure d-wave SC order (for $\Delta_{AF} = 0$) is already described in §3.3.2. Here we introduce the second variational parameter, Δ_{AF} and optimize the wavefunction again, now in the parameter space of Δ_d and Δ_{AF}.

The results for the optimal parameters and the ground state energy in the underdoped region are shown in Fig. 3.11. Fig. 3.11(a) shows $\tilde{\Delta}_{AF}$, the optimal value of the antiferromagnetic gap

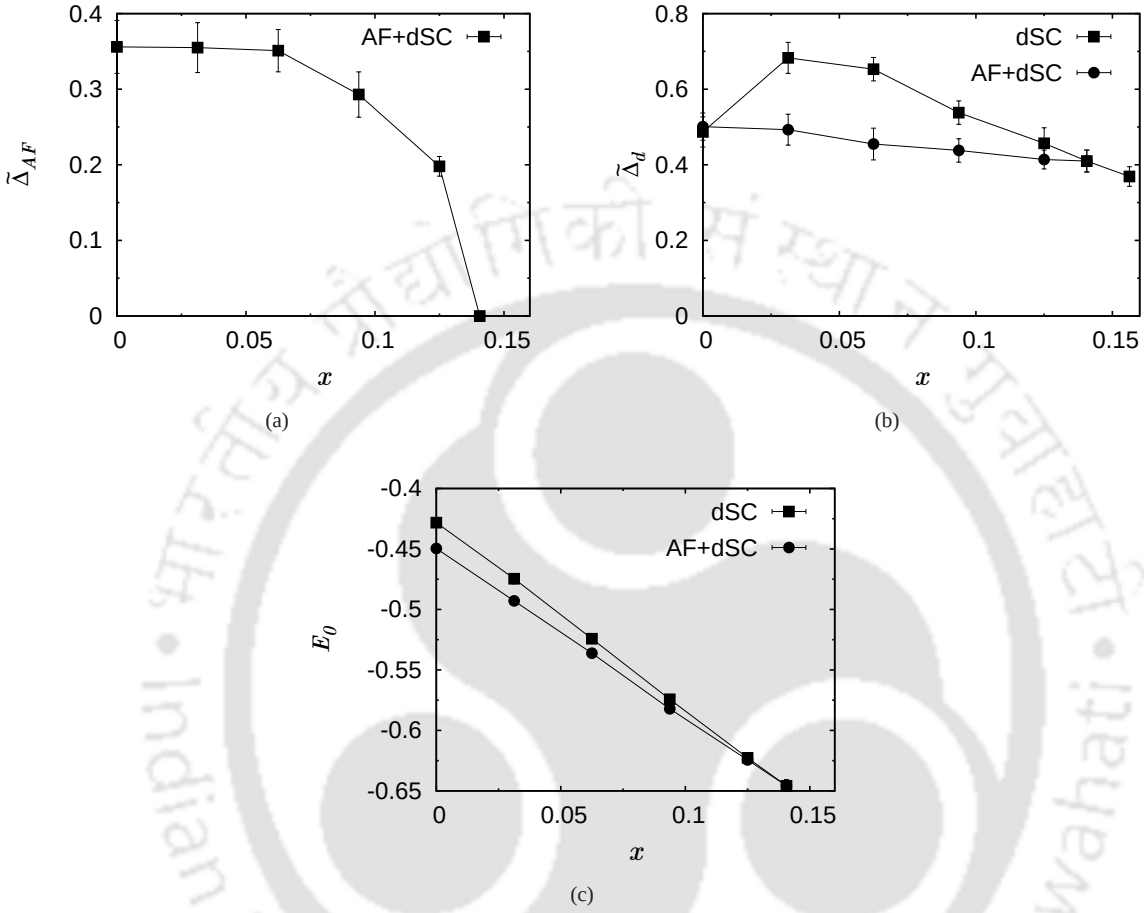

FIGURE 3.11: (a) Optimal AF gap parameter, $\tilde{\Delta}_{AF}$ for the coexisting wavefunction as a function of hole concentration. (b) Optimal SC gap parameter, $\tilde{\Delta}_d$ for both the pure d-wave SC and the coexisting phases as a function of hole concentration in the underdoped region. (c) Optimal energy, E_0 (per site in units of t) for the pure d-wave SC (dSC) and the coexisting AF & SC (AF+dSC) states as a function of hole concentration in the underdoped region. Lattice size is $8 \times 8 \times 2$ and $(t_\perp, J_\perp) = (0.20, 0.10)$.

parameter as a function of hole concentration in the underdoped region. The corresponding optimal SC gap parameter, $\tilde{\Delta}_d$ is now modified as compared to its value in the pure SC wavefunction. The values of $\tilde{\Delta}_d$ for the two wavefunctions are shown in Fig. 3.11(b). We see from the figures that $\tilde{\Delta}_{AF}$ is maximum at half-filling, decreases slowly with x for small value of x and then falls off rapidly to vanish at $\sim$ 14% hole concentration. $\tilde{\Delta}_d$ in the coexisting state is clearly reduced as compared to its value in the pure SC state. Thus in the underdoped region, below $x \sim 0.14$, we have the lowest energy state with nonzero values of $\tilde{\Delta}_{AF}$ and $\tilde{\Delta}_d$. In this

state, both the magnetic and superconducting correlations are found to be strong (shown in the next section) implying that antiferromagnetism coexists with superconductivity below this hole concentration. The optimal energies of the pure *d*-wave SC (dSC) and the coexisting AF & SC (AF+dSC) states is shown in Fig. 3.11(c) as a function of hole doping in the underdoped region. The figure shows that the energy in the coexisting state is significantly lowered near half-filling as compared to that in the pure SC state. The energy difference between the two phases is maximum at half-filling and decreases gradually with increasing hole concentration, finally vanishing at $x \sim 0.14$. It may be mentioned that the coexistence of the two phases were also observed in the two dimensional *t*-*J* model[128, 139, 140] below a hole doping which is almost same as the value obtained above for bilayer.

3.4.3 Enhanced correlations in the coexisting state

Here we calculate the magnetic and superconducting correlations in the coexisting AF & SC state and show that correlations are strong and enhanced compared with the pure SC state. First we examine the magnetic correlations in the underdoped region. Fig. 3.12, we plot the planar and interplanar spin correlations in the coexisting state at various values of hole doping. The figures show that in this case spin-spin correlations decay very slowly as compared

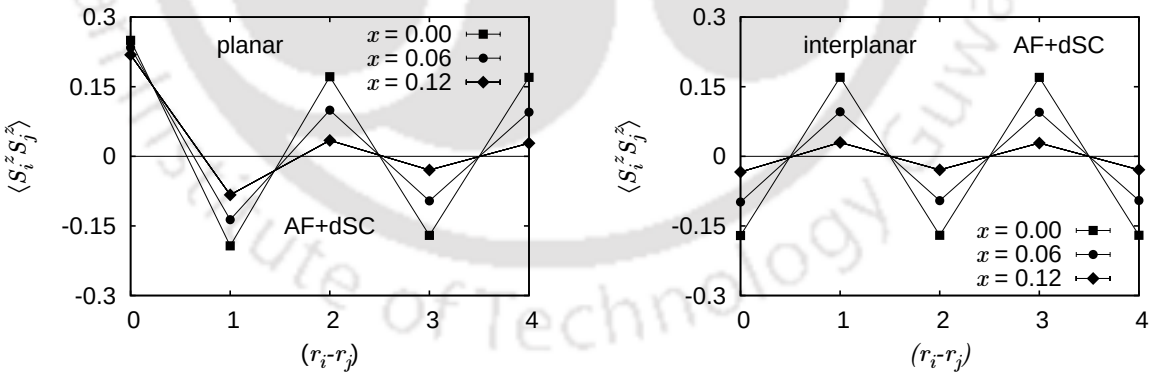

FIGURE 3.12: Spin-spin correlation as a function of distance along $\hat{x}$-direction in the coexisting AF+dSC state. The spins are on lattice sites lying (a) along an edge in a plane, and (b) on two different planes along the same direction. Lattice size is $8 \times 8 \times 2$ and $(t_\perp, J_\perp) = (0.20, 0.10)$.

to the case of pure *d*-wave SC state (Fig. 3.8(a)). Only at larger values of *x*, the correlations

show a appreciable decay with distance as seen for $x = 0.12$ in the figure. The interplanar correlations, which are very weak in the d-wave state, is almost of the same magnitude as the planar correlations in the coexisting state. The presence of magnetic order in the coexisting phase is further emphasized by plotting $S(\mathbf{q})$ versus $\mathbf{q}$ at various hole concentrations in Fig. 3.13. We see that the peaks in $S(\mathbf{q})$ at $\mathbf{q} = (\pi, \pi, \pi)$ are very sharp indicating the existence

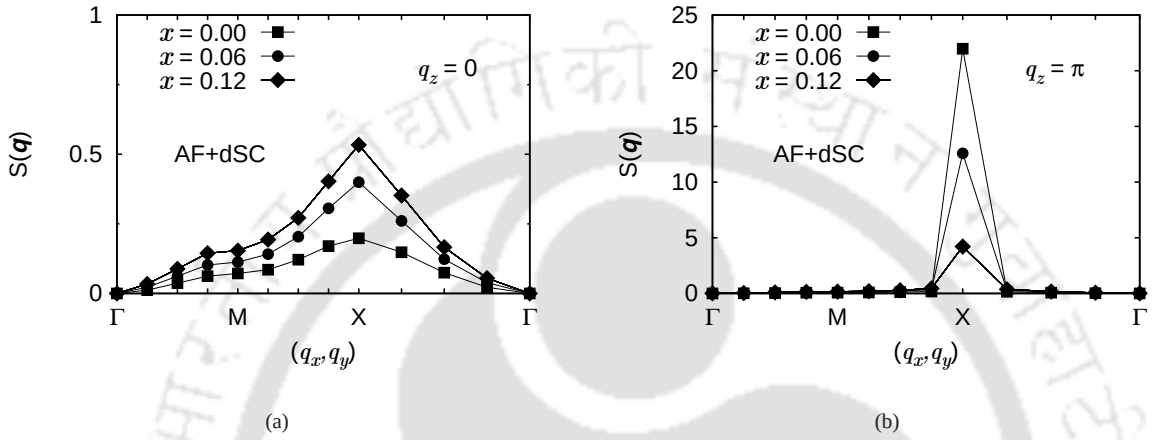

FIGURE 3.13: $S(\mathbf{q})$ for the coexisting AF & SC state as a function of (q_x, q_y) along the ΓMX path as shown in Fig. 3.8(d) for (a) $q_z = 0$ and (b) $q_z = \pi$, as various hole doping shown in the figures. Lattice size is $8 \times 8 \times 2$ and $(t_\perp, J_\perp) = (0.20, 0.10)$.

strong AFLRO in the coexisting phase. To give an quantitative estimate of the sharpness of the peaks, we calculate the ratio between the peak and the half-width at half-maximum (HWHM) of the curves. This ratio at half-filling, for the coexisting state is ~ 40 while the same for the pure d-wave state is ~ 3. A few other points may be noted regarding the behaviour of $S(\mathbf{q})$ in the coexisting state contrasted with that in the pure d-wave state (Fig. 3.8). The difference between magnitudes of $S(\pi, \pi, \pi)$ and $S(\pi, \pi, 0)$ in the coexisting state is much more larger. This is indicative of the strong interplanar AF correlations in this state. Also the variation of $S(\mathbf{q})$) with hole concentration is very contrasting in the two cases. $S(q_x, q_y, \pi)$ decreases with increasing x in both the cases which is due to the destruction of planar correlations by holes. However, $S(q_x, q_y, 0)$ shows an opposite variation in the two cases. It increases with increasing x in the coexisting state while the opposite behaviour is observed for the case of the pure d-wave state (3.8(c)). The former behaviour is understood as follows. Away from half-filling, the holes destroy interplanar AF correlations more effectively than planar correlations because of the lower energy cost in doping so, as $J_\perp < J$. This can be observed by comparing the spin correlations in Fig. 3.12(a) and 3.12(a) for the larger value of hole doping,

e.g. $x = 0.12$. $S(q_x, q_y, 0)$ increases with x because of this weaker interplanar AF correlations away from half-filling as compared to the situation at half-filling where planar and interplanar correlations are of same magnitudes. As for the case of pure d-wave state, the decrease of $S(q_x, q_y, 0)$ with x is a reflection of the fact that interplanar correlations in the state is negligible at all hole doping. Finally we mention that, though the coexisting state provides a better description of the magnetic properties of the ground state, its prediction of a robust AF order in the SC state far away from half-filling is not observed experimentally.

Our next task is to examine how the SC correlations are affected by the coexisting AF order. For this purpose, we calculate the SC pair-pair correlations, $F_{\alpha,\beta}(\mathbf{r} - \mathbf{r}')$ and the corresponding order parameter, Φ_d as described before. The results for Φ_d for the coexisting state and for the pure d-wave state are compared in Fig 3.14. The figure shows that in the region

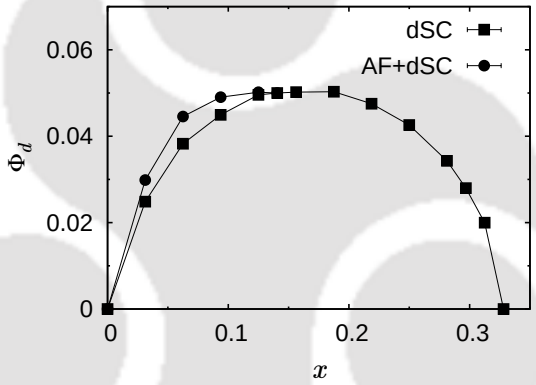

FIGURE 3.14: SC order parameter, Φ_d as a function of hole concentration, x for the coexisting AF & SC and the pure SC state. Lattice size is $8 \times 8 \times 2$ and $(t_\perp, J_\perp) = (0.20, 0.10)$.

of hole doping where the two phases coexists, the SC order parameter, Φ_d has significantly higher magnitude. Thus the superconducting correlations in the coexisting state of AF and SC are enhanced as compared to that in the pure SC state. Earlier we have noted the AF correlations are enhanced in the coexisting state as expected. However the enhancement of SC correlations also is very interesting. More so, if we compare the behaviour of the superconducting gap parameter, $\tilde{\Delta}_d$ in the two phases. $\tilde{\Delta}_d$ is clearly diminished in the coexisting state as shown earlier in Fig. 3.11(b). However Φ_d shows the opposite behaviour and it increases in coexisting phase.

3.5 Summary

We have studied the superconducting and magnetic properties of the bilayer *t-J* model for parameters relevant to bilayer superconductors. Three possible pairing symmetries of the superconducting state were considered. The energy minimization yield the planar $d_{x^2-y^2}$ state to be the most suitable one to study superconductivity. Subsequently the $d_{x^2-y^2}$ wavefunction was optimized at various hole doping for different values of the interplanar parameters. The magnetic and superconducting correlations were studied in details and compared with square lattice results. We observed no qualitative differences between the bilayer and single layer results, though some quantitative differences exist. Larger interplanar hopping was found to reduce planar superconducting correlations in the optimally doped region, whereas it enhances it the overdoped region. Interlayer exchange coupling has no effect on the superconducting correlations for the range of its values considered. The magnetic correlations were found to be very weakly dependent on the interplanar parameters. We have also examined the issue of coexistence of antiferromagnetism and superconductivity in the bilayer. We found that these two phases coexist in the underdoped region upto about 15% hole concentration. In the coexisting phase, interestingly both the magnetic and superconducting are significantly enhanced.

Chapter 4

Role of interlayer couplings: A ground state phase diagram

4.1 Introduction

In the previous chapter, we studied the properties of the bilayer t-J model for the values of the interlayer coupling parameters which are thought to be relevant to the high-T_c superconductors. However, it has always been of general interest for a model of strongly correlated electron to understand its various phases in different ranges of its parameter values. The phase diagrams of the two dimensional t-J and Hubbard models which capture the basic physics of the cuprate superconductors, have been studied in extensive details in the past using a variety of analytical and numerical techniques.

Apart from the general interest, the estimated values of interlayer coupling parameters in bilayer cuprates are also not accurate. Especially the hopping parameter can not be measured directly in experiments and its estimates from band structure calculations may not be correct. In this work, we consider a larger range of values for the interplanar parameters of the bilayer t-J model by keeping the planar parameters fixed, and study its properties using the variational Monte Carlo technique. Specifically, we vary interlayer hopping, $t_\perp$ from a small value to a value equal to t (planar hopping parameter) and interlayer exchange, $J_\perp$ from $0.10t$ to $0.35t$ ($=J$, planar exchange parameter). Thus we obtain a ground state phase diagram for the model

as a function of interplanar hopping, $t_\perp$ and hole concentration, x for a few values of interplanar exchange parameter, $J_\perp$. The phase diagram shows rich features, such as a coexistence of antiferromagnetism and superconductivity at underdoping, planar (d-wave) and interplanar (d_z-wave) superconducting correlations for respectively small and large $J_\perp$, etc. It may be mentioned that the d_z-wave gap function (defined in §3.3.1) in combination with the d-wave gap was thought to be a possible candidate to explain the observed eight nodes energy gap structure in bilayer superconductors as described in §3.3.1. In fact, mean-field study of the t-J model found a combination of these two gap symmetries to be favourable in bilayer[205]. However our VMC study show that these two symmetries are stabilized separately in different range of parameter values. The planar and interplanar superconducting orders are never found to coexist for any of the parameter values that we have considered. Other interesting features in the phase diagrams include a non-monotonic variation of the phase boundary between the d-wave superconducting and normal phases as a function of $t_\perp$, where small interplanar hopping enhances superconducting correlations in the overdoped region before destroying it eventually for large $t_\perp$.

4.2 The trial wavefunction and optimization scheme

The variational wavefunction considered here is same as the one considered in §3.4 for describing the coexisting state of superconductivity (SC) and antiferromagnetism (AF). The wavefunction is defined in Eq. (3.10). For the pairing symmetry for the superconducting state, here we have considered a few more ansatz functions in addition to the earlier ones (Eq. (3.6)). The full list of choices for Δ_k is, (a) $\Delta(\cos k_x - \cos k_y)$ (d-wave), (b) $\Delta \cos k_z$ (d_z-wave). (c) $\Delta_\parallel(\cos k_x - \cos k_y) + \Delta_\perp \cos k_z$, (d) $\Delta_\parallel(\cos k_x - \cos k_y) + \Delta_\perp(1 - \cos k_z)$, (e) Δ (s-wave) and (f) $\Delta_k = \Delta(\cos k_x + \cos k_y)\cos k_z$ where the + (−) sign is for $k_z = 0$ (π) (extended $s^\pm$ state).

Thus the variational parameters of the wavefunction with different pairing symmetries are $\Delta_\parallel$ and $\Delta_\perp$ or Δ in addition to AF gap parameter Δ_{AF} (Eq. (3.10)). The chemical potential, μ is fixed to its value for the noninteracting system for reason mentioned earlier in §3.3.2. Out of the maximum three variational parameters, we shall see later that the wavefunctions with two the coexisting SC gap parameters, e.g. $\Delta_\parallel$ and $\Delta_\perp$ are never stabilized in any region of parameter space. Thus mostly we have to deal with two variational parameter, one being the SC gap parameter which we denote by Δ_{SC} and the other Δ_{AF}. Since we need to optimize the

wavefunction at a very large number points in the Hamiltonian parameter space formed by the two interplanar parameters and hole doping, it is desirable to have an efficient optimization scheme so that the optimal variational parameters can be determined accurately in a reasonable time. The conventional methods for finding the minimum of a multivariable function can not be applied here because it still involves evaluation of the function at large number of points. Another concern in this case is that the calculations are statistical. In conventional minimum finding methods, it is difficult to take into account the statistical fluctuations in the evaluated values of the function. In VMC, special schemes have been proposed for efficient optimization multiparameter wavefunctions[206, 207]. However, here we adopted a straightforward method which enabled us to locate an optimal point fairly accurately without the possibility of getting trapped into any local minimum. The procedure for the cases of two variational parameters is as follows.

For subsequent discussion, let $x \equiv \Delta_{AF}$ and $y \equiv \Delta_{SC}$. For minimization, we first select a wide region in the two dimensional parameter space formed by x and y, and then divide it into a coarse grid of points. Energies are evaluated at these points with smaller number of Monte Carlo sweeps (MCS). This yields a rough estimate of the minimum position of the resulting energy surface. Next, a finer grid is taken around the estimated optimal point and energy evaluations are done again, now with larger number of MCS. Fig. 4.1 shows such an energy surface obtained in the second step. Let us denote the corresponding data set as

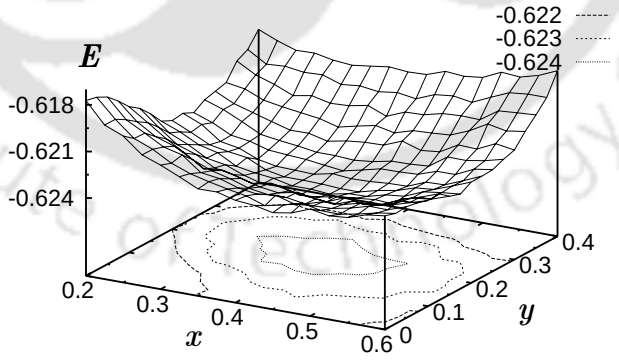

FIGURE 4.1: Variational energy E of the coexisting d-wave SC and AF state as a function of x ($\equiv \Delta_{SC}$) and y ($\equiv \Delta_{AF}$) at hole concentration, $x = 0.14$. The interplanar parameter values are, $t_\perp = 0.20$, $J_\perp = 0.10$.

$\{(x_i, y_j, E_{ij}) |\ i = 0, \ldots, m;\ j = 0, \ldots, n\}$. To locate the optimal point, we first fit a polynomial

$E_j^1(x)$ to the data $\{(x_i, E_{ij})|\ i = 1, \ldots, m\}$ for each fixed values of j. Suppose the minimum of the polynomial E_j^1 falls at x_j^* and let $E_j^* = E_j^1(x_j^*)$. These E_j^* for various j gives rise to a new data set $\{(y_j, E_j^*)|\ j = 1, \ldots, n\}$. To this data, we fit another polynomial $E^2(y)$. Let the minimum of $E^2(y)$ be obtained at $y = y_0$. The corresponding minimum, $E_0 = E^2(y_0)$ is taken to be the optimal value energy. The plot of $E^2(y)$ for the data set of our current example is shown in Fig. 4.2(a). Finally x_0, the value of optimal x is obtained by interpolating data (y_j, x_j^*) at y_0 as shown in Fig. 4.2(b).

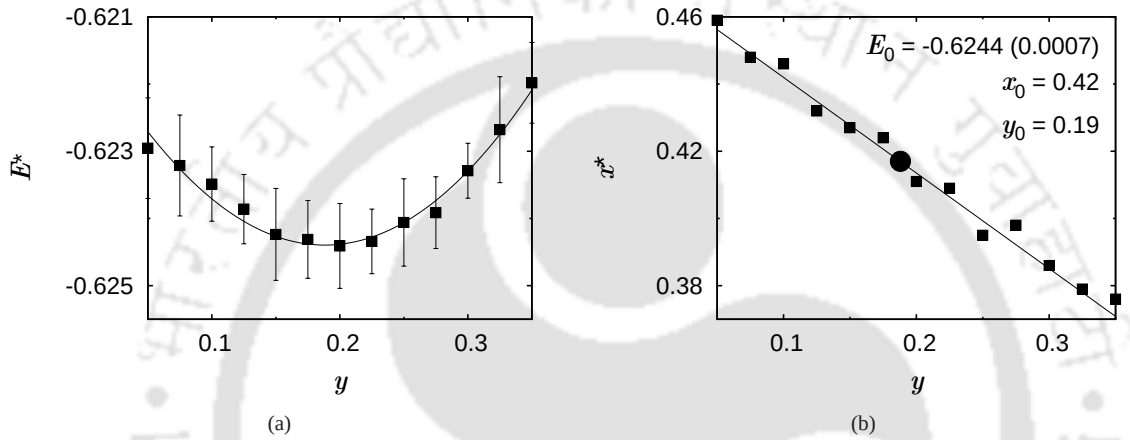

FIGURE 4.2: Determination of the global minimum and the corresponding optimal parameters for the energy surface shown in Fig. 4.1. (a) The energy, E^* as a function of y (see text). The solid line is a quadratic polynomial fit to the data points. (b) x^* as a function of y. The solid line is a linear fit to the data points. The filled circle is the value of x^* corresponding to y_0.

4.3 Phase diagram

We have optimized the energy with respect to the wavefunction with different pairing symmetries for various $t_\perp$ and hole doping, x for three different values of $J_\perp$. The lattice size is chosen to be $8 \times 8 \times 2$. The parameter values and energies are quoted in units of t.

4.3.1 $J_\perp = 0.10$ phase

The phase diagram in $t_\perp - x$ plane for $J_\perp = 0.10$ is shown in Fig. 4.3. In this case, energy calculations show that the SC phase has only d-wave pairing symmetry. In fact, the other

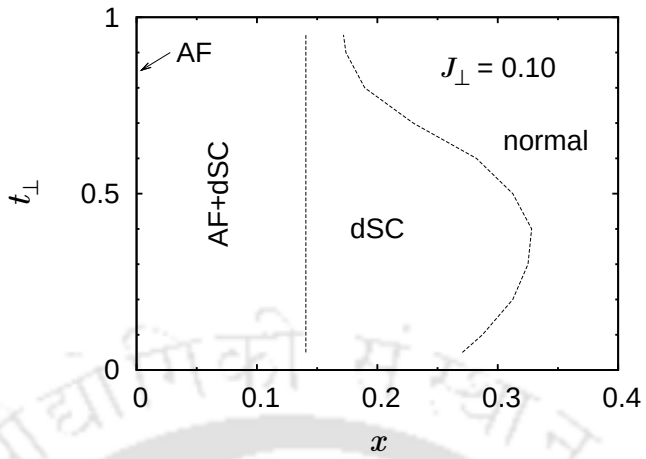

FIGURE 4.3: Phase diagram in the $t_\perp - x$ plane for $J_\perp = 0.10$.

pairing symmetries considered here have energies higher than that of the normal state and hence are out of the competition. AT half-filling ($x = 0$), the system is insulating and has AF long range order (AFLRO). The insulating behaviour at half-filling is a consequence of the suppression of charge fluctuations enforced by the Gutzwiller projection operator. Away from half-filling, there is a coexistence of *d*-wave SC and antiferromagnetism (AF+dSC phase) upto $x \sim 0.14$ for all values of $t_\perp$. Evidence of the coexisting phase in the underdoped regime was already seen for $t_\perp$ upto 0.2 in the last chapter. The same is seen to persist here even at larger values of $t_\perp$. Beyond $x \sim 0.14$, pure *d*-wave SC (dSC) phase emerges as the stable state upto a hole concentration, x_c which strongly depends on $t_\perp$. We observe interesting features of the boundary separating the SC and the normal phase in the overdoped region. Starting at $t_\perp = 0$, the boundary extends towards larger values of hole doping upto about $t_\perp \sim 0.3$, beyond which it turns towards smaller x with further increase in $t_\perp$. Naively, larger $t_\perp$ should destroy planar SC correlations by delocalizing the pairs across the planes. However a close look at the momentum distribution function $n(\mathbf{k})$ ($= \langle c^\dagger_{\mathbf{k}\sigma} c_{\mathbf{k}\sigma} \rangle$ in the overdoped region reveals that there is a significant transfer of spectral weight from $k_z = \pi$ plane to $k_z = 0$ plane with increasing $t_\perp$, implying the emergence of a robust *d*-wave SC phase at moderate $t_\perp$. At larger values of $t_\perp$ the delocalizing effect takes over and we observe a vanishing of the SC phase at lower values of hole doping. These effects are described in details in a following section.

4.3.2 $J_\perp = 0.20$ phase

The most interesting phase diagram (owing to maximum number of phases) is exhibited by the moderate value of the interplanar exchange, $J_\perp$, e.g. 0.20 (Fig. 4.4). In this phase diagram,

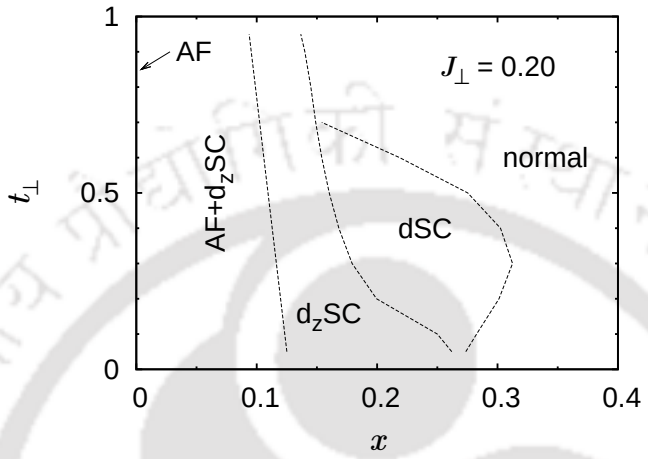

FIGURE 4.4: The phase diagram for $J_\perp = 0.20$.

an SC state with a different pairing symmetry, $\Delta_{\mathbf{k}} = \Delta \cos k_z$ (i.e. d_z-wave, as mentioned earlier) emerges as the stable ground state over a wide range of parameter values. The d_z-wave state competes energetically with the d-wave state over the whole SC phase region in the phase plane. In the under- and optimally doped region, the d_z-wave state yields lower energy than the d-wave state. The half-filled phase is AF insulating as before. In the underdoped regime, antiferromagnetism coexists with the d_z-wave SC state (AF+d$_z$SC phase) upto a hole concentration which seems to decrease slightly with increasing $t_\perp$. The optimally doped phase is pure d_z-wave superconducting (d$_z$SC phase). This phase yields lower energy upto a hole concentration which has a strong $t_\perp$ dependence as shown in the figure. It is worth mentioning here that the d_z-wave pairing symmetry is characterized by strong interplanar and weak planar SC correlations as discussed in the next section. In the overdoped regime, however, the d-wave state wins over and shows the similar variation of the boundary between the SC and the normal state as in the $J_\perp = 0.10$ phase diagram. Energies of all other pairing symmetries are found to be higher than that of the normal state at all values of $t_\perp$ and x.

4.3.3 $J_\perp = 0.35$ phase

Finally we consider the phase diagram for large $J_\perp$, i.e. $J_\perp = J = 0.35$. The phase diagram is shown in Fig. 4.5. The presence of the coexistence of AF and d_z-wave SC phase at underdoped

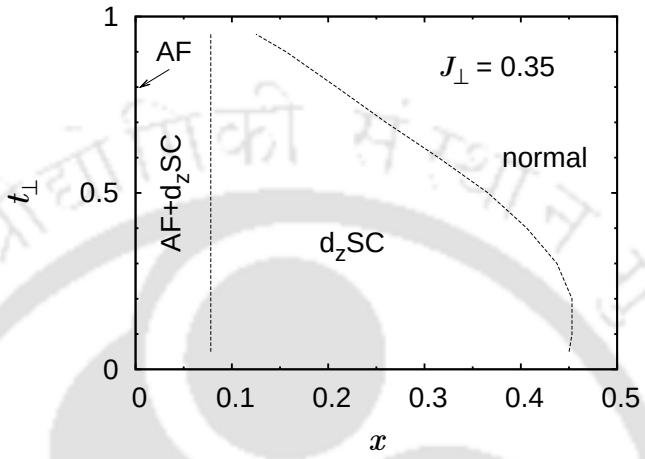

FIGURE 4.5: The phase diagram is shown for large $J_\perp$ i.e. $J_\perp = 0.35$. The d_z-wave SC is the dominating phase here.

regime is predictable. However the range of hole doping for the coexisting phase is smaller than that in the previous case ($J_\perp = 0.20$). The interplanar (d_z-wave) correlations owing to larger $J_\perp$ now spans all of the overdoped region and extends all the way upto $x \sim 0.45$ for small $t_\perp$. The d-wave state no longer yields lower energy in any region of the parameter space unlike in the previous cases. The phase boundary between the d_z-wave SC and normal state moves towards smaller x with increasing $t_\perp$.

4.4 Effect of interlayer couplings

The phase diagrams presented above show a number of interesting features. We see that a planar d-wave superconducting state for smaller $J_\perp$ replaced by the d_z-wave state for larger $J_\perp$. For the moderate value of $J_\perp$, these two phases are found to stabilize separately in different regions of hole doping. The superconducting phase in all the cases coexists with the antiferromagnetism in the underdoped region upto a varied strength of hole doping. Interplanar hopping destroys superconducting correlations except for the d-wave state in overdoped

region where it stabilizes superconductivity. Here we examine effects of the interplanar coupling parameters on various quantities of interest. Also, the nature of SC correlations in the d_z-wave state is unknown unlike in the case of d-wave state. Therefore we shall calculate the SC pair-pair correlations for the d_z-wave state and examine its behaviour.

4.4.1 Energy gaps

First we discuss the variation of the AF and SC energy gaps with interlayer hopping and hole concentration for different values of $J_\perp$. For distinction, we define $\tilde{\Delta}_d$ and $\tilde{\Delta}_{d_z}$ to be the optimal SC gap for the d-wave and d_z-wave states in the phase diagram, respectively. Fig. 4.6 shows the variation of $\tilde{\Delta}_d$ with $t_\perp$ for a few different hole doping, x for $J_\perp = 0.10$. The energy gap shows different variation with $t_\perp$ at different hole doping. At half-filling, $\tilde{\Delta}_d$

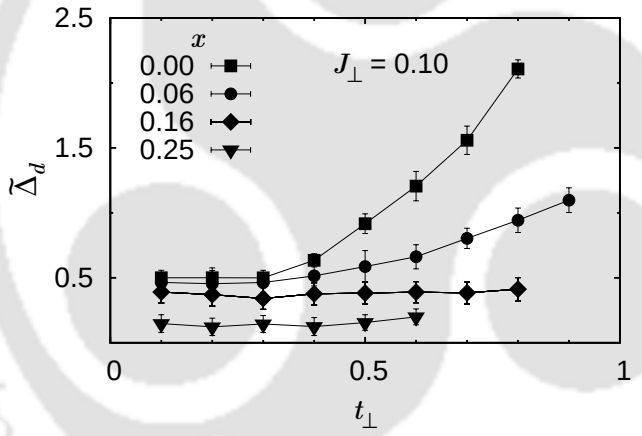

FIGURE 4.6: Dependence of the optimal d-wave SC gap, $\tilde{\Delta}_d$ on interlayer hopping, $t_\perp$ at different hole doping, x. $J_\perp = 0.10$.

increases with increasing $t_\perp$ whereas slightly away from half-filling, the increase is moderate. The two curves in the optimal ($x = 0.16$) and overdoped ($x = 0.25$) regions show that $\tilde{\Delta}_d$ is almost independent of $t_\perp$. This result is to be compared with a corresponding result obtained in a slave-boson mean field (SBMFT) results on bilayer t-J model[165], which corroborates increase of $\tilde{\Delta}_d$ with $t_\perp$ in the underdoped region. The dependence of the energy gap, $\tilde{\Delta}_{d_z}$ for the d_z-wave state on $t_\perp$ and x is shown in Fig.4.7. In this case, we observe an opposite behaviour of the energy gap as compared with that of $\tilde{\Delta}_d$. $\tilde{\Delta}_{d_z}$ decreases with increasing $t_\perp$ for all values of x. Also for a fixed $t_\perp$, the gap increases slightly initially and then falls off rapidly for larger

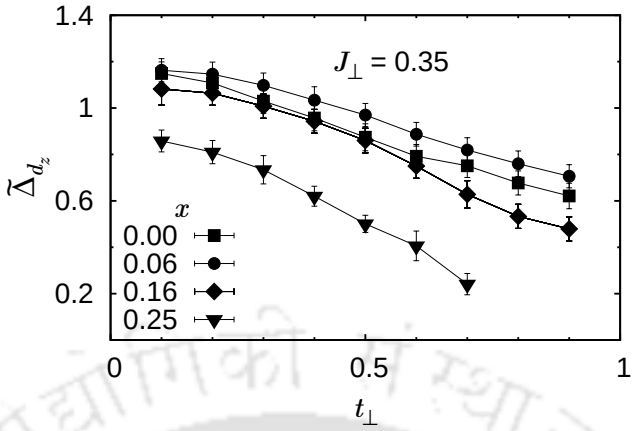

FIGURE 4.7: Dependence of the optimal d_z-wave SC gap, $\tilde{\Delta}_{d_z}$ on interlayer hopping, $t_\perp$ at different hole doping, x. $J_\perp = 0.35$.

hole doping. On the other hand, the magnitude of the AF gap, $\tilde{\Delta}_{AF}$ is found to be more or less independent of $t_\perp$. With regard to its doping dependence, $\tilde{\Delta}_{AF}$ is maximum at half-filling and decreases rapidly with increasing hole concentration. This is shown in Fig. 4.8 for the case of $J_\perp = 0.10$. For other values of $J_\perp$, the behaviour of $\tilde{\Delta}_{AF}$ is same except that it vanishes much more rapidly with hole doping for larger $J_\perp$.

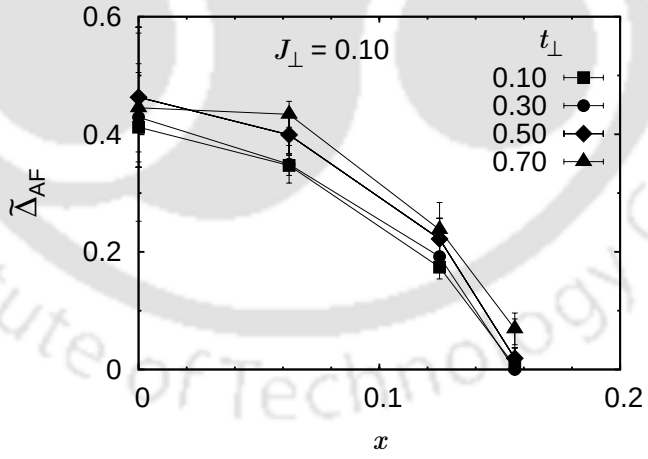

FIGURE 4.8: Doping dependence of the AF gap, $\tilde{\Delta}_{AF}$ for a few values of $t_\perp$ shown in figure. $J_\perp = 0.10$.

4.4.2 Superconducting correlations

Earlier we have mentioned about the non-monotonic variation of the phase boundary between the SC and normal state or equivalently the variation of critical hole concentration, x_c where the SC phase vanishes, with interlayer hopping. For the d-wave state in the $J_\perp = 0.10$ and 0.20 phase planes, x_c increases initially with increasing $t_\perp$, reaches a maximum at $t_\perp \sim 0.3$ and then decreases sharply. Here we try to explain this feature on the basis of energetics. We find that increasing $t_\perp$ can have two contrasting effects on the d-wave SC correlations. Let us look the momentum distribution, $n(\mathbf{k})$ for the d-wave state in the overdoped region. It is calculated as,

$$n(\mathbf{k}) = \frac{1}{2}\sum_{\sigma}\langle c^{\dagger}_{\mathbf{k}\sigma} c_{\mathbf{k}\sigma}\rangle \tag{4.1}$$

In Fig. 4.9, we plot the two dimensional projection of the momentum distribution function in the $k_z = 0$ and $k_z = \pi$ planes for two different interplanar hopping parameters in the overdoped region of the $J_\perp = 0.10$ phase diagram. The values of the hopping parameter are chosen to

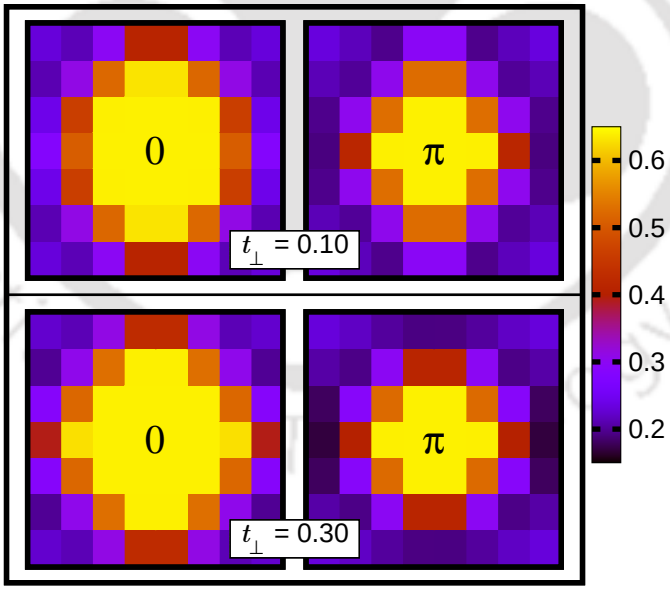

FIGURE 4.9: Plots of $n(\mathbf{k})$ for the d-wave state at hole concentration, $x = 0.28$, projected on a two dimensional (k_x, k_y) plane for $k_z = 0$ and $k_z = \pi$ marked in the figures. The top panel shows $n(\mathbf{k})$ for $t_\perp = 0.10$ while the bottom panel corresponds to $t_\perp = 0.30$. $J_\perp = 0.10$.

be, $t_z = 0.10$ and 0.30 and hole concentration, $x = 0.28$. Around this doping, we see the SC-normal phase boundary extending towards higher doping region as we go from $t_z = 0.10$ to $t_z = 0.30$. The plots in the figure show a significant redistribution of $n(\mathbf{k})$ weights in the two momentum planes as $t_\perp$ is increased. Comparing the plots for the two different values of t_z, we see that the spectral weights shift from the $k_z = \pi$ plane to the $k_z = 0$ plane as $t_\perp$ is increased from 0.10 to 0.30. Thus for larger $t_\perp$, occupation of the pairs with $k_z = 0$ is higher in the overdoped region. This favours the stability of the SC phase, as the $k_z = 0$ pairs are planar and contribute to the development of the SC pairings which for the *d*-wave state are essentially planar. The $k_z = \pi$ pairs are interplanar and hence are not expected to be important as far as the *d*-wave state is concerned. We believe that this transfer of weight from $k_z = \pi$ to $k_z = 0$ plane as $t_\perp$ is increased helps in stabilizing the SC order in the overdoped region for small values of $t_\perp$. For larger $t_\perp$ however, hopping frequency of the electrons across the planes increases and consequently the probability of breaking a planar pair becomes increasing greater. Thus we see a rapid fall of x_c for larger $t_\perp$. To provide evidence for this, we look at the interlayer hopping energy and planar exchange energy for the *d*-wave state as a function of $t_\perp$. This is shown in Fig. 4.10. In Fig. 4.10(a), we plot the interplanar hopping energy, $E^t_\perp$ (= $\langle \mathcal{H}^t_\perp \rangle$ per site) scaled by $t_\perp$ as a function of $t_\perp$. The lowering of this quantity

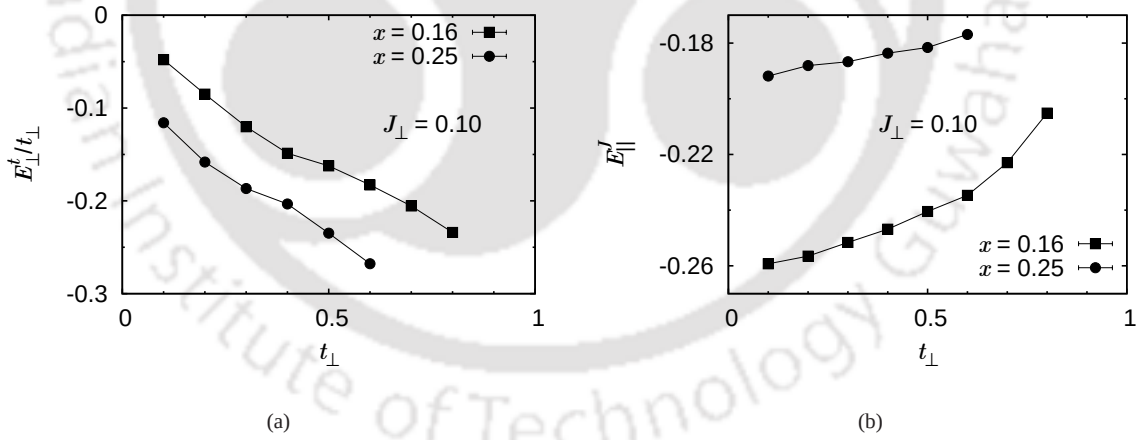

FIGURE 4.10: (a) Interplanar hopping energy scaled by $t_\perp$, $E^t_\perp/t_\perp$ and (b) planar exchange energy, $E^J_\parallel$ for the *d*-wave SC state as a function of $t_\perp$. The values of hole concentrations are shown in the figures. $J_\perp = 0.10$.

with increasing $t_\perp$ as observed in the figure, is an indication of occurrence of higher interlayer hopping frequency of electrons for larger $t_\perp$. The disruption of planar pairings by the enhanced interplanar hopping is confirmed by the loss of planar exchange energy, $E^J_\parallel$ (= $\langle \mathcal{H}^J_\parallel \rangle$ per site) for larger $t_\perp$, which is shown in Fig. 4.10(b). On the other hand, for the case of d_z-wave

state in the $J_\perp = 0.35$ phase plane, we see that x_c decreases uniformly with increasing $t_\perp$, except for small $t_\perp$ where variation of x_c is negligible. This is probably due to the fact that the mechanism for enhancement of planar SC correlations by increased $t_\perp$ mentioned above is not operative in this case. However the pair breaking effect of interlayer hopping of electrons continues to exist for the interlayer pairs as indicated by the loss of interlayer exchange energy in the d_z-wave SC state with increasing $t_\perp$ in Fig. 4.11.

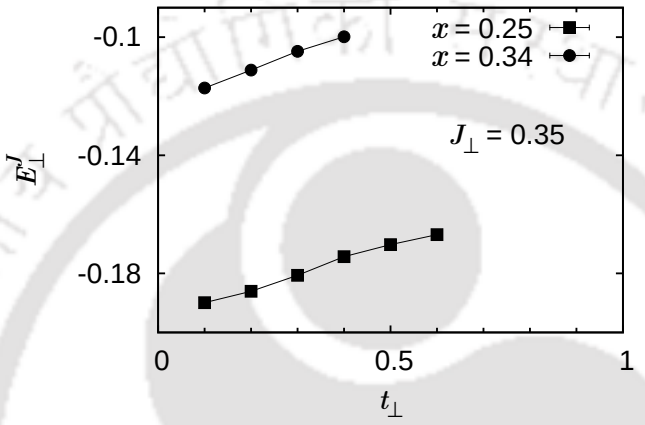

FIGURE 4.11: Interplanar exchange energy, $E_\perp^J$ for the d_z-wave state as a function of $t_\perp$ for two different hole concentrations. $J_\perp = 0.35$.

To investigate the effect of interlayer couplings on the superconducting correlations, we calculate the SC order parameter, Φ defined as (see §3.3.4),

$$F_{\alpha,\beta}(\mathbf{r}-\mathbf{r}') \rightarrow \pm\Phi^2 \tag{4.2}$$

where $F_{\alpha,\beta}(\mathbf{r}-\mathbf{r}') = \left\langle B^\dagger_{\mathbf{r}\alpha} B_{\mathbf{r}'\beta} \right\rangle$. The operator $B^\dagger$ defined as $B^\dagger_{\mathbf{r}\alpha} = \frac{1}{2}(c^\dagger_{\mathbf{r}\uparrow} c^\dagger_{\mathbf{r}+\alpha\downarrow} - c^\dagger_{\mathbf{r}\downarrow} c^\dagger_{\mathbf{r}+\alpha\uparrow})$ creates a singlet pair at two nearest neighbour sites $\mathbf{r}$ and $\mathbf{r}+\boldsymbol{\alpha}$. The unit vectors $\boldsymbol{\alpha}, \boldsymbol{\beta}$ can be either $\hat{x}$, $\hat{y}$ or $\hat{z}$. We further define, $\Phi \equiv \Phi_d$ when both $\boldsymbol{\alpha}$ and $\boldsymbol{\beta}$ lie in a single plane with the $+(-)$ signs in Eq. (4.2) referring to the case when α parallel (perpendicular) to β. For $\boldsymbol{\alpha}, \boldsymbol{\beta}$ both equal to $\hat{z}$, we define $\Phi \equiv \Phi_{d_z}$ which denotes the order parameter corresponding SC correlations across the planes.

The SC pair-pair correlations, F shows very different behaviour in the d- and d_z-wave states. For the d-wave state, the SC correlations in plane are strong and is long range ordered. In comparison, the correlations between two interplanar pairs ($F_{\alpha,\beta}$ for $\boldsymbol{\alpha} = \boldsymbol{\beta} = \hat{z}$)

are found to be very weak, roughly an order of magnitude smaller than that of the planar correlations. The order parameter, Φ_d corresponding to the planar correlations in the *d*-wave state is shown in Fig. 4.12(a) as a function of hole doping for different values of interlayer hopping. While the dome shaped structure of Φ_d has been observed and explained before

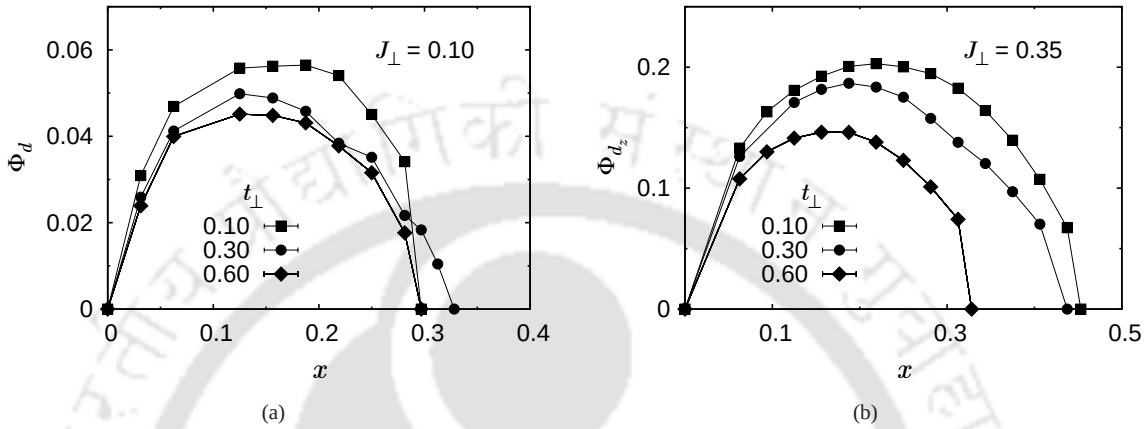

FIGURE 4.12: SC order parameter as a function of hole doping at different values of interlayer hopping. (a) Order parameter, Φ_d corresponding to planar correlations for the *d*-wave SC state ($J_\perp = 0.10$). (b) Order parameter, Φ_{d_z} corresponding to interplanar correlations for the d_z-wave SC state ($J_\perp = 0.35$). Interplanar (planar) SC correlations for the *d*-wave (d_z-wave) state are negligibly small.

for planar systems[142], here it is interesting to note the effect of $t_\perp$ on the correlations. The figure shows that single electron interlayer hopping reduces the SC correlations at all values of doping, except for in the overdoped region where superconductivity enhances for moderate values of $t_\perp$. This should be contrasted with the variation of the SC gap, $\tilde{\Delta}_{SC}$, which increases with $t_\perp$ in the underdoped region as shown earlier. It may be mentioned that while Φ_d scales with the transition temperature, T_c of cuprate superconductors, the gap $\tilde{\Delta}_{SC}$ scales with T^*, the temperature scale for the pseudogap generic to the underdoped cuprates. On the other hand, the superconducting correlations in the d_z wave state are found to be predominantly interplanar. This is a consequence of large $J_\perp$ which make the formation of interlayer pairs energetically favourable. The corresponding order parameter, Φ_{d_z} for $J_\perp = 0.35$ is shown Fig. 4.12(b). It is remarkable that the interplanar d_z-wave correlations is almost an order of magnitude stronger than the planar *d*-wave correlations as seen in the figure. The correlations between planar pairs in this case are very weak and are not shown. Another appealing feature is that in spite of the very different nature of the SC correlations, we observe the same dome

like structure of Φ_{d_z} as a function of x which is interesting. Also to be noted is the fact that the interlayer hopping $t_\perp$ reduces SC correlations similar to the d-wave case.

4.4.3 Magnetic correlations

Further, a probe into the magnetic correlations reveals that three dimensional antiferromagnetic long range order (AFLRO) exists in the region of hole doping where AF and SC coexist. Effects of interlayer couplings, $t_\perp$ and $J_\perp$ on the strength of the AF correlations are negligible. This is confirmed by calculating the planar and interplanar spin-spin correlations as a function of $t_\perp$ and $J_\perp$ (not shown here). However the AFLRO is destroyed rapidly by holes and it goes down with hole doping in a similar fashion as $\tilde{\Delta}_{AF}$.

4.5 Summary

Our variational studies on a t-J bilayer coupled by interplanar hopping ($t_\perp$) and exchange ($J_\perp$) reveals an interesting ($t_\perp - x$) phase diagram. We consider three representative values of $J_\perp$ ($= 0.10, 0.20, 0.35$). For $J_\perp = 0.10$, the stable pairing symmetry of the SC state is d-wave which is characterized by strong planar and weak interplanar SC correlations. Increasing the strength of interlayer exchange coupling changes the nature of the SC state drastically. At $J_\perp = 0.35$, the stable pairing of the SC state becomes the d_z-wave state at all hole doping which is characterized by negligible planar and very strong interplanar SC correlations. At moderate values of $J_\perp$ (=0.20), the d_z-wave SC state in underdoped regime makes transition to the d-wave state in the overdoped region. Antiferromagnetism coexists with the SC state at underdoping in all the three cases. Single particle interlayer hopping has other interesting effects on the superconducting properties. Larger $t_\perp$ enhances the d-wave SC gap at underdoping while it reduces the d_z-wave SC gap at all values of doping. On the other hand, it reduces the SC order parameter in both the cases. However in the overdoped region, moderate values of $t_\perp$ tends to enhance the d-wave SC correlations to higher hole doping. We conclude by mentioning that usually phase separation (PS) is an interesting topic in the study of phase diagrams for planar systems, however there are enough evidences that PS is not an issue for the value of (planar) J we have chosen in our study (viz. $J = 0.35$)[208, 209, 210] and hence does not figure in our discussion.

Chapter 5

Interlayer pair tunneling in bilayer: A variational calculation

5.1 Introduction

The idea of interlayer pair tunneling (ILPT) in high-T_c superconductors was introduced by Wheatley *et al*[211, 212] in order to explain the occurrence of the high transition temperatures in the materials. The mechanism of ILPT forms one of the vital components of the theory of high-T_c superconductivity proposed by Anderson[26]. According to this theory, superconductivity originates in the individual CuO_2 layers by way of pairing of electrons that may be caused either by electron-phonon interactions or by spin fluctuations. Coherent single particle hopping between two CuO_2 layers is blocked in the normal state due to the non-Fermi liquid nature. This explains the observed *c*-axis anisotropies in various physical properties in the normal state. In the superconducting state however, Cooper pairs from one CuO_2 plane can tunnel to an adjacent plane by the Josephson tunneling mechanism. This delocalization process is coherent and it lowers the kinetic energy substantially by accessing the *c*-axis dynamical degrees of freedom which is forbidden in the normal state. The possibility of coherent tunneling of singlet pairs was revisited by Muthukumar *et al*[213] who showed that the matrix elements for interlayer hopping of an electron pair is nonzero and hence the corresponding Green's function has a coherent part, while single particle tunneling across the layers is forbidden. The ILPT theory[26] proposes that this coherent tunneling of

pairs enhances superconducting correlations preformed in the CuO_2 planes and provides a large condensation energy leading to the high values of T_c. Thus within the ILPT scenario, superconductivity is driven by a gain in kinetic energy in contrast to the BCS theory where the condensation energy is provided by an overall gain in potential energy, a possibility believed to be operative for cuprates superconductors. The consequences of ILPT to a conventional superconducting state was studied by Chakravarty *et al*[148]. They showed that planar momentum conserving tunneling of Cooper pairs give rise to highly an anisotropic character to a *s*-wave superconducting gap function and leads to a high value of T_c. More references on ILPT in high-T_c superconductors is available in the thesis by Angilella[214].

The Josephson tunneling of Cooper pairs between two adjacent CuO_2 layers ca be described by a term[148],

$$\mathcal{H}_J = -\sum_{\mathbf{k}} T_J(\mathbf{k}) \left(c^{(1)\dagger}_{\mathbf{k}\uparrow} c^{(1)\dagger}_{-\mathbf{k}\downarrow} c^{(2)}_{-\mathbf{k}\downarrow} c^{(2)}_{\mathbf{k}\uparrow} + h.c \right) \tag{5.1}$$

where $c^{(m)\dagger}_{\mathbf{k}\sigma}$ creates an electron with wave vector $\mathbf{k}$ and spin σ in layer m $(= 1, 2)$. $T_J(\mathbf{k})$ represents the Josephson pair tunneling amplitude which is chosen to be $T_J(\mathbf{k}) = t_\perp(\mathbf{k})^2/t$, where t is the in-plane hopping integral. The single particle interplanar hopping amplitude, $t_\perp(\mathbf{k})$ depends on planar momentum $\mathbf{k}$ as,

$$t_\perp(\mathbf{k}) = \frac{t_\perp}{4} \left[\cos(k_x a) - \cos(k_y a) \right]^2 \tag{5.2}$$

Such a form of $t_\perp(\mathbf{k})$ is supported by band structure calculation and experimental evidences in bilayer cuprates (§1.4). The tunneling Hamiltonian of Eq. (5.1) describes destruction of a Cooper pair in one plane and creation of a pair in the other plane. The process conserves the planar momentum, $\mathbf{k}$ and represents an interaction which is strictly local in $\mathbf{k}$-space. This implies an infinite range pairing interaction in real space and it is believed to have many nontrivial consequences to the properties in the superconducting state including the highly anisotropic gap structure[26].

Regarding the validity of the ILPT model, experiments designed to verify the scenario seem to contradict the notion for certain materials. For example, the *c*-axis penetration depth, which is related to the condensation energy due to the interlayer tunneling, is found to differ in $Tl_2Ba_2CuO_{6+x}$[98, 99] from the value predicted by the ILPT theory by roughly one order of magnitude. However, Chakravarty *et al*[215] have argued that the discrepancy in theory

and experiments in these materials can be brought down drastically by a more careful analysis taking into account the fluctuation effects.

In this work, we directly calculate the energy due to the Josephson pair tunneling term in a bilayer in superconducting state, where each of the layers is described by the Gutzwiller projected *d*-wave BCS wavefunction having variable particle number. Calculations are done using a grand canonical VMC simulation. The results of our calculation show that the energy due to the pair tunneling term is too small to be of any significance at least for parameter values considered. Apart from this result that negates the importance of ILPT in the variational study, this work also demonstrates an algorithm to perform Monte Carlo simulation in a grand canonical scheme.

5.2 The model

The effect of ILPT on the superconducting properties of multilayered systems have been studied by describing individual layers by either a BCS-like effective Hamiltonian[148, 214] or a toy Hamiltonian[213] and then adding a pair-tunneling term between them. Here we consider the two dimensional *t*-*J* model for each of the layers connected by the Josephson tunneling term. Thus we consider a Hamiltonian for a bilayer lattice given by,

$$\begin{aligned}\mathcal{H} = & - t \sum_{m\langle i,j\rangle\sigma} \left(c_{i\sigma}^{(m)\dagger} c_{j\sigma}^{(m)} + h.c. \right) + J \sum_{m\langle i,j\rangle} \left(\mathbf{S}_i^{(m)} . \mathbf{S}_j^{(m)} - \frac{1}{4} n_i^{(m)} n_j^{(m)} \right) \\ & - \sum_{\mathbf{k}} T_J(\mathbf{k}) \left(c_{\mathbf{k}\uparrow}^{(1)\dagger} c_{-\mathbf{k}\downarrow}^{(1)\dagger} c_{-\mathbf{k}\downarrow}^{(2)} c_{\mathbf{k}\uparrow}^{(2)} + h.c. \right) \end{aligned} \tag{5.3}$$

where $c_{i\sigma}^{(m)}$ ($c_{i\sigma}^{(m)\dagger}$) annihilates (creates) an electron of spin σ at site i of layer m ($= 1, 2$), and $n_i^{(m)} = c_{i\sigma}^{(m)\dagger} c_{i\sigma}^{(m)}$. $\mathbf{S}_i^{(m)}$ is the spin operator at site i of layer m. The summation indices $\langle i, j\rangle$ indicate nearest neighbor pairs in a plane and wave vector $\mathbf{k}$ belongs to the first Brillouin zone of a 2D square lattice. The no double occupancy restriction is implicitly assumed. The parameters t and J are the planar hopping and exchange integral, respectively. The pair tunneling amplitude, $T_J(\mathbf{k})$ is taken to be of the form[148],

$$T_J(\mathbf{k}) = \frac{t_\perp^2}{16t} (\cos k_x - \cos k_y)^4 \tag{5.4}$$

with $t_\perp$ being the interplanar single particle hopping parameter. As for the parameter values, estimates for t ($\sim$ 0.4 eV) and J ($\sim$ 0.13 eV) are already mentioned in §3.2. Magnitude of $t_\perp$ is estimated to be of the order of 0.15 eV[148] giving a value of $t_\perp/t$ to be $\sim$ 0.4. Hence, here we consider $t_\perp$ to be $0.4t$. The exchange parameter J is fixed at $0.35t$.

5.3 The variational wavefunction

The Gutzwiller projected BCS wavefunction has proved to be a reasonably good variational wavefunction to describe the superconducting state of the two dimensional t-J and Hubbard models as mentioned before. Traditionally in VMC studies of these models, one consider a variational wavefunction in fixed electron number (N) representation for convenience. This is possible and also justified as these Hamiltonians conserve particle number and average values of observables in canonical and grand canonical scheme are expected to show same qualitative behaviour. However in this case, the pair tunneling term in the Hamiltonian (Eq. (5.3)) destroys or creates two electrons in an individual layer. Therefore it is necessary to incorporate particle number fluctuations in the variational wavefunction. Here we describe the state of individual layers by the Gutzwiller projected BCS wavefunction with variable particle number,

$$|\Psi\rangle^{(m)} = \mathcal{P}_G^{(m)}|\Psi_{BCS}\rangle^{(m)} = \mathcal{P}_G^{(m)}\prod_{\mathbf{k}}\left(u_{\mathbf{k}} + v_{\mathbf{k}}c_{\mathbf{k}\uparrow}^{(m)\dagger}c_{-\mathbf{k}\downarrow}^{(m)\dagger}\right)|0\rangle \tag{5.5}$$

where m ($= 1, 2$) is the layer index. The pairing symmetry of the superconducting state is taken to be the d-wave. Then we consider a product two such wavefunctions, ones for each layer, as the trial wavefunction of the Hamiltonian of Eq. (5.3). Thus our variational wavefunction is given by,

$$|\Psi_{var}\rangle = |\Psi\rangle^{(1)}|\Psi\rangle^{(2)} \tag{5.6}$$

5.4 The method

As the variational wavefunction described above represents a wavefunction with fluctuating particle number, we employ a grand canonical version of the VMC method. First, we represent the Hamiltonian and the wavefunction in real space, as illustrated below.

5.4.1 Hamiltonian in real space

The third term, $\mathcal{H}_3$ of Eq. (5.3) is in k-space. We transform it into real space by using the Fourier transformations,

$$c^{(m)\dagger}_{\mathbf{k}\sigma} = \frac{1}{\sqrt{N_s}} \sum_i e^{-i\mathbf{k}\cdot\mathbf{r}^{(m)}_i} c^{(m)\dagger}_{i\sigma} \quad \text{and} \quad c^{(m)}_{\mathbf{k}\sigma} = \frac{1}{\sqrt{N_s}} \sum_i e^{i\mathbf{k}\cdot\mathbf{r}^{(m)}_i} c^{(m)}_{i\sigma} \tag{5.7}$$

where N_s is the number of lattice sites per layer and $\mathbf{r}^{(m)}_i$ represents a vector in layer m. Thus we get,

$$\begin{aligned} \mathcal{H}_3 &= -\sum_{\mathbf{k}} T_J(\mathbf{k}) \left(c^{(1)\dagger}_{\mathbf{k}\uparrow} c^{(1)\dagger}_{-\mathbf{k}\downarrow} c^{(2)}_{-\mathbf{k}\downarrow} c^{(2)}_{\mathbf{k}\uparrow} + h.c. \right) \\ &= -\sum_{ijpq} \left(T_{ijpq} c^{(1)\dagger}_{i\uparrow} c^{(1)\dagger}_{j\downarrow} c^{(2)}_{p\downarrow} c^{(2)}_{q\uparrow} + T'_{qpji} c^{(2)\dagger}_{q\uparrow} c^{(2)\dagger}_{p\downarrow} c^{(1)}_{j\downarrow} c^{(1)}_{i\uparrow} \right) \end{aligned} \tag{5.8}$$

where the amplitudes T_{ijpq} and T'_{qpji} are given by,

$$T_{ijpq} = \frac{1}{N_s^2} \sum_{\mathbf{k}} T_J(\mathbf{k}) e^{-i\mathbf{k}\cdot(\mathbf{r}^{(1)}_i - \mathbf{r}^{(1)}_j)} e^{-i\mathbf{k}\cdot(\mathbf{r}^{(2)}_p - \mathbf{r}^{(2)}_q)} \tag{5.9}$$

$$T_{qpji} = \frac{1}{N_s^2} \sum_{\mathbf{k}} T_J(\mathbf{k}) e^{-i\mathbf{k}\cdot(\mathbf{r}^{(2)}_q - \mathbf{r}^{(2)}_p)} e^{-i\mathbf{k}\cdot(\mathbf{r}^{(1)}_j - \mathbf{r}^{(1)}_i)} = T^*_{ijpq} = T_{ijpq} \tag{5.10}$$

Since $T_{qpji} = T_{ijpq} = T^*_{ijpq}$, Eq. 5.8 can be written as,

$$\mathcal{H}_3 = -\sum_{ijpq} T_{ijpq} \left(c^{(1)\dagger}_{i\uparrow} c^{(1)\dagger}_{j\downarrow} c^{(2)}_{p\downarrow} c^{(2)}_{q\uparrow} + h.c. \right) \tag{5.11}$$

In numerical simulation, it is advantageous to calculate T_{ijpq} beforehand and store it in memory rather than calculating it on the run, in order to save computational time. On the other hand, T_{ijpq} for all possible combination of the indices is a four dimensional *matrix* of size $N_s \times N_s \times N_s \times N_s$ and hence storing it requires a large amount of computer memory even for a reasonable lattice size. However it is easily recognized that due to the symmetries of T_{ijpq}, many of matrix elements are same and it turns out that we need to store a matrix of size of only $N_s \times N_s$. All other elements can be mapped on to this matrix using the symmetry properties of T.

5.4.2 Wavefunction in real space

In §2.3.1, we described the real space representation of a wavefunction which is same as the individual terms in the product wavefunction of Eq (5.6) except that in the earlier case the wavefunction was projected into a fixed N (electron number) subspace. In this case, though the procedure is similar, we have keep in mind some nontrivial consequence of the particle number variation. To illustrate it, let us concentrate on the grand canonical wavefunction for a single layer as given in Eq (5.5). Dropping the layer indices for the time being, we write it as.

$$\begin{aligned} |\Psi\rangle &= \mathcal{P}_G|\Psi_{BCS}\rangle = \mathcal{P}_G \prod_{\mathbf{k}} \left(u_{\mathbf{k}} + v_{\mathbf{k}} c^\dagger_{\mathbf{k}\uparrow} c^\dagger_{-\mathbf{k}\downarrow}\right)|0\rangle \\ &\equiv \mathcal{P}_G \sum_{N=0,2,\ldots}^{N_s} \frac{1}{(N/2)!}\left(\sum_{\mathbf{k}} \varphi(\mathbf{k}) c^\dagger_{\mathbf{k}\uparrow} c^\dagger_{-\mathbf{k}\downarrow}\right)^{N/2}|0\rangle \\ &= \mathcal{P}_G \sum_{N=0,2,\ldots}^{N_s} |\Psi_{BCS}\rangle_N \end{aligned} \tag{5.12}$$

where $\varphi(\mathbf{k})$ as defined in §2.3.1, is given by

$$\varphi(\mathbf{k}) = \frac{\Delta_{\mathbf{k}}}{(\varepsilon_{\mathbf{k}} - \mu) + \sqrt{(\varepsilon_{\mathbf{k}} - \mu)^2 + \Delta^2_{\mathbf{k}}}} \tag{5.13}$$

The gap function is taken to be $\Delta_{\mathbf{k}} = \Delta(\cos k_y - \cos k_y)$. Each term in the summation over N in Eq. (5.12), i.e. $|\Psi_{BCS}\rangle_N$ represent a BCS state with N (even) electrons. Using the Fourier transformation of Eq. (2.9), we get

$$|\Psi_{BCS}\rangle_N = \frac{1}{(N/2)!}\left(\sum_{ij} \varphi(\mathbf{r}_{i\uparrow} - \mathbf{r}_{j\downarrow}) c^\dagger_{i\uparrow} c^\dagger_{j\downarrow}\right)^{N/2}|0\rangle \tag{5.14}$$

where $\varphi(\mathbf{r})$ as defined in Eq. (2.11), is given by

$$\varphi(\mathbf{r}) = \frac{1}{N_s}\sum_{\mathbf{k}} \varphi(\mathbf{k}) e^{-i\mathbf{k}\cdot\mathbf{r}} \tag{5.15}$$

Here we mention that in the grand canonical formalism, it is necessary to consider the numerical factors, such as $(N/2)!$ and N_s in the above two equations, correctly in the calculations. The next important step is the expand the right hand side of Eq. (5.14) by maintaining correct

order of the electron operators. By doing so, we get

$$\mathcal{P}_G|\Psi_{BCS}\rangle_N = \sum_{R_N} C(R_N)\left(c^\dagger_{i_P\uparrow}c^\dagger_{j_P\downarrow}\ldots c^\dagger_{i_2\uparrow}c^\dagger_{j_2\downarrow}c^\dagger_{i_1\uparrow}c^\dagger_{j_1\downarrow}\right)|0\rangle \tag{5.16}$$

where P $(= N/2)$ is the number of up or down electrons and $C(R_N)$ is a $N/2\times N/2$ determinant given by,

$$C(R_N) = \begin{vmatrix} \varphi(\mathbf{r}_{i_1\uparrow}-\mathbf{r}_{j_1\downarrow}) & \cdots & \varphi(\mathbf{r}_{i_1\uparrow}-\mathbf{r}_{j_P\downarrow}) \\ \vdots & & \vdots \\ \varphi(\mathbf{r}_{i_P\uparrow}-\mathbf{r}_{j_1\downarrow}) & \cdots & \varphi(\mathbf{r}_{i_P\uparrow}-\mathbf{r}_{j_P\downarrow}) \end{vmatrix} \tag{5.17}$$

and the effect of the projection operator, $\mathcal{P}_G$ is taken care of by excluding any configuration in Eq. (5.16) with doubly occupied site. The factor of $\frac{1}{(N/2)!}$ in Eq. (5.14) is canceled by a factor accumulated after rearranging the terms to get Eq. (5.16). Further rearranging the electron operators in Eq. (5.16) to recast it into a slightly different form, we get

$$\begin{aligned} \mathcal{P}_G|\Psi_{BCS}\rangle_N &= \sum_{R_N} C(R_N)(-1)^{1+2+\cdots+(P-1)}\left(c^\dagger_{i_1\uparrow}c^\dagger_{i_2\uparrow}\ldots c^\dagger_{i_P\uparrow}c^\dagger_{j_1\downarrow}c^\dagger_{j_2\downarrow}\ldots c^\dagger_{j_P\downarrow}\right)|0\rangle \\ &= S_N\sum_{R_N} C(R_N)|R_N\rangle \end{aligned} \tag{5.18}$$

where the sign factor, S_N is equal to $(-1)^{1+2+\cdots+(N/2-1)} = (-1)^{N(N-2)/8}$. With this we can write the real space grand canonical BCS wavefunction for a single layer as,

$$|\Psi\rangle = \sum_{N=0,2,\ldots}^{\infty} S_N\left(\sum_{R_N} C(R_N)|R_N\rangle\right) \tag{5.19}$$

Therefore the real space representation of our variational wavefunction of Eq. (5.6) for the bilayer becomes,

$$|\Psi_{var}\rangle = \sum_{N=0,2,\ldots}^{\infty}\sum_{N'=0,2,\ldots}^{\infty} S_N S_{N'}\left(\sum_{R_N^{(1)}}\sum_{R_{N'}^{(2)}} C(R_N^{(1)})C(R_{N'}^{(2)})|R_N^{(1)}\rangle|R_{N'}^{(2)}\rangle\right) \tag{5.20}$$

5.4.3 Grand canonical simulation

Having done the groundwork, the next task is to perform the Monte Carlo simulation of the variational wavefunction. The trial wavefunction defined in Eq. (5.20) is a linear superposition of product states where each term in the product represents a BCS state for a layer with a fixed electron number. In a particular configuration, the number of electrons in the two layers, N and N' may be different. However it is to be noted that because of the presence the Gutzwiller projector, N and N' can vary only upto N_s. The average number of electrons in each layer will be determined by the chemical potential, which we can choose to have same value for both the layers so as to get same average particle density in the two layers. However it turns out that, such a direct simulation of the wavefunction of Eq. (5.20) where particle number can fluctuate, has some nontrivial aspects. It may be mentioned that, a previous simulation of the grand canonical BCS wavefunction was performed by transforming the wavefunction into a mixed band problem[137]. But here we succeed in doing so directly from Eq. (5.20) using an algorithm to be described below. Since the basic problem is of simulating a grand canonical wavefunction in the individual layers, we first focus on the wavefunction for a single layer.

The projected grand canonical BCS wavefunction for a single layer is given in Eq. (5.19). This wavefunction represent a state in the Hilbert space, $\mathbb{H}$ consisting of states with varying number of particles. The expectation value of an observable, $\hat{A}$ is given by

$$\begin{aligned}\langle\hat{A}\rangle &= \frac{\sum_N \sum_{R_N} S_N C(R_N)\langle\Psi|\hat{A}|R_N\rangle}{\sum_N \sum_{R_N} |C(R_N)|^2} \\ &= \sum_N \sum_{R_N} P(R_N)\frac{S_N\langle\Psi|\hat{A}|R_N\rangle}{C^*(R_N)}\end{aligned} \tag{5.21}$$

where

$$P(R_N) = \frac{|C(R_N)|^2}{\sum_N \sum_{R_N} |C(R_N)|^2} \tag{5.22}$$

In Monte Carlo, we can evaluate the sum in Eq. (5.21) by importance sampling over the configurations with respect to their weights, $P(R_N)$. Thus we can write,

$$\langle\hat{A}\rangle \approx \frac{1}{\sum_N M_N} \sum_N \sum_{R_N} \left(\frac{S_N\langle\Psi|\hat{A}|R_N\rangle}{C^*(R_N)}\right) \tag{5.23}$$

where M_N is number of states sampled from an N particle subspace of $\mathbb{H}$. However, the problem in carrying out the Monte Carlo simulation in this case is of obtaining the right distribution of M_N among various fixed N subspaces. This difficulty can be illustrated by comparing with the situation in canonical VMC. In this case, the wavefunction (Eq. (5.18)) consists of superposition of states with a fixed number of particles. The various basis states of the wavefunction differ only in the occupancies of the lattice sites. Therefore starting with one state, we can generate any other state by successively applying any of the following two kinds of Monte Carlo moves. These are (i) a hopping move where an up or down spin is moved to a vacant site or a combination of the hopping move and (ii) an exchange move where two antiparallel spins are exchanged, with the selection of spins and sites all being possibly random. Thus in other words, a random *walk* in the Hilbert space of the fixed N wavefunction, based on these two Monte Carlo moves is ergodic as the walker is able to visit any of the states in the Hilbert space. However, such a walk based on only the above two moves will obviously fail in the grand canonical case. Here, in addition to the above moves, we need to create or destroy electrons from a configuration. Since for our wavefunction, each basis state is defined for an even number of electrons therefore we need to create or destroy electrons in pairs. The question is how often should we create and how often should we destroy a pair?

Let $\mathbb{H}_N$ be the subspace of $\mathbb{H}$ with fixed number of particles, N. The dimension of $\mathbb{H}_N$, that is the total number of configurations with N electrons strongly depend on N and is given by,

$$G_N = \frac{N_s!}{(N_s - N)!\frac{N}{2}!\frac{N}{2}!} \tag{5.24}$$

The quantity G_N is equal to the total number distinct ways in which we can put $N/2$ up electrons, $N/2$ down electrons and $(N_s - N)$ holes in a lattice having N_s sites (no site is to be doubly occupied by electrons). G_N is sharply peaked at a particular N and much smaller at other values. As an example, we show G_N as a function of N for a 8×8 lattice in Fig. 5.1(a). With the creation or destruction of a pair of electrons, the random walker jumps from one subspace to another as indicated in Fig. 5.1(b). Let us call the move in which we either attempt to create or destroy a pair or stay in current subspace, a jumping move. Now we require that, the time which the walker *attempts* to spend in a particular subspace $\mathcal{H}_N$, or the number of attempts the walker makes to jump into subspace $\mathcal{H}_N$, should be proportional to G_N. However the actual time spent may be different as it will be influenced by the weights or coefficients, $C(R_N)$ of the configurations $|R_N\rangle$ of a subspace. In particular if we consider a hypothetical

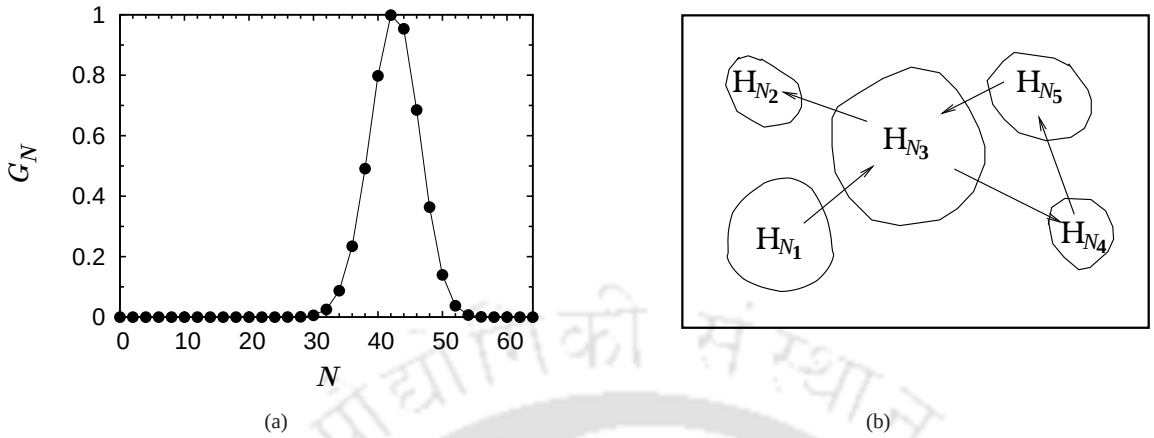

FIGURE 5.1: (a) Dimension, G_N (normalized to unity) of different subspaces $\mathbb{H}_N$ as a function of number of electrons, N for a 8×8 lattice. (b) Schematic representation of a random walk in the grand canonical Hilbert space $\mathbb{H}$ with the arrows indicating jumps of the walker from one fixed N subspace to another with the creation or destruction of electron pairs.

situation where all $|R_N\rangle$ have the same weight, that is, if we consider a wavefunction, $|\Psi_{hyp}\rangle$ such that

$$|\Psi_{hyp}\rangle = \sum_{N=0,2,\ldots}^{Ns} \sum_{R_N} |R_N\rangle \tag{5.25}$$

then we should get, $M_N \propto G_N$, where M_N is as defined in Eq. (5.23). This is an important condition which must be satisfied by the random walker in the grand canonical Hilbert space. The challenge now is to formulate a strategy for random walk which meets the above criterion. In this regard, we propose an algorithm as described below.

We start with an initial random configuration, $|R_N\rangle_i$ of $N/2$ up and $N/2$ down electrons, as usual. To generate other states in the Markovian chain (see §2.3.4) we do a series of Monte Carlo moves as follows. First, we select two distinct sites i and j randomly. The occupants s_i and s_j at these sites may be a hole (0) or an up ($\uparrow$) spin or a down ($\downarrow$) spin. Depending upon the occupant, we attempt a jumping move as follows.

1. If s_i is 0 and s_j is 0: try to create a pair at these two sites (jump from $\mathbb{H}_N \rightarrow \mathbb{H}_{N+2}$).

2. If both s_i and s_j are $\uparrow$: try to destroy one of these with another $\downarrow$ spin chosen randomly (jump from $\mathbb{H}_N \rightarrow \mathbb{H}_{N-2}$).

3. If both s_i and s_j are $\downarrow$: try to destroy one of these with another $\uparrow$ spin chosen randomly (jump from $\mathbb{H}_N \rightarrow \mathbb{H}_{N-2}$).

4. Otherwise: do nothing (stay in $\mathbb{H}_N$)

One such jumping move can be followed by a certain number of hopping and exchange moves as usual. In any of these moves, a new state $|R_{N''}\rangle_{n+1}$ is generated from the current state $|R_{N'}\rangle_n$ with a transition probability, W given by,

$$W(R^n_{N'} \rightarrow R^{n+1}_{N''}) = \min\left\{1, \frac{P(R^{n+1}_{N''})}{P(R^n_{N'})}\right\} \tag{5.26}$$

Here in one Monte Carlo step (MCS), we do one jumping move followed by N_s number of combined hopping and exchange moves. To check whether this algorithm satisfies the condition described in Eq. (5.25), we calculated M_N by taking $C(R_N)$ for all configurations to be equal to unity. The results obtained after giving a run of 10^5 MCS consisting of the above algorithm, is shown alongwith the desired distribution, G_N in Fig. 5.2. The figure shows

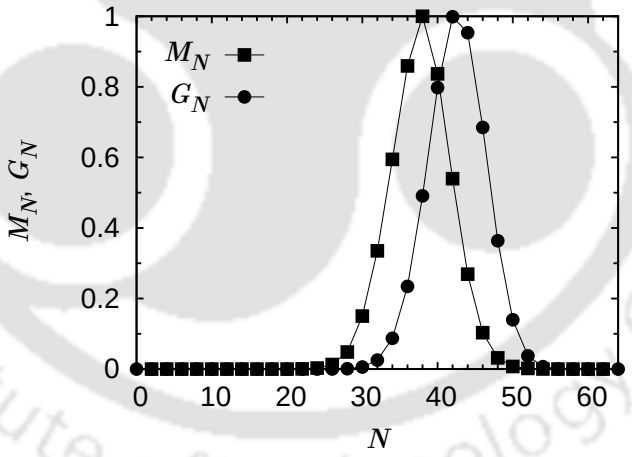

FIGURE 5.2: Normalized values of M_N defined in Eq. (5.23) measured after Monte Carlo simulation of the hypothetical wavefunction of Eq. (5.25) and G_N (see text) as a function of number of electrons N. The results are for a lattice size of 8×8.

that the shapes of the two distribution curves for M_N and G_N are remarkably similar, though their peak positions are slightly different. We found that the simulation based on the above algorithm gives results for the calculated quantities for the actual wavefunction that agree well with those in other studies, as will be shown later. Therefore we go ahead with this algorithm to perform the grand canonical VMC simulation for our purpose here.

5.4.4 Controlling particle density

The average number of particles, $\bar{N}$ in the grand canonical wavefunction determined by the variational parameters μ and $\Delta_{\mathbf{k}}$. Since in our simulation, the particle density is fixed, the variation of μ and Δ is constrained by an implicit equation,

$$\bar{N}(\mu, \Delta) = \text{constant} \tag{5.27}$$

effectively reducing the number of variational parameters to one, which we choose to be Δ. Thus before proceeding for calculations, we must obtain μ as a function of Δ and $\bar{N}$ that satisfies Eq. (5.27). Since inverting Eq. (5.27) analytically is not possible, we have to determine μ only by trial and error method. This requires a search for μ over a wide range of values to obtain the desired μ which would fix the average particle to $\bar{N}$ for a constant Δ. This is inconvenient as the procedure has to be repeated for every change of Δ in a calculation, for example, in wavefunction optimization. However we get around this difficulty by reducing the search for μ to a great extent by using the method of renormalization analysis of Edegger *et al*[116].

The average number of particles in the projected grand canonical BCS wavefunction is given by,

$$\bar{N} = \frac{\langle \Psi_{BCS} | \mathcal{P}_G \hat{N} \mathcal{P}_G | \Psi_{BCS} \rangle}{\langle \Psi_{BCS} | \mathcal{P}_G | \Psi_{BCS} \rangle} \tag{5.28}$$

This number $\bar{N}$ is different from the the average particle number in the unprojected BCS wavefunction because of the projection operator, $\mathcal{P}_G$. However, the effect of projection can be taken into account by renormalizing the unprojected wavefunction and the average number of particles in the projected wavefunction can be made equal to that in an unprojected renormalized wavefunction[216]. This way it can be shown that,

$$\bar{N} \approx 2 \sum_{\mathbf{k}} \frac{g_t^2 |v_{\mathbf{k}}|^2}{u_{\mathbf{k}}|^2 + g_t^2 |v_{\mathbf{k}}|^2} \tag{5.29}$$

where g_t is a renormalization factor given by,

$$g_t = \frac{N_s - \bar{N}}{N_s - N/2} \tag{5.30}$$

The BCS amplitudes $u_{\mathbf{k}}$ and $v_{\mathbf{k}}$ are given by,

$$u_{\mathbf{k}}^2 = \frac{1}{2}\left(1 - \frac{\varepsilon_{\mathbf{k}}}{\sqrt{\Delta_{\mathbf{k}}^2 + (\varepsilon_{\mathbf{k}} - \mu)^2}}\right), \quad v_{\mathbf{k}}^2 = \frac{1}{2}\left(1 + \frac{\varepsilon_{\mathbf{k}}}{\sqrt{\Delta_{\mathbf{k}}^2 + (\varepsilon_{\mathbf{k}} - \mu)^2}}\right), \tag{5.31}$$

where $\varepsilon_{\mathbf{k}}$ is the free electron dispersion. Therefore given a hole density $n = \bar{N}/N_s$ and gap parameter Δ, we can solve Eq. (5.29) numerically for chemical potential, μ. The value of μ can in turn be used in the projected grand canonical BCS wavefunction to get a density close to the desired value in the VMC simulation. While this approach greatly narrows down the search for a desired value of μ and hence reduces computational efforts, it also provides a check for the VMC codes. The chemical potential, obtained after solving the above equation for a particular electron density, should fix the average particle number in the VMC simulation of the grand canonical wavefunction to almost the same value. We carried out this check to test the correctness of our VMC algorithm and found positive result, which will be shown in the following section.

5.4.5 Verification of the algorithm

The first check of our grand canonical VMC algorithm comes through the calculation of particle densities, n as a function of chemical potential, μ. For this purpose we consider the projected grand canonical d-wave BCS wavefunction for the t-J model on a square lattice of size 8×8. Results for n as function of μ and gap parameter Δ for this wavefunction is available from an earlier VMC study by Yokoyama *et al*[137] who used a different formalism for simulation. These results were also compared by Edegger *et al*[216] with their results obtained by the method of renormalization mentioned before. Therefore, we also calculate this quantity by our grand canonical VMC method and compare the results with those obtained in both of these studies. The comparison is shown in Fig. 5.3. It shows that our results for n in Fig. 5.3(a) agree very well with those in Fig. 5.3(b). Especially, the agreement with the VMC results in the second figure is excellent. This gives us an indication that our algorithm for grand canonical VMC simulation is correct. We make a further check on the codes by calculating the energy of the grand canonical BCS wavefunction for the square t-J model using the grand canonical VMC and comparing the results with that for the fixed N wavefunction obtained by using the canonical VMC described earlier. The results for the hopping energy, E_t ($=\langle\mathcal{H}_t\rangle$)

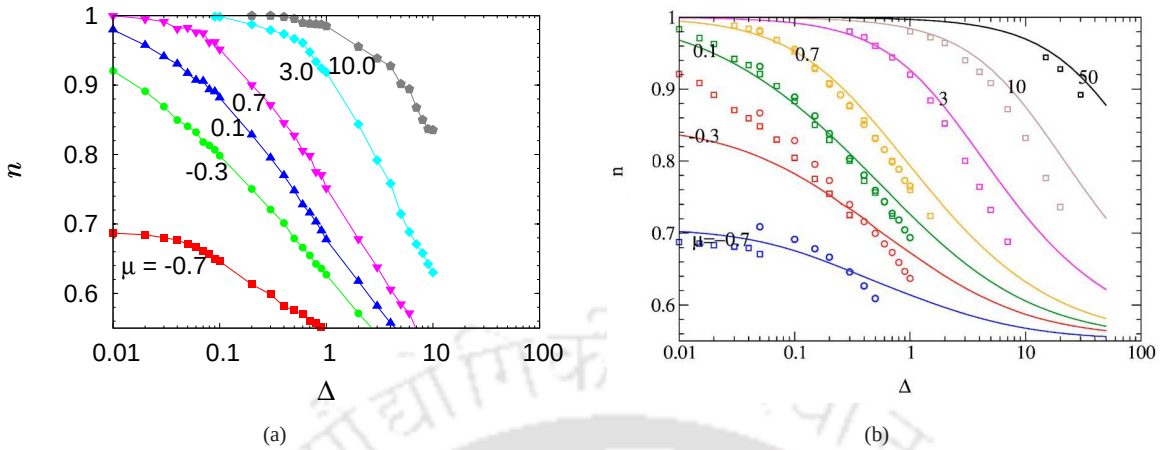

FIGURE 5.3: Particle density, n as a function of gap parameter Δ for the projected grand canonical BCS wavefunction with d-wave symmetry at various chemical potential, μ. (a) Obtained from our grand canonical VMC simulation for a lattice size of 8×8. (b) Obtained by the method of renormalization by Edegger *et al*[216] (solid lines) and by VMC of Yokoyama *et al*[137] (circles for 6×6 lattice) and (squares for 8×8 lattice), taken from Ref. [216].

and exchange energy, E_J ($=\langle \mathcal{H}_J \rangle$) with $\mathcal{H}_t$ and $\mathcal{H}_J$ being the first two terms of Eq. (5.3) for one layer, at various hole densities obtained in the two cases are shown in Fig. 5.4. We see

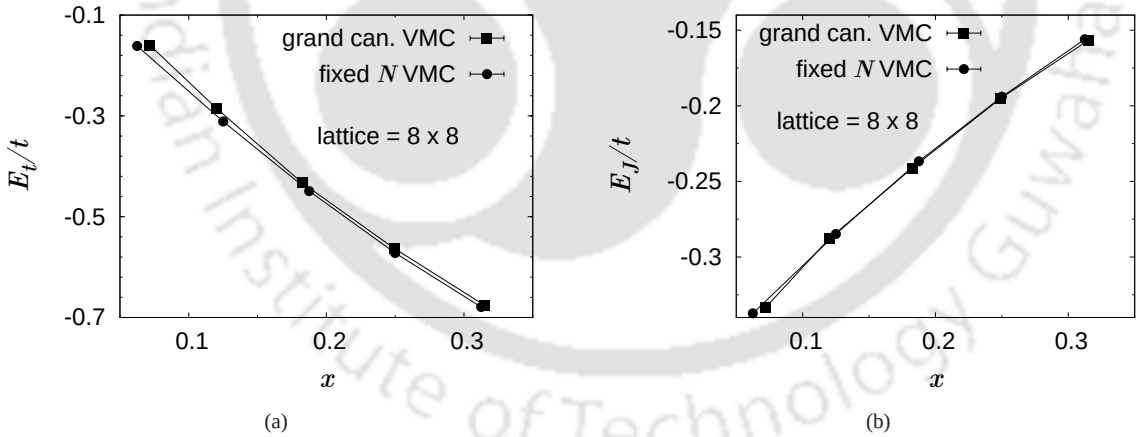

FIGURE 5.4: (a) Hopping energy, E_t/t (per site) and (b) exchange energy, E_J/t (per site) of the d-wave SC state for a square t-J model as a function of hole concentration, x obtained by the grand canonical and fixed N VMC simulation. Exchange constant, $J = 0.35t$.

in the figures that except for the small differences near half-filling, the overall agreement between the two results is excellent. This confirms the correctness of our grand canonical VMC algorithm. Therefore next we go ahead with the calculations for the bilayer for purpose as set out in the beginning.

5.5 Energy due to interlayer pair tunneling

In this section, we shall show the calculation of energies of the various terms in the Hamiltonian of Eq. (5.3) using the grand canonical VMC method. The system that we consider is a bilayer lattice consisting of two square planes which we take to be of size 8×8. As described by the Hamiltonian (Eq. (5.3)), each of the layers is represented by a t-J model and a Josephson pair tunneling term connects the two layers. The variational wavefunction for the bilayer is defined in Eq. (5.6). It consists of a product of two projected BCS wavefunctions with varying particle number, one for each layer. The wavefunction has d-wave pairing symmetry.

The grand canonical VMC formalism used here to simulate the wavefunction is described above in details in the context of a single layer wavefunction. The procedure for the bilayer is similar. We first initiate two random configurations of spins in the two layers. To generate other configurations, we make a series of Monte Carlo moves as follows. First we choose one layer randomly and then attempt a jumping move from that layer. This is followed by N_s (number of sites in a layer) number of hopping and exchange moves in the layer where we stay after the jumping move. One set of such moves is considered as one Monte Carlo sweep (MCS). The inverse update method used earlier (§2.3.5) to update configurations after a move is accepted is employed here also. The chemical potential, μ is chosen to have the same value in both the layers to obtain same average density of particles in the two layers. To calculate the expectation values of observables, we take samples from about 5×10^4 MCS after giving a warm up run of 5000 MCS.

We calculated energy as a function of the variational parameter, Δ at various hole doping. In the calculations, we found that for $t_\perp = 0.4t$, which is the value suggested in Ref. [148] as mentioned earlier, the interlayer pair tunneling energy is numerically negligible. Therefore, here we consider a much greater value, e.g. $t_\perp/t = 1$ in the calculations. The results for the total energy, E (per site in units of t) as a function of Δ for three hole concentrations in three different regimes of hole doping are shown in Fig. 5.5. In the figures for $x = 0.06$ (underdoped) and $x = 0.19$ (optimally doped), we see that E has a minimum with respect to Δ indicating the stability of a d-wave superconducting state in the bilayer. For $x = 0.31$ however, the lowest energy is obtained only for $\Delta \to 0$ which reduces the wavefunction to the normal state. Now let us examine the component of the energy due to interlayer pair tunneling, i.e., $E_\perp (= \langle \mathcal{H}_J \rangle$ where $\mathcal{H}_J$ is the third term of the Hamiltonian of Eq. (5.3)). In Fig. 5.6, we

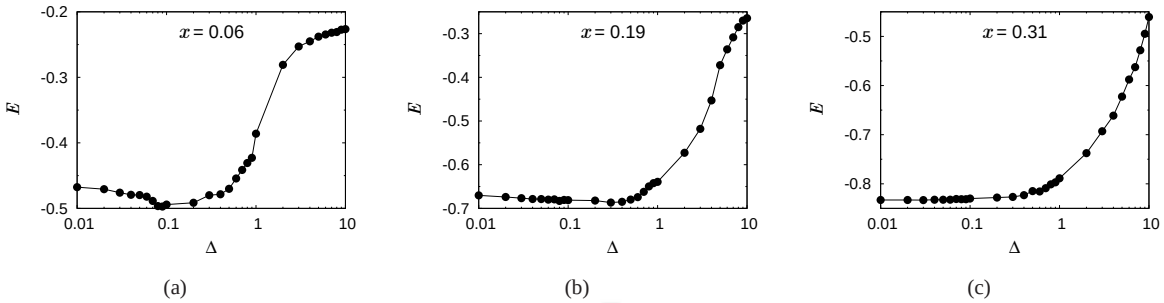

FIGURE 5.5: Total energy, E (per site in units of t) of the wavefunction defined in Eq. (5.6) for a bilayer as a function of the variational parameter, Δ for three values of hole concentrations shown in the figures. Parameter values are $J/t = 0.35$ and $t_\perp/t = 1$ and lattice size is $8\times8\times2$.

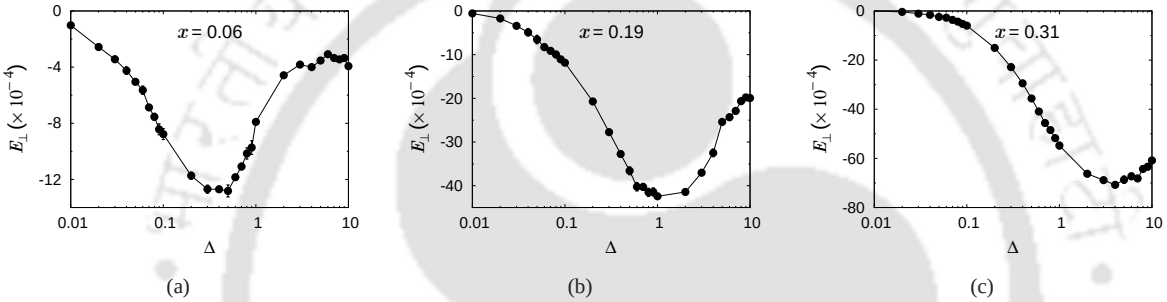

FIGURE 5.6: Energy, $E_\perp$ (per site in units of t) due to the interlayer pair tunneling term in the Hamiltonian of Eq. (5.3) as a function of Δ, for parameter values same as those in Fig. 5.5.

plot $E_\perp$ (per site in units of t) as a function of Δ for same values of x as above. The figures shows that $E_\perp$ is a non-monotonic function of Δ. This is in sharp contrast to the behaviour of the single particle hopping energy or the exchange energy which are monotonically varying function of Δ (as in Fig. 3.7). Moreover, the relative depth of the minima in the $E_\perp$ versus Δ curves are much greater than that for the total energy, E. Another remarkable feature is the behaviour of $\tilde{\Delta}'$, the gap parameter where $E_\perp$ shows a minimum. Comparison of the plots in the above two figures show that the magnitude of $\tilde{\Delta}'$ is much greater than $\tilde{\Delta}$, the optimal gap parameter corresponding to the total energy. This implies that interlayer pair tunneling tends to enhance superconducting pairing in a plane as suggested in the ILPT theory[26]. However, we observe that the lowering of energy by interlayer pair tunneling is very small even for $t_\perp/t = 1$ (see the scale of the vertical axis in Fig. 5.6) as compared to the other energies, which is the most important result here. Because of this small value of $E_\perp$, the pair tunneling term has practically has no effect on $\tilde{\Delta}$. We also calculated the condensation energy, E_c as $E_c = E_n - E_s$, where E_n ($= E$ for $\Delta \to 0$) and E_s ($= E$ for $\Delta = \tilde{\Delta}$) are the energies of the

normal and superconducting states, respectively. We found that at optimal doping ($x = 0.19$), contribution to E_c by the interlayer pair tunneling term (for $t_\perp/t = 1$) is only $\sim$ 10% percent of the total value, in contrast to the opposite scenario suggested in the ILPT theory[26]. The reason for this negligible energy of the pair tunneling term was found to be the following. The magnitudes of the tunneling amplitudes, T_{ijpq} (Eq. (5.9)) are very small. For $t_\perp/t = 1$, typically it ranges from zero to $\sim 10^{-3}$.

5.6 Summary

We have studied the effects of interlayer pair tunneling in a *t*-*J* bilayer by using a grand canonical variational Monte Carlo method. As the variational state, we consider a product wavefunction where each of the layers is described by the projected *d*-wave BCS wavefunction with varying particle number. The algorithm used for the grand canonical VMC simulation is unique which we have developed and described in details. We calculate the energies corresponding to different terms in the Hamiltonian at various hole dopings. We find that though the energy due the Josephson pair tunneling term shows interesting variations with respect to the superconducting gap parameter, its magnitude is too small to have any significant effect on the superconducting properties, including the condensation energy.

Chapter 6

Summary and outlook

Since the discovery of high-T_c superconductivity in the cuprate compounds intense theoretical efforts have been made to understand the strongly correlated electron systems in these materials. The crystal structures of the cuprates consist of stratified CuO_2 layers as the main component of a unit cell. Over the years, theoretical studies on the high-T_c cuprates have focused mainly on a single CuO_2 layer which is believed to carry the essential physics of these materials. However, there also exists a strong interlayer coupling between different CuO_2 planes, especially in multilayered compounds which contain more than one CuO_2 layer per unit cell. For example, the magnetic moments of the copper atoms in two adjacent CuO_2 planes of bilayer compounds, such as $YBa_2Cu_3O_{6+x}$ (YBCO), $Bi_2Sr_2CaCu_2O_{8+x}$ (Bi2212) etc., are found to be connected by an antiferromagnetic exchange coupling whose strength is nearly 10% of that between the copper spins in a plane. The bilayer splitting clearly observed in the recent ARPES experiments in bilayer cuprates implies that there exists a coherent single particle hopping in the superconducting state across the CuO_2 planes. The interlayer couplings between different CuO_2 layers have profound implications to the physical properties of the cuprate superconductors. It gives rise to a much higher superconducting transition temperature, T_c in multilayered cuprates in addition to some subtle differences in magnetic and other electronic properties. However the precise mechanism how interlayer coupling affects the physical properties is currently not well understood.

In this thesis, we have studied the superconducting and magnetic properties of bilayer superconductors and examined the effects of interlayer couplings on the properties. Each of the layers is described by a two dimensional t-J model. Interlayer couplings are provided by an

interplanar single particle hopping and an interplanar exchange coupling term. The resulting Hamiltonian is studied using the variational Monte Carlo (VMC) method which is a powerful numerical numerical technique to obtain the ground state properties in presence of strong correlations. We developed the numerical code for VMC and tested it rigorously for correctness. The method is described in details. These form the subject of chapter 2. We also included a brief study on the effects of nonmagnetic impurity doping on the magnetic properties of copper oxide layer and ladder materials. The physical systems were modeled by a strong coupling Hubbard model with an additional potential term representing the impurities. The resulting Hamiltonian is studied using the finite temperature quantum Monte Carlo (FTQMC) method, the code for which are also developed by us independently. We observed interesting effects, such as, enhancement of antiferromagnetic (AF) correlations around an impurity, destruction of AF long range order (AFLRO) by finite concentration of impurities etc. For ladder, the uniform magnetic susceptibility as a function of temperature for the doped system shows a sharp increase at lower temperatures, a feature not seen in pure ladders. We examined the interplay of holes and impurities away from half-filling but found no evidence of any impurity effect on hole mobility.

The momentum dependence of the superconducting gap has been one of the major issues in the high-T_c superconductors. In general, the gap function is found to be of $d_{x^2-y^2}$-wave symmetry from angle resolved photoemission spectroscopy (ARPES) and tunneling experiments. Various analytical and numerical studies of the two dimensional t-J and Hubbard models over the years have shown that these models strongly support the scenario. However, there also exists a number of experimental evidences, especially in bilayer materials, which suggest that the gap symmetry is more complex than a simple d-wave. We examined this issue in chapter 3. We considered several pairing symmetries of the superconducting state for a t-J bilayer by taking the Hamiltonian parameter values that are suggested to be appropriate for bilayer cuprates by experiments. Our variational calculations show that for the physical range of Hamiltonian parameter values, the d-wave state yield the lowest energy in the bilayer as in single layered systems. The interplay of antiferromagnetism and superconductivity has always been an important issue in the study of cuprate superconductors owing to their proximity in the phase diagram. We have investigated the issue of coexistence in bilayers and found that antiferromagnetism coexists with superconductivity in the underdoped regime, a scenario also observed in the two dimensional t-J model. Interestingly we observed that in

the coexisting state, both the AF and SC correlations are significantly enhanced as compared to those in pure superconducting state.

In chapter 4, we obtained a ground state phase diagram for t-J bilayer as a function the interlayer coupling strengths and hole concentration for fixed values of planar parameters. The phase diagram shows rich features, such as a coexistence of antiferromagnetism and superconductivity at underdoping, competing planar and interplanar superconducting correlations for moderate and strong interlayer exchange coupling etc. Another interesting feature in the phase diagram is a non-monotonic variation of the phase boundary between the superconducting and normal phases as a function of interlayer hopping parameter. While larger single particle interlayer hopping enhances the magnitude of d-wave SC gap at underdoping, it is found to have the opposite effect on SC correlations. The single electron interlayer hopping reduces the SC correlations at all doping levels, except for in the overdoped region where pairing correlations are enhanced for moderate values of the parameter. Increasing strength of interlayer exchange coupling changes the nature of the SC state from being predominantly planar to a state having strong interplanar pairing. The magnetic correlations at and near half-filling are found to show three dimensional AF long range order (AFLRO). The magnetic correlations are affected negligibly by interlayer couplings. Instead, the holes are found to be much more effective in destroying the AFLRO.

The interlayer pair tunneling (ILPT) has been believed to play an important role in the development of the superconducting state in high-T_c cuprates. It has been suggested that in the superconducting state Cooper pairs tunnel across the CuO_2 layers coherently thereby lowering the kinetic energy substantially. This interlayer pair tunneling amplifies superconductivity in the plane and provides almost all of the large condensation energy observed in the cuprate superconductors. However experimental test of the above scenario in a number of compounds contradicts the picture. Here we examined the issue using a grand canonical VMC method based on a new algorithm. Specifically, we calculated the energy due to the Josephson tunneling of Cooper pairs across the layers. This is the content of chapter 5. We described the superconducting state of the bilayer by a variational wavefunction which consists of product of two Gutzwiller projected d-wave BCS wavefunctions with varying particle number, one for each layer. The wavefunction is simulated using our grand canonical VMC method which is described in details. Calculation of energies show that though the energy due the interlayer

pair tunneling shows interesting variations with respect to the superconducting gap parameter, its magnitude is too small to have any significant effect on the superconducting properties, including the condensation energy.

Finally, a few concluding remarks are in order. In this work, we have attempted to understand how interlayer couplings effect the superconducting and magnetic properties of bilayer superconductors. Since the variational method used here is mainly limited to studying only the ground state properties, rigorous comparison of our results with experiments could not be made. As for the possible extension of the work, it can be pursued in various directions. First we can consider a more realistic model Hamiltonian for bilayer superconductors than the basic bilayer *t*-*J* model considered here. To cite an example, we can include the next nearest neighbour hopping in the Hamiltonian which is shown to be necessary to explain some of the observed ARPES features of the cuprates. Also, the interlayer hopping parameter, $t_\perp$ is taken here to be independent of the planar momentum, **k**. However, in view of the observed anisotropy in the magnitude of band splitting in bilayer superconductors, it is desirable to take a **k**-dependent form of $t_\perp$ as suggested by the experiments. As for the nature of the superconducting state in bilayer, a few more possible pairing symmetries than the ones considered here can be explored. Another interesting prospect would be to extend the variational Monte Carlo method to excited states and study the finite temperature properties of bilayer superconductors.

Appendix A

The finite temperature Quantum Monte Carlo method

A.1 Grand canonical ensemble average

The basic idea in finite temperature Quantum Monte Carlo (FTQMC) method[182, 217] is to simulate the grand canonical ensemble of a system. The grand canonical expectation value of an observable, O is given by,

$$\langle O \rangle = \frac{Tr\left(Oe^{-\beta H}\right)}{\mathcal{Z}} \tag{A.1}$$

where $\beta = 1/kT$, $\mathcal{H}$ is the Hamiltonian of the system. Tr stands for sum over all particle numbers and over all site occupancies. $\mathcal{Z}$ is the grand canonical partition function defined as,

$$\mathcal{Z} = Tr\left(e^{-\beta H}\right) \tag{A.2}$$

The Hamiltonian for the Hubbard model is given by,

$$\mathcal{H} = -t \sum_{\langle ij \rangle, \sigma} \left(c^{\dagger}_{i\sigma} c_{j\sigma} + h.c.\right) + U \sum_{i} n_{i\uparrow} n_{j\downarrow} - \mu \sum_{i\sigma} n_{i\sigma} \tag{A.3}$$

where the meaning of the terms are as described in Chapter 2.

A.2 Trotter decomposition

To perform numerical simulation, we have to first carry out the trace over fermionic degrees of freedom in Eq. (A.1). To achieve this, we discretize the imaginary time, β into small steps by writing $\beta = \Delta\tau L$. The partition function now can be written as

$$\mathcal{Z} = Tr\left(e^{-\Delta\tau LH}\right) = Tr\left(e^{-\Delta\tau(K+V)}\right)^L \tag{A.4}$$

with K and V being

$$K = -t\sum_{\langle ij\rangle,\sigma}\left(c^\dagger_{i\sigma}c_{j\sigma} + h.c.\right) - \mu\sum_{i\sigma} n_{i\sigma} \tag{A.5}$$

$$V = U\sum_i n_{i\uparrow}n_{j\downarrow} \tag{A.6}$$

Now different terms in the exponential in Eq. (A.4) are separated using the Suzuki-Trotter decomposition formula[218],

$$e^{-\Delta\tau(K+V)} \cong e^{-\Delta\tau K}e^{-\Delta\tau V} \tag{A.7}$$

so that the partition function becomes

$$\mathcal{Z} \cong Tr\left(e^{-\Delta\tau K}e^{-\Delta\tau V}\right)^L \tag{A.8}$$

A.3 Hubbard-Stratonovich transformation

The interaction term $e^{-\Delta\tau V}$ is quartic in electron operators. This term is made quadratic by using the discrete Hubbard-Stratonovich transformation[219] as follows. Since $n^2_{i\sigma} = n_{i\sigma}$, we can write

$$n_{i\uparrow}n_{i\downarrow} = -\frac{1}{2}m_i^2 + \frac{1}{2}n_i \tag{A.9}$$

where $m_i = (n_{i\uparrow} - n_{i\downarrow})$ and $n_i = (n_{i\uparrow} + n_{i\downarrow})$ are local magnetization and charge, respectively. Therefore we get

$$\begin{aligned} e^{-\Delta\tau V} &= e^{-\Delta\tau U \sum_i \left(-\frac{1}{2}m_i^2 + \frac{1}{2}n_i\right)} \\ &= \prod_i e^{-\frac{U\Delta\tau}{2}n_i} e^{\frac{U\Delta\tau}{2}m_i^2} \end{aligned} \tag{A.10}$$

By the Hubbard-Stratonovich transformation,

$$e^{\frac{U\Delta\tau}{2}m_i^2} = \frac{1}{2}\sum_{s_i=\pm 1} e^{-s_i\lambda m_i} \tag{A.11}$$

where $\cosh\lambda = e^{U\Delta\tau}/2$. U is regarded to be positive here.

A.4 Trace over fermionic degrees of freedom

Using the above the $e^{-\Delta\tau V}$ term can be written as,

$$\begin{aligned} e^{-\Delta\tau V} &= \prod_i e^{-\frac{U\Delta\tau}{2}n_i} \frac{1}{2}\sum_{s_i=\pm 1} e^{-s_i\lambda m_i} \\ &= \prod_i \left[\frac{1}{2}\sum_{s_i=\pm 1}\prod_\sigma e^{-\left(\sigma s_i\lambda + \frac{U\Delta\tau}{2}\right)n_{i\sigma}}\right] \\ &= \left(\frac{1}{2}\right)^{N_s}\sum_{s_1}\sum_{s_2}\cdots\prod_\sigma e^{-\sum_i\left(\sigma s_i\lambda + \frac{U\Delta\tau}{2}\right)n_{i\sigma}} \\ &= \left(\frac{1}{2}\right)^{N_s} Tr_{\{s\}}\left[\prod_\sigma e^{-\sum_i\left(\sigma s_i\lambda + \frac{U\Delta\tau}{2}\right)n_{i\sigma}}\right] \end{aligned} \tag{A.12}$$

In the above, $\sigma = +\ (-)$ for spin $\uparrow$ ($\downarrow$) and N_s is the number of lattice sites. Now the $e^{-\Delta\tau K}$ term is written as,

$$\begin{aligned} e^{-\Delta\tau K} &= e^{\Delta\tau t\sum_{\langle ij\rangle\sigma}\left(c_{i\sigma}^\dagger c_{j\sigma} + h.c.\right) + \Delta\tau\mu\sum_{i\sigma} n_{i\sigma}} \\ &= \prod_\sigma \left(e^{-\Delta\tau\sum_{ij} c_{i\sigma}^\dagger K_{ij} c_{j\sigma}}\right)\left(e^{\Delta\tau\mu\sum_{i\sigma} n_{i\sigma}}\right) \end{aligned} \tag{A.13}$$

The two exponential terms can be separated because they commute. $K_{ij} = -t$ for i, j nearest neighbour and is 0 otherwise. Therefore

$$\begin{aligned} e^{-\Delta\tau K}e^{-\Delta\tau V} &= \left(\prod_{\sigma} e^{-\Delta\tau\sum_{ij}c^{\dagger}_{i\sigma}K_{ij}c_{j\sigma}}e^{\Delta\tau\mu\sum_{i\sigma}n_{i\sigma}}\right)\left(\left(\frac{1}{2}\right)^{N_s}\underset{\{s\}}{Tr}\prod_{\sigma}e^{-\sum_i\left(\sigma s_i\lambda+\frac{U\Delta\tau}{2}\right)n_{i\sigma}}\right) \\ &= \left(\frac{1}{2}\right)^{N_s}\underset{\{s\}}{Tr}\left(\prod_{\sigma}e^{-\Delta\tau\sum_{ij}c^{\dagger}_{i\sigma}K_{ij}c_{j\sigma}}e^{-\Delta\tau\sum_i c^{\dagger}_{i\sigma}V^{\sigma}_i c_{j\sigma}}\right) \end{aligned} \tag{A.14}$$

We have divided the whole imaginary time interval $(0,\beta)$ into small slices each of width Δ. If we consider the above term to be for the l-th time slice ($l = 1, 2, \ldots, L$), then the Hubbard-Stratonovich (HS) variables s_i as well as V_i^{σ} acquires a time index l. Thus $V_i^{\sigma}(l)$ is given by,

$$V_i^{\sigma}(l) = \frac{\sigma\lambda s_i(l)}{\Delta\tau} + \left(\frac{U}{2} - \mu\right) \tag{A.15}$$

Next we write,

$$\left(e^{-\Delta\tau K}e^{-\Delta\tau V}\right)^L = \prod_{l=L}^{1}\left(e^{-\Delta\tau K}e^{-\Delta\tau V}\right) \tag{A.16}$$

so that earlier times appear to the right. The partition function now becomes

$$\begin{aligned} \mathcal{Z} &\cong Tr\left(e^{-\Delta\tau K}e^{-\Delta\tau V}\right)^L \\ &= \left(\frac{1}{2}\right)^{N_sL}\underset{\{s\}}{Tr}\prod_{\sigma}Tr\left(\prod_{l}e^{-\Delta\tau\sum_{ij}c^{\dagger}_{i\sigma}K_{ij}c_{j\sigma}}e^{-\Delta\tau\sum_i c^{\dagger}_{i\sigma}V^{\sigma}_i c_{j\sigma}}\right) \end{aligned} \tag{A.17}$$

The trace over fermionic degrees of freedom of the term inside parenthesis can be shown to be equal to $\det\left[I + B_L^{\sigma}B_{L-1}^{\sigma}\ldots B_1^{\sigma}\right]$. Thus

$$\mathcal{Z} \cong \left(\frac{1}{2}\right)^{N_sL}\underset{\{s\}}{Tr}\prod_{\sigma}\det\left[I + B_L^{\sigma}B_{L-1}^{\sigma}\ldots B_1^{\sigma}\right] \tag{A.18}$$

The matrices B_l^{σ} are give by

$$B_l^{\sigma} = e^{-\Delta\tau K}e^{-\Delta\tau V^{\sigma}(l)} \tag{A.19}$$

with K and $V^{\sigma}(l)$ being the $N_s \times N_s$ matrices

$$K = \begin{pmatrix} 0 & -t & 0 & \cdots & 0 & -t \\ -t & 0 & -t & \cdots & 0 & 0 \\ 0 & -t & 0 & \cdots & 0 & 0 \\ \vdots & & & & & \vdots \\ -t & 0 & 0 & \cdots & -t & 0 \end{pmatrix} \tag{A.20}$$

$$V^{\sigma}(l) = \begin{pmatrix} d_1^{\sigma}(l) & 0 & \cdots & 0 \\ 0 & d_2^{\sigma}(l) & \cdots & 0 \\ \vdots & & & \vdots \\ 0 & 0 & \cdots & d_{N_s}^{\sigma}(l) \end{pmatrix} \tag{A.21}$$

where the diagonal elements are given by $d_i^{\sigma}(l) = \frac{1}{\Delta\tau}\lambda\sigma s_i(l) + \left(\frac{U}{2} - \mu\right)$. Introducing

$$O^{\sigma}(\{s\}) = [I + B_L^{\sigma} B_{L-1}^{\sigma} \ldots B_1^{\sigma}] \tag{A.22}$$

we get

$$\begin{aligned} \mathcal{Z} &\cong \left(\frac{1}{2}\right)^{N_s L} \underset{\{s\}}{Tr}\left[\det O^{\uparrow}(\{s\})\, O^{\downarrow}(\{s\})\right] \\ &= \underset{\{s\}}{Tr}\left[\rho(\{s\})\right] \end{aligned} \tag{A.23}$$

where

$$\rho(\{s\}) = \left(\frac{1}{2}\right)^{N_s L} \left[\det O^{\uparrow}(\{s\})\, O^{\downarrow}(\{s\})\right] \tag{A.24}$$

is called the effective density matrix.

A.5 Calculation of expectation values

Using Eq. (A.17), the equal-time correlation function of two operators A and B is written as

$$\langle AB\rangle = \frac{1}{\mathcal{Z}}\underset{\{s\}}{Tr}Tr\left[AB\prod_{l\sigma}e^{-\Delta\tau\sum_{ij}c^{\dagger}_{i\sigma}K_{ij}c_{j\sigma}}e^{-\Delta\tau\sum_{i}c^{\dagger}_{i\sigma}V^{\sigma}_{i}c_{j\sigma}}\right] \tag{A.25}$$

Defining the fermion average or Green's function for a given configuration of HS fields as,

$$\langle AB\rangle_{\{s\}} \equiv \frac{1}{\rho(\{s\})}Tr\left[AB\prod_{l\sigma}e^{-\Delta\tau\sum_{ij}c^{\dagger}_{i\sigma}K_{ij}c_{j\sigma}}e^{-\Delta\tau\sum_{i}c^{\dagger}_{i\sigma}V^{\sigma}_{i}c_{j\sigma}}\right] \tag{A.26}$$

the correlation function becomes

$$\langle AB\rangle = \frac{1}{\mathcal{Z}}\underset{\{s\}}{Tr}\langle AB\rangle_{\{s\}}\rho(\{s\}) \tag{A.27}$$

Therefore the correlation functions are obtained by sampling the corresponding Green's functions over the HS spin configurations weighted by $\rho(\{s\})$. The algorithm for the simulation is described in great details elsewhere[182, 183, 220]. Here we mention a few technical points. The problem that plagues the method is that the weight factors $\rho(\{s\})$ becomes negative in certain cases, especially away from half-filling, which makes calculations impractical. This is called the negative sign problem in the method.

The equal-time single-particle Green's function $\langle c_{i\sigma}(l)c^{\dagger}_{j\sigma}(l)\rangle_{\{s\}}$ plays a very important role in the Monte Carlo updating process as well as in calculation of expectation values of other observables. This quantity can be shown to be equal to

$$\langle c_{i\sigma}(l)c^{\dagger}_{j\sigma}(l)\rangle_{\{s\}} = [g^{\sigma}(l)]_{ij} = [I + A^{\sigma}(l)]^{-1} \tag{A.28}$$

where $A^{\sigma}(l) = B^{\sigma}_{l-1}B^{\sigma}_{l-2}\ldots B^{\sigma}_{1}B^{\sigma}_{L}\ldots B^{\sigma}_{l}$. We note that the Green's function matrix, $g^{\sigma}(l)$ is obtained from the inverse of another matrix, $[I + A^{\sigma}(l)]$. This matrix is often very ill conditioned, especially at low temperature or high β. Therefore straightforward calculation of $g^{\sigma}(l)$ becomes unstable at low temperature ($\beta t > 3$) and larger U ($> 4t$). The problem is overcome to a large extend by employing an elaborate technique for computation of $g^{\sigma}(l)$, called the method of matrix decomposition[182, 220].

In addition to the equal-time Green's function, $g^{\sigma}(l)$ we also define unequal-time Green's function, $G^{\sigma}(l_1, l_2)$ for $l_1 > l_2$ as $G^{\sigma}_{ij}(l_1, l_2) = \langle c_{i\sigma}(l_1) c^{\dagger}_{i\sigma}(l_2) \rangle_{\{s\}}$. $G^{\sigma}(l_1, l_2)$ can be expressed in terms of the single-particle Green's function as,

$$G^{\sigma}(l_1, l_2) = B^{\sigma}_{l_1} B^{\sigma}_{l_1-1} \ldots B^{\sigma}_{1} B^{\sigma}_{2} \ldots B^{\sigma}_{l_2+1} g^{\sigma}(l_2 + 1) \tag{A.29}$$

We note that both the quantities $g^{\sigma}_{ij}(l)$ and $G^{\sigma}_{ij}(l_1, l_2)$ correspond to a particular configuration of HS fields $\{s\}$. The averages of these quantities over the HS configurations as in Eq. (A.27) give the final expectation values which we denote as $\langle\langle g^{\sigma}_{ij}(l) \rangle\rangle$ and $\langle\langle G^{\sigma}_{ij}(l_1, l_2) \rangle\rangle$. In Monte Carlo, the average is calculated by importance sampling over the N_a configurations according to their weights $\rho(\{s\})$, to get

$$\langle\langle g^{\sigma}_{ij}(l) \rangle\rangle \approx \frac{1}{N_a} \sum_{\zeta=1}^{N_a} g^{\sigma}_{ij}(l) \tag{A.30}$$

and so on. Here ζ represents a configuration, $\{s\}$ of HS field variables.

The expectation value of other quantities can be expressed in terms of these two averages. For example, let us consider a few quantities of common interest. The occupation, n_i at site i is given by, $n_i = \sum_{\sigma} \langle c^{\dagger}_{i\sigma} c_{i\sigma} \rangle$. However in this formalism, each $c_{i\sigma}$ operator has a time index l. In other words we have a space-time lattice of dimension $(N \times N) \times L$. If the lattice has translational symmetry, average occupation at any site is obtained as,

$$\begin{aligned} n &= \frac{1}{N_s L} \sum_{i,l} \sum_{\sigma} \left\langle c^{\dagger}_{i\sigma}(l) c_{i\sigma}(l) \right\rangle \\ &= \frac{1}{N_s L} \sum_{i,l} \sum_{\sigma} \langle\langle \tilde{g}^{\sigma}_{ii}(l) \rangle\rangle \end{aligned} \tag{A.31}$$

where $\tilde{g}^{\sigma}(l) = 1 - g^{\sigma}(l)$. The spin-spin correlation function is $\langle \mathbf{S}_i . \mathbf{S}_j \rangle = (\langle m^x_i m^x_j \rangle + \langle m^y_i m^y_j \rangle + \langle m^z_i m^z_j \rangle)/2$, where $m^x_i = c^{\dagger}_{i\uparrow} c_{i\downarrow} + c^{\dagger}_{i\downarrow} c_{i\uparrow}$, $m^y_i = -i(c^{\dagger}_{i\uparrow} c_{i\downarrow} - c^{\dagger}_{i\downarrow} c_{i\uparrow})$ and $m^z_i = n_{i\uparrow} - n_{i\downarrow}$. Using the Wick's theorem,

$$\langle c^{\dagger}_{i_1} c_{i_2} c^{\dagger}_{i_3} c_{i_4} \rangle_{\{s\}} = \langle c^{\dagger}_{i_1} c_{i_2} \rangle_{\{s\}} \langle c^{\dagger}_{i_3} c_{i_4} \rangle_{\{s\}} + \langle c^{\dagger}_{i_1} c_{i_4} \rangle_{\{s\}} \langle c_{i_2} c^{\dagger}_{i_3} \rangle_{\{s\}} \tag{A.32}$$

each component of the spin-spin correlation function can be expressed as,

$$\langle m_i^x m_j^x \rangle = \langle m_i^y m_j^y \rangle = \left\langle\left\langle \tilde{g}_{ji}^{\uparrow} g_{ij}^{\downarrow} + \tilde{g}_{ji}^{\downarrow} g_{ij}^{\uparrow} \right\rangle\right\rangle \tag{A.33}$$

$$\langle m_i^z m_j^z \rangle = \left\langle\left\langle \tilde{g}_{ii}^{\uparrow}\tilde{g}_{jj}^{\uparrow} + \tilde{g}_{ji}^{\uparrow} g_{ij}^{\uparrow} - \tilde{g}_{ii}^{\uparrow}\tilde{g}_{jj}^{\downarrow} - \tilde{g}_{ii}^{\downarrow}\tilde{g}_{jj}^{\uparrow} + \tilde{g}_{ii}^{\downarrow}\tilde{g}_{jj}^{\downarrow} + \tilde{g}_{ji}^{\downarrow} g_{ij}^{\downarrow} \right\rangle\right\rangle \tag{A.34}$$

Finally the spin susceptibility is defined as,

$$\chi(\mathbf{q}) = \frac{1}{N_s} \sum_{ij} e^{-i\mathbf{q}.(\mathbf{r}_i - \mathbf{r}_j)} \int_0^{\beta} d\tau \left\langle \mathbf{S}_i(\tau)\mathbf{S}_j(0) \right\rangle \tag{A.35}$$

In the discrete time formulation here, the integral is replaced by a sum over the different imaginary time intervals. The unequal-time correlation function is expressed in terms of the unequal-time Green's function. For example, the z-component of the correlation function can be written as,

$$\left\langle m_i^z(l_1) m_j^z(l_2) \right\rangle = \sum_{\sigma\sigma'} \left[(2\delta_{\sigma\sigma'} - 1) \left\langle\left\langle \tilde{g}_{ii}^{\sigma}(l_1)\tilde{g}_{jj}^{\sigma'}(l_2) \right\rangle\right\rangle + \delta_{\sigma\sigma'} \left\langle\left\langle \tilde{G}_{ji}^{\sigma}(l_1, l_2) G_{ij}^{\sigma}(l_1, l_2) \right\rangle\right\rangle \right] \tag{A.36}$$

Other quantities are expressed in terms of the Green's function in a similar way.

Appendix B

Variational wavefunction with coexisting AF and SC order

B.1 AF mean-field decoupling of the bilayer t-J model

Let us consider the t-J Hamiltonian given by,

$$\mathcal{H} = -t \sum_{\langle i,j\rangle\sigma} \left(c^{\dagger}_{i\sigma} c_{j\sigma} + h.c. \right) + J \sum_{\langle i,j\rangle} \mathbf{S}_i \cdot \mathbf{S}_j \tag{B.1}$$

for a three dimensional cubic lattice with A and B being the two sublattices. Here t is the hopping integral and J is exchange constant. $c_{i\sigma}$ ($c^{\dagger}_{i\sigma}$) annihilates (creates) an electron of spin σ at site i. $\mathbf{S}_i$ is the spin operator at site i. The summation indices $\langle i, j\rangle$ indicate sum over nearest neighbours. The Hamiltonian act on a subspace of no doubly occupied sites.

The exchange part of the Hamiltonian can be decoupled by using the identity

$$\hat{P}\hat{Q} \cong \langle \hat{P} \rangle \hat{Q} + \langle \hat{Q} \rangle \hat{P} - \langle \hat{P} \rangle \langle \hat{Q} \rangle \tag{B.2}$$

For antiferromagnetically (AF) ordered ground state, we write

$$\begin{aligned} \langle S_i^x \rangle &= \langle S_i^y \rangle = 0 \qquad \text{(B.3)} \\ \langle S_i^z \rangle &= +m \quad \text{if} \quad i \in A \\ &= -m \quad \text{if} \quad i \in B \\ \text{Or} \quad \langle S_i^z \rangle &= m e^{i\mathbf{Q}\cdot\mathbf{r}_i}, \quad \mathbf{Q} = (\pi, \pi, \pi) \qquad \text{(B.4)} \end{aligned}$$

where $m \geq 0$ and A, B represent the two sub lattices. Thus

$$\begin{aligned} J \sum_{\langle i,j \rangle} \mathbf{S}_i \cdot \mathbf{S}_j &= J \sum_{\langle i,j \rangle} \left(\langle S_i^z \rangle S_j^z + \langle S_j^z \rangle S_i^z - \langle S_j^z \rangle \langle S_i^z \rangle \right) \\ &= Jm \sum_{\langle i,j \rangle} \left(e^{i\mathbf{Q}\cdot\mathbf{r}_i} S_j^z + e^{i\mathbf{Q}\cdot\mathbf{r}_j} S_i^z \right) - J \sum_{\langle i,j \rangle} \langle S_i^z \rangle \langle S_j^z \rangle \\ &= 2Jm \sum_{\langle i,j \rangle} e^{i\mathbf{Q}\cdot\mathbf{r}_j} S_i^z - \frac{1}{2} Jm^2 z N_s \qquad \text{(B.5)} \end{aligned}$$

Here N_s is the number of lattice sites and z is the coordination number of each site. We can write

$$\sum_{\langle i,j \rangle} e^{i\mathbf{Q}\cdot\mathbf{r}_j} S_i^z = \frac{1}{2} \sum_i \sum_{\delta_i} e^{i\mathbf{Q}\cdot\delta_i} e^{i\mathbf{Q}\cdot\mathbf{r}_i} S_i^z = -D \sum_i e^{i\mathbf{Q}\cdot\mathbf{r}_i} S_i^z \qquad \text{(B.6)}$$

where δ_i is a vector connecting site i to its nearest neighbours, D $(= z/2)$ is the dimension of the lattice. Thus the mean-field Hamiltonian up to a constant term becomes

$$\mathcal{H}_{MF} = -t \sum_{\langle i,j \rangle \sigma} \left(c_{i\sigma}^\dagger c_{j\sigma} + h.c. \right) - \Delta_{AF} \sum_i e^{i\mathbf{Q}\cdot\mathbf{r}_i} S_i^z \qquad \text{(B.7)}$$

where $\Delta_{AF} = 2JmD \geq 0$. Fourier transforming the electron operators, we get

$$\mathcal{H}_{MF} = \sum_{\mathbf{k}\sigma} \epsilon_{\mathbf{k}} c_{\mathbf{k}\sigma}^\dagger c_{\mathbf{k}\sigma} - \Delta_{AF} \sum_{\mathbf{k}\sigma} \eta(\sigma) c_{\mathbf{k}+\mathbf{Q}\sigma}^\dagger c_{\mathbf{k}\sigma} \qquad \text{(B.8)}$$

where $\eta(\sigma) = +1, -1$ for $\sigma = \uparrow, \downarrow$ and $\epsilon_{\mathbf{k}} = -2t(\cos k_x + \cos k_y + \cos k_z)$ is the free electron dispersion relation. The Hamiltonian is block diagonal in $\mathbf{k}$. We recast the Hamiltonian into

the following form,

$$\mathcal{H}_{MF} = \sum_{\mathbf{k}\sigma} \left(\epsilon_{\mathbf{k}} c^{\dagger}_{\mathbf{k}\sigma} c_{\mathbf{k}\sigma} + \epsilon_{\mathbf{k+Q}} c^{\dagger}_{\mathbf{k+Q}\sigma} c_{\mathbf{k+Q}\sigma} \right) - \Delta_{AF} \sum_{\mathbf{k}\sigma} \eta(\sigma) \left(c^{\dagger}_{\mathbf{k+Q}\sigma} c_{\mathbf{k}\sigma} + c^{\dagger}_{\mathbf{k+2Q}\sigma} c_{\mathbf{k+Q}\sigma} \right) \quad \text{(B.9)}$$

where in the summations, $\mathbf{k}$ is now limited to that part of the Brillouin zone, for which $\epsilon_{\mathbf{k}} < 0$. Since $\epsilon_{\mathbf{k+Q}} = -\epsilon_{\mathbf{k}}$ and $\mathbf{k} + 2\mathbf{Q} = \mathbf{k}$, we get

$$\mathcal{H}_{MF} = \sum_{\mathbf{k}\sigma} \left\{ \epsilon_{\mathbf{k}} \left(c^{\dagger}_{\mathbf{k}\sigma} c_{\mathbf{k}\sigma} - c^{\dagger}_{\mathbf{k+Q}\sigma} c_{\mathbf{k+Q}\sigma} \right) - \Delta_{AF} \eta(\sigma) \left(c^{\dagger}_{\mathbf{k+Q}\sigma} c_{\mathbf{k}\sigma} + c^{\dagger}_{\mathbf{k}\sigma} c_{\mathbf{k+Q}\sigma} \right) \right\} \quad \text{(B.10)}$$

B.2 Diagonalization of the Hamiltonian

The Hamiltonian can be written in matrix form as follows.

$$\mathcal{H}_{MF} = \sum_{\mathbf{k}\sigma} \begin{bmatrix} c_{\mathbf{k}\sigma} \\ c_{\mathbf{k+Q}\sigma} \end{bmatrix}^{\dagger} \begin{bmatrix} \epsilon_{\mathbf{k}} & -\eta(\sigma)\Delta_{AF} \\ -\eta(\sigma)\Delta_{AF} & -\epsilon_{\mathbf{k}} \end{bmatrix} \begin{bmatrix} c_{\mathbf{k}\sigma} \\ c_{\mathbf{k+Q}\sigma} \end{bmatrix} \quad \text{(B.11)}$$

The matrix

$$M = \begin{bmatrix} \epsilon_{\mathbf{k}} & -\eta(\sigma)\Delta_{AF} \\ -\eta(\sigma)\Delta_{AF} & -\epsilon_{\mathbf{k}} \end{bmatrix} \quad \text{(B.12)}$$

can be diagonalized easily to get the eigenvalues as $E^{\mp}_{\mathbf{k}} = \mp\sqrt{{\epsilon_{\mathbf{k}}}^2 + \Delta^2_{AF}}$. The eigen vectors corresponding eigenvalues $E^{\mp}_{\mathbf{k}}$ are found to be respectively,

$$v^{-} = \begin{bmatrix} \alpha_{\mathbf{k}} \\ \eta(\sigma)\beta_{\mathbf{k}} \end{bmatrix} \quad v^{+} = \begin{bmatrix} -\eta(\sigma)\beta_{\mathbf{k}} \\ \alpha_{\mathbf{k}} \end{bmatrix} \quad \text{(B.13)}$$

Here $\alpha_{\mathbf{k}}$ and $\beta_{\mathbf{k}}$ are given by

$$\alpha_{\mathbf{k}} = \frac{1}{\sqrt{2}} \left(1 - \frac{\epsilon_{\mathbf{k}}}{\sqrt{\epsilon^2_{\mathbf{k}} + \Delta^2_{AF}}} \right)^{1/2} \quad \text{(B.14)}$$

$$\beta_{\mathbf{k}} = \frac{1}{\sqrt{2}} \left(1 + \frac{\epsilon_{\mathbf{k}}}{\sqrt{\epsilon^2_{\mathbf{k}} + \Delta^2_{AF}}} \right)^{1/2} \quad \text{(B.15)}$$

It is easy to see that the transformation

$$U = \begin{bmatrix} v^- & v^+ \end{bmatrix} = \begin{bmatrix} \alpha_{\mathbf{k}} & -\eta(\sigma)\beta_{\mathbf{k}} \\ \eta(\sigma)\beta_{\mathbf{k}} & \alpha_{\mathbf{k}} \end{bmatrix} \tag{B.16}$$

diagonalizes the matrix M in the following way

$$U^{-1}MU = \begin{bmatrix} E^-_{\mathbf{k}} & 0 \\ 0 & E^+_{\mathbf{k}} \end{bmatrix}$$

Thus the diagonalized Hamiltonian becomes

$$\mathcal{H}_{MF} = \sum_{\mathbf{k}\sigma} \begin{bmatrix} d_{\mathbf{k}\sigma} \\ d_{\mathbf{k}+\mathbf{Q}\sigma} \end{bmatrix}^\dagger \begin{bmatrix} E^-_{\mathbf{k}} & 0 \\ 0 & E^+_{\mathbf{k}} \end{bmatrix} \begin{bmatrix} d_{\mathbf{k}\sigma} \\ d_{\mathbf{k}+\mathbf{Q}\sigma} \end{bmatrix} \tag{B.17}$$

The antiferromagnetic quasiparticle operators $d_{\mathbf{k}\sigma}$, are related to the electron operators $c_{k\sigma}$, by the following transformation

$$\begin{bmatrix} d_{\mathbf{k}\sigma} \\ d_{\mathbf{k}+\mathbf{Q}\sigma} \end{bmatrix} = \begin{bmatrix} \alpha_{\mathbf{k}} & \eta(\sigma)\beta_{\mathbf{k}} \\ -\eta(\sigma)\beta_{\mathbf{k}} & \alpha_{\mathbf{k}} \end{bmatrix} \begin{bmatrix} c_{k\sigma} \\ c_{k+Q\sigma} \end{bmatrix} \tag{B.18}$$

The ground state of the Hamiltonian is the fully projected sea of the quasiparticles filled up to the Fermi level,

$$|\Psi_0(\Delta_{AF})\rangle = \mathcal{P}_G \prod_{k\leq k_F} d^\dagger_{\mathbf{k}\uparrow} d^\dagger_{\mathbf{k}\downarrow} |0\rangle \tag{B.19}$$

where $\mathcal{P}_G = \prod_i (1 - n_{i\uparrow} n_{i\downarrow})$ is Gutzwiller projector. It is worth mentioning here that, since $\epsilon_{\mathbf{k}} < 0$, therefore for $\Delta_{AF} = 0$ we get $\alpha_{\mathbf{k}} = 1$ and $\beta_{\mathbf{k}} = 0$, which reduces Eq. (B.18) to the identity transformation as it should.

B.3 Wavefunction with coexisting AF and SC order

If we assume that the ground state of the Hamiltonian consists of coexisting antiferromagnetic (AF) and superconducting (SC) phases, then a reasonable variational wavefunction would be a BCS wavefunction with built in pairs of AF quasiparticles (instead of bare electrons). Such

a wavefunction in fixed N (particle number) formulation can be written as,

$$|\Psi_0(\Delta_{AF}, \Delta_{SC})\rangle = \mathcal{P}_G \mathcal{P}_N \prod_{\mathbf{k}} \left(u_{\mathbf{k}} + v_{\mathbf{k}} d^{\dagger}_{\mathbf{k}\uparrow} d^{\dagger}_{-\mathbf{k}\downarrow}\right)|0\rangle \tag{B.20}$$

where the product index '**k**' runs over the first Brillouin zone (FBZ) and

$$\frac{v_{\mathbf{k}}}{u_{\mathbf{k}}} = \begin{cases} \phi^{-}(\mathbf{k}) & \text{for } \mathbf{k}, \text{ such that } \epsilon_{\mathbf{k}} < 0 \\ \phi^{+}(\mathbf{k}) & \text{for } \mathbf{k}, \text{ such that } \epsilon_{\mathbf{k}} > 0 \end{cases}$$

with

$$\phi^{\mp}(\mathbf{k}) = \frac{\Delta_{\mathbf{k}}}{\left(E^{\mp}_{\mathbf{k}} - \mu\right) + \sqrt{\left(E^{\mp}_{\mathbf{k}} - \mu\right)^2 + \Delta^2_{\mathbf{k}}}} \tag{B.21}$$

The quantity $\Delta_{\mathbf{k}} = \Delta_{SC} f(\mathbf{k})$ is the SC gap function and μ is the chemical potential.

B.4 Various phases in the wavefunction

The wavefunction given by Eq. (B.20) describes various phases depending upon the values of Δ_{AF} and Δ_{SC} as follows.

B.4.1 Pure superconducting ($\Delta_{AF} = 0$, $\Delta_{SC} \neq 0$)

For $\Delta_{AF} = 0$, $\alpha_{\mathbf{k}} = 1$ and $\beta_{\mathbf{k}} = 0$. Therefore

$$d^{\dagger}_{\mathbf{k}\uparrow} d^{\dagger}_{-\mathbf{k}\downarrow} = c^{\dagger}_{k\uparrow} c^{\dagger}_{k\downarrow} \qquad d^{\dagger}_{\mathbf{k}+\mathbf{Q}\uparrow} d^{\dagger}_{-(\mathbf{k}+\mathbf{Q})\downarrow} = c^{\dagger}_{k+Q\uparrow} c^{\dagger}_{-(k+Q)\downarrow}$$

With this, from Eq. (B.27) we get,

$$
\begin{aligned}
|\Psi_0(0,\Delta_{SC})\rangle &= \mathcal{P}_G\Bigg(\sum_{\mathbf{k}\,(\epsilon_\mathbf{k}<0)} \frac{\Delta_\mathbf{k}}{(-|\epsilon_\mathbf{k}|-\mu)+\sqrt{(-|\epsilon_\mathbf{k}|-\mu)^2+\Delta_\mathbf{k}^2}} c^\dagger_{k\uparrow}c^\dagger_{-k\downarrow} \\
&\quad + \sum_{\mathbf{k}\,(\epsilon_\mathbf{k}<0)} \frac{\Delta_{\mathbf{k}+\mathbf{Q}}}{(|\epsilon_{\mathbf{k}+\mathbf{Q}}|-\mu)+\sqrt{(|\epsilon_{\mathbf{k}+\mathbf{Q}}|-\mu)^2+\Delta_{\mathbf{k}+\mathbf{Q}}^2}} c^\dagger_{k+Q\uparrow}c^\dagger_{-(k+Q)\downarrow}\Bigg)^{N/2}|0\rangle \\
&= \mathcal{P}_G\Bigg(\sum_{\mathbf{k}\,(\epsilon_\mathbf{k}<0)} \frac{\Delta_\mathbf{k}}{(\epsilon_\mathbf{k}-\mu)+\sqrt{(\epsilon_\mathbf{k}-\mu)^2+\Delta_\mathbf{k}^2}} c^\dagger_{k\uparrow}c^\dagger_{-k\downarrow} \\
&\quad + \sum_{\mathbf{k}\,(\epsilon_\mathbf{k}>0)} \frac{\Delta_\mathbf{k}}{(\epsilon_\mathbf{k}-\mu)+\sqrt{(\epsilon_\mathbf{k}-\mu)^2+\Delta_\mathbf{k}}} c^\dagger_{k\uparrow}c^\dagger_{-k\downarrow}\Bigg)^{N/2}|0\rangle \\
&= \mathcal{P}_G\left(\sum_{\mathbf{k}\,(\mathbf{k}\in \mathrm{FBZ})} \frac{\Delta_\mathbf{k}}{(\epsilon_\mathbf{k}-\mu)+\sqrt{(\epsilon_\mathbf{k}-\mu)^2+\Delta_\mathbf{k}}} c^\dagger_{k\uparrow}c^\dagger_{-k\downarrow}\right)^{N/2}|0\rangle \\
&= \mathcal{P}_G\left(\sum_{\mathbf{k}} \varphi(\mathbf{k}) c^\dagger_{k\uparrow}c^\dagger_{-k\downarrow}\right)^{N/2}|0\rangle
\end{aligned}
\tag{B.22}
$$

which is the usual projected BCS wavefunction.

B.4.2 Pure antiferromagnetic ($\Delta_{AF}\neq 0, \Delta_{SC}\to 0$)

Because there is no double occupancy, $\mu \leq 0$ and hence $(E^+_\mathbf{k}-\mu)>0$. Therefore for $\epsilon_\mathbf{k}>0$, we get

$$
\phi^+(\mathbf{k})\Big|_{\Delta_{SC}=0} = \left.\frac{\Delta_{SC} f(\mathbf{k})}{\left(E^+_\mathbf{k}-\mu\right)+\sqrt{\left(E^+_\mathbf{k}-\mu\right)^2+\{\Delta_{SC} f(\mathbf{k})\}^2}}\right|_{\Delta_{SC}=0} = 0 \tag{B.23}
$$

Again since $(E^-_\mathbf{k}-\mu)\leq 0$ for $k\leq k_F$ and $(E^-_\mathbf{k}-\mu)>0$ for $\mathbf{k}>\mathbf{k}_F$, therefore for $\epsilon_\mathbf{k}\leq 0$ we get,

$$
\begin{aligned}
\lim_{\Delta_{SC}\to 0}\phi^-(\mathbf{k}) &= \lim_{\Delta_{SC}\to 0}\frac{\Delta_{SC} f(\mathbf{k})}{\left(E^-_\mathbf{k}-\mu\right)+\sqrt{\left(E^-_\mathbf{k}-\mu\right)^2+\{\Delta_{SC} f(\mathbf{k})\}^2}} \\
&= 0 \quad \text{for } \mathbf{k}>\mathbf{k}_F
\end{aligned}
\tag{B.24}
$$

Therefore Eq. (B.27) becomes

$$|\Psi_0(\Delta_{AF}, \Delta_{SC} \to 0)\rangle = \mathcal{P}_G \prod_{\mathbf{k}\leq\mathbf{k}_F} d^\dagger_{\mathbf{k}\uparrow} d^\dagger_{-\mathbf{k}\downarrow}|0\rangle \equiv \mathcal{P}_G \prod_{\mathbf{k}\leq\mathbf{k}_F} d^\dagger_{\mathbf{k}\uparrow} d^\dagger_{\mathbf{k}\downarrow}|0\rangle \tag{B.25}$$

which is same as Eq. (B.19).

B.4.3 Paramagnetic ($\Delta_{AF} = 0, \Delta_{SC} \to 0$)

For this case we have in addition, $d^\dagger_{\mathbf{k}\uparrow} d^\dagger_{\mathbf{k}\downarrow} = c^\dagger_{k\uparrow} c^\dagger_{k\downarrow}$ in Eq. (B.25). Therefore the wavefunction reduces to the paramagnetic Fermi sea of electrons.

$$|\Psi_0(0, \Delta_{SC} \to 0)\rangle = \mathcal{P}_G \prod_{\mathbf{k}\leq\mathbf{k}_F} c^\dagger_{k\uparrow} c^\dagger_{k\downarrow}|0\rangle \tag{B.26}$$

B.5 Transformation of the wavefunction into real space

The wavefunction with coexisting AF and SC order given in Eq. (B.20) can be written as

$$\begin{aligned} |\Psi_0\rangle &= \mathcal{P}_G \left(\sum_{\mathbf{k}} \frac{v_{\mathbf{k}}}{u_{\mathbf{k}}} d^\dagger_{\mathbf{k}\uparrow} d^\dagger_{-\mathbf{k}\downarrow} \right)^{N/2} |0\rangle \\ &= \mathcal{P}_G \left(\sum_{\mathbf{k}\ (\epsilon_{\mathbf{k}}<0)} \left\{ \phi^-(\mathbf{k}) d^\dagger_{\mathbf{k}\uparrow} d^\dagger_{-\mathbf{k}\downarrow} + \phi^+(\mathbf{k}+\mathbf{Q}) d^\dagger_{\mathbf{k}+\mathbf{Q}\sigma} d^\dagger_{-(\mathbf{k}+\mathbf{Q})\downarrow} \right\} \right)^{N/2} |0\rangle \end{aligned} \tag{B.27}$$

Using the transformations given by Eq. (B.18), we get

$$\begin{aligned} d^\dagger_{\mathbf{k}\uparrow} d^\dagger_{-\mathbf{k}\downarrow} &= \alpha^2_{\mathbf{k}} c^\dagger_{k\uparrow} c^\dagger_{-k\downarrow} - \alpha_{\mathbf{k}}\beta_{\mathbf{k}} c^\dagger_{k\uparrow} c^\dagger_{-(k+Q)\downarrow} + \alpha_{\mathbf{k}}\beta_{\mathbf{k}} c^\dagger_{k+Q\uparrow} c^\dagger_{-k\downarrow} \\ &\quad -\beta^2_{\mathbf{k}} c^\dagger_{k+Q\uparrow} c^\dagger_{-(k+Q)\downarrow} \\ d^\dagger_{\mathbf{k}+\mathbf{Q}\uparrow} d^\dagger_{-(\mathbf{k}+\mathbf{Q})\downarrow} &= -\beta^2_{\mathbf{k}} c^\dagger_{k\uparrow} c^\dagger_{-k\downarrow} - \alpha_{\mathbf{k}}\beta_{\mathbf{k}} c^\dagger_{k\uparrow} c^\dagger_{-(k+Q)\downarrow} + \alpha_{\mathbf{k}}\beta_{\mathbf{k}} c^\dagger_{k+Q\uparrow} c^\dagger_{-k\downarrow} \\ &\quad +\alpha^2_{\mathbf{k}} c^\dagger_{k+Q\uparrow} c^\dagger_{-(k+Q)\downarrow} \end{aligned}$$

Here we have used, $-\mathbf{k}+\mathbf{Q} = -\mathbf{k}+\mathbf{Q}-2\mathbf{Q} = -(\mathbf{k}+\mathbf{Q})$. Performing reverse Fourier transform of the $c_{k\sigma}$ operators, we get

$$\sum_{\mathbf{k}\,(\epsilon_{\mathbf{k}}<0)} \phi^{-}(\mathbf{k}) d^{\dagger}_{\mathbf{k}\uparrow} d^{\dagger}_{-\mathbf{k}\downarrow} = \sum_{\mathbf{k}\,(\epsilon_{\mathbf{k}}<0)} \phi^{-}(\mathbf{k}) \Bigg\{ \frac{1}{N} \sum_{ij} \Big(\alpha^2_{\mathbf{k}} - \alpha_{\mathbf{k}}\beta_{\mathbf{k}} e^{-i\mathbf{Q}.\mathbf{r}_j} + \alpha_{\mathbf{k}}\beta_{\mathbf{k}} e^{i\mathbf{Q}.\mathbf{r}_i} - \beta^2_{\mathbf{k}} e^{i\mathbf{Q}.(\mathbf{r}_i-\mathbf{r}_j)} \Big) e^{i\mathbf{k}.(\mathbf{r}_i-\mathbf{r}_j)} c^{\dagger}_{i\uparrow} c^{\dagger}_{i\downarrow} \Bigg\} \tag{B.28}$$

and

$$\sum_{\mathbf{k}\,(\epsilon_{\mathbf{k}}<0)} \phi^{+}(\mathbf{k}+\mathbf{Q}) d^{\dagger}_{\mathbf{k}+\mathbf{Q}\uparrow} d^{\dagger}_{-(\mathbf{k}+\mathbf{Q})\downarrow} = \sum_{\mathbf{k}\,(\epsilon_{\mathbf{k}}<0)} \phi^{+}(\mathbf{k}+\mathbf{Q}) \Bigg\{ \frac{1}{N} \sum_{ij} \Big(\alpha^2_{\mathbf{k}} e^{i\mathbf{Q}.(\mathbf{r}_i-\mathbf{r}_j)} - \alpha_{\mathbf{k}}\beta_{\mathbf{k}} e^{-i\mathbf{Q}.\mathbf{r}_j} + \alpha_{\mathbf{k}}\beta_{\mathbf{k}} e^{i\mathbf{Q}.\mathbf{r}_i} - \beta^2_{\mathbf{k}} \Big) e^{i\mathbf{k}.(\mathbf{r}_i-\mathbf{r}_j)} c^{\dagger}_{i\uparrow} c^{\dagger}_{i\downarrow} \Bigg\} \tag{B.29}$$

The second equation can be recast into slightly different form by writing $\mathbf{k} = \mathbf{k}' - \mathbf{Q}$, where $\mathbf{k}'$ is such that $\epsilon_{\mathbf{k}'} > 0$. We get $\alpha_{\mathbf{k}} = \alpha_{\mathbf{k}'-\mathbf{Q}} = \beta_{\mathbf{k}'}$ and $\beta_{\mathbf{k}} = \alpha_{\mathbf{k}'}$. Thus

$$\sum_{\mathbf{k}\,(\epsilon_{\mathbf{k}}<0)} \phi^{+}(\mathbf{k}+\mathbf{Q}) d^{\dagger}_{\mathbf{k}+\mathbf{Q}\uparrow} d^{\dagger}_{-(\mathbf{k}+\mathbf{Q})\downarrow} = \sum_{ij} \Bigg\{ \frac{1}{N} \sum_{\mathbf{k}\,(\epsilon_{\mathbf{k}}>0)} \phi^{+}(\mathbf{k}) \Big(\beta^2_{\mathbf{k}} - \alpha_{\mathbf{k}}\beta_{\mathbf{k}} e^{-i\mathbf{Q}.\mathbf{r}_i} + \alpha_{\mathbf{k}}\beta_{\mathbf{k}} e^{i\mathbf{Q}.\mathbf{r}_j} - \alpha^2_{\mathbf{k}} e^{-i\mathbf{Q}.(\mathbf{r}_i-\mathbf{r}_j)} \Big) e^{i\mathbf{k}.(\mathbf{r}_i-\mathbf{r}_j)} \Bigg\} c^{\dagger}_{i\uparrow} c^{\dagger}_{i\downarrow} \tag{B.30}$$

Therefore we can write the wavefunction as,

$$|\Psi_0(\Delta_{AF}, \Delta_{SC})\rangle = \mathcal{P}_G \left(\sum_{ij} \phi(\mathbf{r}_{i\uparrow}, \mathbf{r}_{j\downarrow}) c^{\dagger}_{i\uparrow} c^{\dagger}_{j\downarrow} \right)^{N/2} |0\rangle \tag{B.31}$$

where $\phi(\mathbf{r}_{i\uparrow}, \mathbf{r}_{j\downarrow}) = \phi_1(\mathbf{r}_{i\uparrow}, \mathbf{r}_{j\downarrow}) + \phi_2(\mathbf{r}_{i\uparrow}, \mathbf{r}_{j\uparrow})$, and ϕ_1, ϕ_2 are given by

$$\phi_1(\mathbf{r}_{i\uparrow}, \mathbf{r}_{j\downarrow}) = \frac{1}{N} \sum_{\mathbf{k}\,(\epsilon_{\mathbf{k}}<0)} \phi^{-}(\mathbf{k}) \Big(\alpha^2_{\mathbf{k}} - \alpha_{\mathbf{k}}\beta_{\mathbf{k}} e^{-i\mathbf{Q}.\mathbf{r}_j} + \alpha_{\mathbf{k}}\beta_{\mathbf{k}} e^{i\mathbf{Q}.\mathbf{r}_i} - \beta^2_{\mathbf{k}} e^{i\mathbf{Q}.(\mathbf{r}_i-\mathbf{r}_j)} \Big) e^{i\mathbf{k}.(\mathbf{r}_i-\mathbf{r}_j)} \tag{B.32}$$

$$\phi_2(\mathbf{r}_{i\uparrow}, \mathbf{r}_{j\downarrow}) = \frac{1}{N} \sum_{\mathbf{k}\,(\epsilon_{\mathbf{k}}>0)} \phi^{+}(\mathbf{k}) \Big(\beta^2_{\mathbf{k}} - \alpha_{\mathbf{k}}\beta_{\mathbf{k}} e^{-i\mathbf{Q}.\mathbf{r}_i} + \alpha_{\mathbf{k}}\beta_{\mathbf{k}} e^{i\mathbf{Q}.\mathbf{r}_j} - \alpha^2_{\mathbf{k}} e^{-i\mathbf{Q}.(\mathbf{r}_i-\mathbf{r}_j)} \Big) e^{i\mathbf{k}.(\mathbf{r}_i-\mathbf{r}_j)} \tag{B.33}$$

Expanding the right hand side of Eq. (B.31), and then applying the projection operator, we can write it as

$$|\Psi_0\rangle = \sum_{\substack{\{i_1,\ldots,i_M\}\{j_1,\ldots,j_M\} \\ i_m \neq j_n}} \left\{\det\left|\phi(\mathbf{r}_{i\uparrow}, \mathbf{r}_{j\downarrow})\right|\right\} c_{i_1\uparrow} c_{i_2\uparrow} \ldots c_{i_M\uparrow} c_{j_1\downarrow} c_{j_2\downarrow} \ldots c_{j_M\downarrow}|0\rangle \tag{B.34}$$

where the sum is over the set of occupancies $\{i_1, \ldots, i_M\}$ and $\{j_1, \ldots, j_M\}$ of $\uparrow$ and $\downarrow$ spins respectively, with the restriction that in any term $i_m \neq j_n$ for $m, n \leq M$. M is the number of $\uparrow$ or $\downarrow$ spins, $2M \leq N$. The determinant is given by,

$$\det\left|\phi(\mathbf{r}_{i\uparrow}, \mathbf{r}_{j\downarrow})\right| = \begin{vmatrix} \phi(\mathbf{r}_{i_1\uparrow}, \mathbf{r}_{j_1\downarrow}) & \cdots & \phi(\mathbf{r}_{i_1\uparrow}, \mathbf{r}_{j_M\downarrow}) \\ \vdots & & \vdots \\ \phi(\mathbf{r}_{i_M\uparrow}, \mathbf{r}_{j_1\downarrow}) & \cdots & \phi(\mathbf{r}_{i_M\uparrow}, \mathbf{r}_{j_M\downarrow}) \end{vmatrix} \tag{B.35}$$

Bibliography

[1] J. G. Bednorz and K. A. Müller, Z. Phys. B **64**, 189 (1986).

[2] J. G. Bednorz and K. A. Müller, Rev. Mod. Phys. **60**, 585 (1988).

[3] J. G. Bednorz, M. Takashige, and K. A. Müller, Europhys. Lett. **3**, 379 (1987).

[4] S. Uchida, H. Takagi, K. Kitazawa, and S. Tanaka, Jpn. J. Appl. Phys. **26**, L1 (1987).

[5] H. Takagi, S. Uchida, K. Kitazawa, and S. Tanaka, Jpn. J. Appl. Phys. **26**, L123 (1987).

[6] C. W. Chu et al., Phys. Rev. Lett. **58**, 405 (1987).

[7] C. W. Chu, P. H. Hor, R. L. Meng, L. Gao, and Z. J. Huang, Science **235**, 567 (1987).

[8] J. G. Bednorz, K. A. Müller, and M. Takashige, Science **236**, 73 (1987).

[9] R. J. Cava, R. B. van Dover, B. Batlogg, and E. A. Rietman, Phys. Rev. Lett. **58**, 408 (1987).

[10] M. K. Wu et al., Phys. Rev. Lett. **58**, 908 (1987).

[11] H. Maeda, Y. Tanaka, M. Fukutomi, and T. Asano, Jpn. J. Appl. Phys. **27**, L209 (1988).

[12] R. M. Hazen et al., Phys. Rev. Lett. **60**, 1174 (1988).

[13] Z. Z. Sheng and A. M. Hermann, Nature **332**, 138 (1988).

[14] R. M. Hazen et al., Phys. Rev. Lett. **60**, 1657 (1988).

[15] A. Schilling, M. Cantoni, J. D. Guo, and H. R. Ott, Nature **363**, 56 (1993).

[16] C. W. Chu et al., Nature **365**, 323 (1993).

[17] R. M. Hazen, Crystal structures of high temperature superconductors, in *Physical Properties of High Temperature Superconductors II*, edited by D. M. Ginsberg, page 121, World Scientific, 1990.

[18] B. Raveau, C. Michel, and M. Hervieu, Structual chemistry of high T_c superconductors, in *Studies of High Temperature Superconductors 2*, edited by A. V. Narlikar, page 1, Nova Science Publishers, 1989.

[19] M. A. G. Aranda, Adv. Mater. **6**, 905 (1994).

[20] P. J. Ford and G. A. Saunders, *The Rise of the Superconductors*, CRC Press, 2004.

[21] A. Damascelli, Z. Hussain, and Z.-X. Shen, Rev. Mod. Phys. **75**, 475 (2003).

[22] J. D. Jorgensen, Phys. Today **44**, 34 (1991).

[23] C. C. Torardi et al., Science **240**, 631 (1988).

[24] E. Dagotto, Rev. Mod. Phys. **66**, 763 (1994).

[25] M. A. Kastner, R. J. Birgeneau, G. Shirane, and Y. Endoh, Rev. Mod. Phys. **70**, 897 (1998).

[26] P. W. Anderson, *The Theory of Superconductivity in the High-T_c Cuprates*, Princeton Series in Physics, Princeton University Press, 1997.

[27] P. A. Lee, N. Nagaosa, and X.-G. Wen, Rev. Mod. Phys. **78**, 17 (2006).

[28] B. Keimer et al., Phys. Rev. B **46**, 14034 (1992).

[29] G. Burns, *High-Temperature Superconductivity*, Academic Press, 1992.

[30] P. Fazekas, *Lecture Notes on Electron Correlation and Magnetism*, volume 5 of *Series in Modern Condensed Matter Physics*, World Scientific, 1999.

[31] M. Imada, A. Fujimori, and Y. Tokura, Rev. Mod. Phys. **70**, 1039 (1998).

[32] S. Uchida et al., Phys. Rev. B **43**, 7942 (1991).

[33] J. P. Falck, A. Levy, M. A. Kastner, and R. J. Birgeneau, Phys. Rev. Lett. **69**, 1109 (1992).

[34] T. Thio, R. J. Birgeneau, A. Cassanho, and M. A. Kastner, Phys. Rev. B **42**, 10800 (1990).

[35] J. M. Tranquada, Neutron Scattering Studies of Antiferromagnetic Correlations in Cuprates, in *Handbook of High-Temperature Superconductivity*, edited by J. R. Schrieffer and J. S. Brooks, Springer, 2007.

[36] D. Vaknin et al., Phys. Rev. Lett. **58**, 2802 (1987).

[37] B. Keimer et al., Phys. Rev. B **45**, 7430 (1992).

[38] K. B. Lyons, P. A. Fleury, J. P. Remeika, A. S. Cooper, and T. J. Negran, Phys. Rev. B **37**, 2353 (1988).

[39] P. E. Sulewski, P. A. Fleury, K. B. Lyons, S.-W. Cheong, and Z. Fisk, Phys. Rev. B **41**, 225 (1990).

[40] R. J. Birgeneau et al., Phys. Rev. Lett. **59**, 1329 (1987).

[41] P. Böni et al., Phys. Rev. B **38**, 185 (1988).

[42] J. M. Tranquada et al., Phys. Rev. Lett. **60**, 156 (1988).

[43] H. Casalta et al., Phys. Rev. B **50**, 9688 (1994).

[44] B. Batlogg, Physics Today **44**, 44 (1991).

[45] D. M. Ginsberg, editor, *Physical Properties of High Temperature Superconductors*, volume I-V, World Scientific, 1989-96.

[46] C. C. Tsuei and J. R. Kirtley, Rev. Mod. Phys. **72**, 969 (2000).

[47] D. N. Basov and T. Timusk, Rev. Mod. Phys. **77**, 721 (2005).

[48] J. R. Schrieffer and J. S. Brooks, editors, *Handbook of High-Temperature Superconductivity*, Springer, 2007.

[49] H. Takagi et al., Phys. Rev. Lett. **69**, 2975 (1992).

[50] A. P. Mackenzie, S. R. Julian, D. C. Sinclair, and C. T. Lin, Phys. Rev. B **53**, 5848 (1996).

[51] S. J. Hagen, T. W. Jing, Z. Z. Wang, J. Horvath, and N. P. Ong, Phys. Rev. B **37**, 7928 (1988).

[52] S. Martin, A. T. Fiory, R. M. Fleming, L. F. Schneemeyer, and J. V. Waszczak, Phys. Rev. B **41**, 846 (1990).

[53] T. A. Friedmann, M. W. Rabin, J. Giapintzakis, J. P. Rice, and D. M. Ginsberg, Phys. Rev. B **42**, 6217 (1990).

[54] N. E. Hussey, Normal State Transport Properties, in *Handbook of High-Temperature Superconductivity*, edited by J. R. Schrieffer and J. S. Brooks, Springer, 2007.

[55] S. L. Cooper and K. E. Gray, Anisotropy and Interlayer Coupling in the High T_c Cuprates, in *Physical Properties of High Temperature Superconductors IV*, edited by D. M. Ginsberg, volume 4, World Scientific, 1994.

[56] S. W. Tozer, A. W. Kleinsasser, T. Penney, D. Kaiser, and F. Holtzberg, Phys. Rev. Lett. **59**, 1768 (1987).

[57] N. E. Hussey, J. R. Cooper, Y. Kodama, and Y. Nishihara, Phys. Rev. B **58**, R611 (1998).

[58] J. M. Harris, Y. F. Yan, and N. P. Ong, Phys. Rev. B **46**, 14293 (1992).

[59] J. Orenstein, Optical Conductivity and Spatial Inhomogeneity in Cuprate Superconductors, in *Handbook of High-Temperature Superconductivity*, edited by J. R. Schrieffer and J. S. Brooks, Springer, 2007.

[60] T. Timusk and B. Statt, Rep. Prog. Phys. **62**, 61 (1999).

[61] M. Randeria, cond-mat/9710223 (1997).

[62] N. J. Curro, T. Imai, C. P. Slichter, and B. Dabrowski, Phys. Rev. B **56**, 877 (1997).

[63] T. Nakano et al., Phys. Rev. B **49**, 16000 (1994).

[64] J. W. Loram, K. A. Mirza, J. R. Cooper, and W. Y. Liang, Phys. Rev. Lett. **71**, 1740 (1993).

[65] H. Ding et al., Nature **382**, 51 (1996).

[66] H. Ding et al., Phys. Rev. Lett. **78**, 2628 (1997).

[67] D. S. Marshall et al., Phys. Rev. Lett. **76**, 4841 (1996).

[68] C. E. Gough et al., Nature **326**, 855 (1987).

[69] Z.-X. Shen and D. S. Dessau, Phys. Rep. **253**, 1 (1995).

[70] P. V. Bogdanov et al., Phys. Rev. Lett. **89**, 167002 (2002).

[71] X. J. Zhou, T. Cuk, T. Devereaux, N. Nagaosa, and Z.-X. Shen, Angle-resolved Photoemission Spectroscopy on Electronic Structure and Electron-Phonon Coupling in Cuprate Superconductors, in *Handbook of High-Temperature Superconductivity*, edited by J. R. Schrieffer and J. S. Brooks, Springer, 2007.

[72] H. Ding et al., Phys. Rev. B **54**, R9678 (1996).

[73] D. J. V. Harlingen, Rev. Mod. Phys. **67**, 515 (1995).

[74] C. C. Tsuei et al., Phys. Rev. Lett. **73**, 593 (1994).

[75] C. C. Tsuei et al., Science **271**, 329 (1996).

[76] A. V. Fedorov et al., Phys. Rev. Lett. **82**, 2179 (1999).

[77] D. S. Dessau et al., Phys. Rev. Lett. **66**, 2160 (1991).

[78] M. Randeria et al., Phys. Rev. Lett. **74**, 4951 (1995).

[79] J. M. Imer et al., Phys. Rev. Lett. **62**, 336 (1989).

[80] W. E. Pickett, Rev. Mod. Phys. **61**, 433 (1989).

[81] V. J. Emery, Phys. Rev. Lett. **58**, 2794 (1987).

[82] C. M. Varma, S. Schmitt-Rink, and E. Abrahams, Solid State Commun. **62**, 681 (1987).

[83] M. S. Hybertsen, M. Schlüter, and N. E. Christensen, Phys. Rev. B **39**, 9028 (1989).

[84] F. C. Zhang and T. M. Rice, Phys. Rev. B **37**, 3759 (1988).

[85] P. W. Anderson, Science **235**, 1196 (1987).

[86] M. S. Hybertsen, E. B. Stechel, M. Schlüter, and D. R. Jennison, Phys. Rev. B **41**, 11068 (1990).

[87] S. M. Hayden et al., Phys. Rev. Lett. **67**, 3622 (1991).

[88] J. Hubbard, Proc. R. Soc. London, Ser. A **276**, 238 (1963).

[89] J. Bardeen, L. N. Cooper, and J. R. Schrieffer, Phys. Rev. **108**, 1175 (1957).

[90] J. R. Schrieffer, X.-G. Wen, and S.-C. Zhang, Phys. Rev. Lett. **60**, 944 (1988).

[91] K. Miyake, S. Schmitt-Rink, and C. M. Varma, Phys. Rev. B **34**, 6554 (1986).

[92] P. Monthoux and D. Pines, Phys. Rev. B **47**, 6069 (1993).

[93] R. S. Markiewicz, Int. J. Mod. Phys. B **5**, 2037 (1993).

[94] E. Dagotto, A. Nazarenko, and A. Moreo, Phys. Rev. Lett. **74**, 310 (1995).

[95] E. Demler, W. Hanke, and S.-C. Zhang, Rev. Mod. Phys. **76**, 909 (2004).

[96] N. F. Mott, Contemp. Phys. **30**, 373 (1990).

[97] C. M. Varma, P. B. Littlewood, S. Schmitt-Rink, E. Abrahams, and A. E. Ruckenstein, Phys. Rev. Lett. **63**, 1996 (1989).

[98] K. A. Moler, J. R. Kirtley, D. G. Hinks, T. W. Li, and M. Xu, Science **279**, 1193 (1998).

[99] A. A. Tsvetkov et al., Nature **395**, 360 (1998).

[100] P. W. Anderson, Phys. Rev. **115**, 2 (1959).

[101] S. Chakravarty, B. I. Halperin, and D. R. Nelson, Phys. Rev. Lett. **60**, 1057 (1988).

[102] S. Chakravarty, B. I. Halperin, and D. R. Nelson, Phys. Rev. B **39**, 2344 (1989).

[103] H.-Q. Ding and M. S. Makivić, Phys. Rev. Lett. **64**, 1449 (1990).

[104] M. S. Makivić and H.-Q. Ding, Phys. Rev. B **43**, 3562 (1991).

[105] P. W. Anderson et al., J. Phys.: Condens. Matter **16**, R755 (2004).

[106] S. A. Kivelson, D. S. Rokhsar, and J. P. Sethna, Phys. Rev. B **35**, 8865 (1987).

[107] Z. Zou and P. W. Anderson, Phys. Rev. B **37**, 627 (1988).

[108] G. Baskaran, Z. Zou, and P. W. Anderson, Solid State Commun. **63**, 973 (1987).

[109] A. E. Ruckenstein, P. J. Hirschfeld, and J. Appel, Phys. Rev. B **36**, 857 (1987).

[110] G. Kotliar and J. Liu, Phys. Rev. B **38**, 5142 (1988).

[111] G. Baskaran and P. W. Anderson, Phys. Rev. B **37**, 580 (1988).

[112] L. B. Ioffe and A. I. Larkin, Phys. Rev. B **39**, 8988 (1989).

[113] N. Nagaosa and P. A. Lee, Phys. Rev. Lett. **64**, 2450 (1990).

[114] X.-G. Wen and P. A. Lee, Phys. Rev. Lett. **76**, 503 (1996).

[115] F. C. Zhang, C. Gros, T. M. Rice, and H. Shiba, Supercond. Sci. Tech. **1**, 36 (1988).

[116] B. Edegger, V. N. Muthukumar, and C. Gros, Adv. Phys. **56**, No. 6, 927 (2007).

[117] M. C. Gutzwiller, Phys. Rev. Lett. **10**, 159 (1963).

[118] J. C. Campuzano et al., Phys. Rev. Lett. **83**, 3709 (1999).

[119] N. Bulut, Adv. Phys. **51**, 1587 (2002).

[120] J. Jaklic and P. Prelovsek, Adv. Phys. **49**, 1 (1999).

[121] F. Becca, A. Parola, and S. Sorella, Phys. Rev. B **61**, R16287 (2000).

[122] E. Dagotto and T. M. Rice, Science **271**, 618 (1996).

[123] A. Georges, G. Kotliar, W. Krauth, and M. J. Rozenberg, Rev. Mod. Phys. **68**, 13 (1996).

[124] C. Gros, Phys. Rev. B **38**, 931 (1988).

[125] C. Gros, Ann. Phys. (N.Y.) **189**, 53 (1989).

[126] M. Calandra and S. Sorella, Phys. Rev. B **61**, R11894 (2000).

[127] S. Sorella, Phys. Rev. B **64**, 024512 (2001).

[128] S. Sorella et al., Phys. Rev. Lett. **88**, 117002 (2002).

[129] V. I. Anisimov, M. A. Korotin, I. A. Nekrasov, and Z. V. Pchelkina, Phys. Rev. B **66**, 100502 (2002).

[130] L. Spanu, M. Lugas, F. Becca, and S. Sorella, Phys. Rev. B **77**, 024510 (2008).

[131] W. L. McMillan, Phys. Rev. **138**, A 442 (1965).

[132] D. Ceperley, G. V. Chester, and M. H. Kalos, Phys. Rev. B **16**, 3081 (1977).

[133] D. Ceperley, Phys. Rev. B **18**, 3126 (1978).

[134] C. Gros, R. Joynt, and T. M. Rice, Phys. Rev. B **36**, 381 (1987).

[135] H. Yokoyama and H. Shiba, J. Phys. Soc. Jpn. **56**, 1490 (1987).

[136] H. Yokoyama and H. Shiba, J. Phys. Soc. Jpn. **56**, 3582 (1987).

[137] H. Yokoyama and H. Shiba, J. Phys. Soc. Jpn. **57**, 2482 (1988).

[138] H. Yokoyama and M. Ogata, J. Phys. Soc. Jpn. **65**, 3615 (1996).

[139] T. Giamarchi and C. Lhuillier, Phys. Rev. B **43**, 12943 (1991).

[140] A. Himeda and M. Ogata, Phys. Rev. B **60**, R9935 (1999).

[141] A. Paramekanti, M. Randeria, and N. Trivedi, Phys. Rev. Lett. **87**, 217002 (2001).

[142] A. Paramekanti, M. Randeria, and N. Trivedi, Phys. Rev. B **70**, 054504 (2004).

[143] S. Yunoki, E. Dagotto, and S. Sorella, Phys. Rev. Lett. **94**, 037001 (2005).

[144] C. P. Nave, D. A. Ivanov, and P. A. Lee, Phys. Rev. B **73**, 104502 (2006).

[145] F. Tan and Q.-H. Wang, Phys. Rev. Lett. **100**, 117004 (2008).

[146] P. W. Anderson and Z. Zou, Phys. Rev. Lett. **60**, 132 (1988).

[147] P. W. Anderson, Science **256**, 1526 (1992).

[148] S. Chakravarty, A. Sudbø, P. W. Anderson, and S. Strong, Science **261**, 337 (1993).

[149] G. Kotliar et al., Europhys. Lett. **15**, 655 (1991).

[150] O. K. Andersen, A. I. Liechtenstein, O. Jepsen, and F. Paulsen, J. Phys. Chem. Solids **56**, 1573 (1995).

[151] H. Ding et al., Phys. Rev. Lett. **76**, 1533 (1996).

[152] D. L. Feng et al., Phys. Rev. Lett. **86**, 5550 (2001).

[153] Y.-D. Chuang et al., Phys. Rev. Lett. **87**, 117002 (2001).

[154] T. Valla et al., Phys. Rev. B **73**, 184518 (2006).

[155] S. V. Borisenko et al., Phys. Rev. Lett. **96**, 117004 (2006).

[156] T. Yamasaki et al., Phys. Rev. B **75**, 140513(R) (2007).

[157] D. H. Lu et al., Phys. Rev. Lett. **86**, 4370 (2001).

[158] Y. Lan, J. Qin, and S. Feng, Phys. Rev. B **76**, 014533 (2007).

[159] Rossat-Mignod et al., Physica C **185**, 86 (1991).

[160] H. F. Fong et al., Phys. Rev. Lett. **75**, 316 (1995).

[161] B. Keimer et al., J. Phys. Chem. Solids **60**, 1007 (1999).

[162] K. Yamada et al., Phys. Rev. B **57**, 6165 (1998).

[163] B. J. Sternlieb, G. Shirane, J. M. Tranquada, M. Sato, and S. Shamoto, Phys. Rev. B **47**, 5320 (1993).

[164] M. Biagini, Phys. Rev. B **51**, 6107 (1995).

[165] M. Biagini, Phys. Rev. B **52**, 7715 (1995).

[166] M. Biagini, Phys. Rev. B **53**, 9359 (1996).

[167] F. Yuan, J. Qin, S. Feng, and W. Y. Chen, Phys. Rev. B **67**, 134504 (2003).

[168] F. Krüger and S. Scheidl, Phys. Rev. B **70**, 064421 (2004).

[169] H. Zhao and J. R. Engelbrecht, Phys. Rev. B **71**, 054508 (2005).

[170] T. Zhou, Z. D. Wang, and J.-X. Li, Phys. Rev. B **75**, 024516 (2007).

[171] H. Yamase and W. Metzner, Phys. Rev. B **73**, 214517 (2006).

[172] K. Binder and D. W. Heermann, *Monte Carlo Simulation in Statistical Physics*, volume 80 of *Springer Series in Solid-State Sciences*, Springer Verlag, 4th edition, 2002.

[173] R. M. Neal, *Probabilistic Inference Using Markov Chain Monte Carlo Methods*, Technical report, Department of Computer Science, University of Toronto, 1993.

[174] S. Sorella, G. E. Santoro, and F. Becca, *SISSA Lecture notes on Numerical methods for strongly correlated electrons*, Lecture notes, SISSA-ISAS, Italy, 2008.

[175] B. Walsh, Markov Chain Monte Carlo and Gibbs Sampling, 2004 (unpublished).

[176] A. Chakraborty, A. J. Epstein, M. Jarrell, and E. M. McCarron, Phys. Rev. B **40**, 5296 (1989).

[177] S.-W. Cheong et al., Phys. Rev. B **44**, 9739 (1991).

[178] M. Hücker et al., Phys. Rev. B **59**, R725 (1999).

[179] J. L. Tallon, C. Bernhard, G. V. M. Williams, and J. W. Loram, Phys. Rev. Lett. **79**, 5294 (1997).

[180] K. Ishida et al., Phys. Rev. B **53**, 2827 (1996).

[181] M. Azuma, Y. Fujishiro, M. Takano, M. Nohara, and H. Takagi, Phys. Rev. B **55**, R8658 (1997).

[182] S. R. White et al., Phys. Rev. B **40**, 506 (1989).

[183] R. R. Santos, Braz. J. Phys. **33**, 36 (2003).

[184] N. Bulut, Phys. Rev. B **68**, 235103 (2003).

[185] G. B. Martins, M. Laukamp, J. Riera, and E. Dagotto, Phys. Rev. Lett. **78**, 3563 (1997).

[186] A. W. Sandvik, E. Dagotto, and D. J. Scalapino, Phys. Rev. B **56**, 11701 (1997).

[187] M. Laukamp et al., Phys. Rev. B **57**, 10755 (1998).

[188] P. Sengupta, R. T. Scaletter, and R. R. P. Singh, Phys. Rev. B **66**, 144420 (2002).

[189] P. Monthoux and D. Pines, Phys. Rev. B **49**, 4261 (1994).

[190] P. Monthoux and D. J. Scalapino, Phys. Rev. Lett. **72**, 1874 (1994).

[191] S. C. Zhang, Science **275**, 1089 (1997).

[192] Y. Sidis et al., Phys. Rev. Lett. **86**, 4100 (2001).

[193] J. A. Hodges et al., Phys. Rev. B **66**, 020501 (2002).

[194] H. A. Mook et al., Phys. Rev. B **66**, 144513 (2002).

[195] H. Kotegawa et al., Phys. Rev. B **69**, 014501 (2004).

[196] M. Inui, S. Doniach, P. J. Hirschfeld, and A. E. Ruckenstein, Phys. Rev. B **37**, 2320 (1988).

[197] S. Shamoto, M. Sato, J. M. Tranquada, B. J. Sternlieb, and G. Shirane, Phys. Rev. B **48**, 13817 (1993).

[198] D. Reznik et al., Phys. Rev. B **53**, R14741 (1996).

[199] S. M. Hayden, G. Aeppli, T. G. Perring, H. A. Mook, and F. Doğan, Phys. Rev. B **54**, R6905 (1996).

[200] A. J. Millis and H. Monien, Phys. Rev. B **54**, 16172 (1996).

[201] D. Muñoz, I. d. P. R. Moreira, and F. Illas, Phys. Rev. B **71**, 172505 (2005).

[202] H. Ding et al., Phys. Rev. Lett. **74**, 2784 (1995).

[203] I. Vobornik et al., Physica C **317**, 589 (1999).

[204] G. Zhao, Phys. Rev. B **75**, 140510(R) (2007).

[205] P. A. Lee and K. Kuboki, J. Phys. Chem. Solids **56**, 1633 (1995).

[206] C. J. Umrigar and C. Filippi, Phys. Rev. Lett. **94**, 150201 (2005).

[207] S. Sorella, Phys. Rev. B **71**, R241103 (2005).

[208] C. S. Hellberg and E. Manousakis, Phys. Rev. B **52**, 4639 (1995).

[209] M. Y. Kagan and T. M. Rice, J. Phys.: Condens. Matter **6**, 3771 (1994).

[210] D. Poilblanc, Phys. Rev. B **52**, 9201 (1995).

[211] J. M. Wheatley, T. C. Hsu, and P. W. Anderson, Phys. Rev. B **37**, 5897 (1988).

[212] J. M. Wheatley, T. C. Hsu, and P. W. Anderson, Nature **333**, 121 (1988).

[213] V. N. Muthukumar and G. Baskaran, arXiv:cond-mat/9403078v1 (1994).

[214] G. G. N. Angilella, *Interlayer Pair-Tunneling in Layered Cuprates*, PhD thesis, Università degli Studi di Catania, 1999 (unpublished).

[215] S. Chakravarty, H.-Y. Kee, and E. Abrahams, Phys. Rev. Lett. **82**, 2366 (1999).

[216] B. Edegger, N. Fukushima, C. Gros, and V. N. Muthukumar, Phys. Rev. B **72**, 134504 (2005).

[217] R. Blankenbecler, D. J. Scalapino, and R. L. Sugar, Phys. Rev. D **24**, 2278 (1981).

[218] M. Suzuki, editor, *Quantum Monte Carlo Methods*, volume 74 of *Springer series in Solid State Sciences*, Springer, New York, 1987.

[219] J. E. Hirsch, Phys. Rev. B **31**, 4403 (1985).

[220] E. Loh and J. Gubernatis, Stable numerical simulation of models of interacting electrons in condensed-matter physics, in *Electronic Phase Transitions*, edited by W. Hanke and Y. V. Kopaev, Modern Problems of Condensed Matter Physics, page 177, Elseiver Science Publisher, 1992.

Publications

Journal

1. Amal Medhi and Saurabh Basu, *Importance of interlayer pair tunneling: A variational perspective* (communicated)
2. Amal Medhi, Saurabh Basu, and Charudatt Kadolkar, *Phase diagram for a t-J bilayer: role of interlayer couplings* (accepted for publication in Eur. Phys. J. B)
3. Amal Medhi, Saurabh Basu, and Charudatt Kadolkar, *Coexistence of magnetism and superconductivity in a t-J bilayer*, Phys. Rev. B **76**, 235122 (2007)
4. Amal Medhi, Saurabh Basu, and Charudatt Kadolkar, *Stability of the Gutzwiller projected BCS wavefunction in t-J bilayers: A Variational Monte Carlo study*, Physica C **451**, 17 (2007)
5. Amal Medhi, Saurabh Basu, and Charudatt Kadolkar, *Nonmagnetic impurities in a two-leg Hubbard ladder*, J. Appl. Phys. **101**, 09D404 (2007)
6. Amal Medhi, Saurabh Basu, and Charudatt Kadolkar, *Quantum Monte Carlo study of the Hubbard model doped with nonmagnetic impurities*, Physica B **378-380**, 315 (2006)
7. Amal Medhi, Saurabh Basu, and Charudatt Kadolkar, *Variational Monte Carlo study of the antiferromagnetic state in t-J bilayers*, Indian J. Phys. **82** (3), 251 (2008)

Conference proceedings

1. Amal Medhi, Saurabh Basu, and Charudatt Kadolkar, *Phase diagram for a t-J bilayer: A variational Monte Carlo study*, Proceedings, DAE Solid State Physics Symposium (2008), (accepted)
2. Amal Medhi, Saurabh Basu, and Charudatt Kadolkar, *Effect of interplanar exchange coupling on the superconducting and magnetic properties of bilayer t-J model*, Proceedings, DAE Solid State Physics Symposium (2007), P-821
3. Amal Medhi, Saurabh Basu, and Charudatt Kadolkar, *Coexistence of superconductivity and antiferromagnetism in a bilayer t-J model*, Proceedings, DAE Solid State Physics Symposium (2006)
4. Amal Medhi, Saurabh Basu, and Charudatt Kadolkar, *Spin correlation studies in t-J bilayers*, Proceedings, DAE Solid State Physics Symposium (2005), P-593

Vita

Mr. Amal Medhi, born in Assam, India did his B.Sc. with Physics Honours in 1997 from Cotton College, Guwahati and M.Sc. in Physics in 2000 from Gauhati University, Guwahati. He joined IIT Guwahati for Ph.D. in 2002. He was awarded Junior Research Fellowship in 2002 and Senior Research Fellowship in 2004 by CSIR, India. Currently he is an Assistant Professor at the Department of Basic Sciences and Social Sciences, North-Eastern Hill University, Shillong, India.